Fall 1-31-2023

Waste-Derived Hybrid Nanocomposite For the Simultaneous Removal of Antibiotics and Dyes from Water Bodies

AbdelKader Ahmed
abdu192019@aucegypt.edu

The American University in Cairo
الجامعة الأمريكية بالقاهرة

The American University in Cairo CLIMATE CHANGE AUC@COP27

Graduate Studies

Waste-derived hybrid nanocomposite for the simultaneous removal of antibiotics and dyes from water bodies

A THESIS SUBMITTED BY

Abdelkadr Salih Ahmed

TO THE

Nanotechnology M.Sc. Program

Supervisor:
Dr. Mayyada El-Sayed
Associate Professor, Department of Chemistry

22/10/2022

in partial fulfillment of the requirements for the degree of
M.Sc. in Nanotechnology

`

Declaration of Authorship

I, Abdelkadr Salih Ahmed, declare that this thesis titled, "***Waste-derived hybrid nanocomposite for the simultaneous removal of antibiotics and dyes from water bodies***" and the work presented in it are my own. I confirm that:

- This work was done wholly or mainly while in candidature for a research degree at this University.
- Where any part of this thesis has previously been submitted for a degree or any other qualification at this University or any other institution, this has been clearly stated.
- Where I have consulted the published work of others, this is always clearly attributed.
- Where I have quoted from the work of others, the source is always given. With the exception of such quotations, this thesis is entirely my own work.
- I have acknowledged all main sources of help.
- Where the thesis is based on work done by myself jointly with others, I have made clear exactly what was done by others and what I have contributed myself.

Signed:

Date:

22/10/2022

`

Abstract

A novel eco-friendly approach was used to synthesize a hydroxyapatite-carbon nanocomposite (HAP-C) by utilizing the industrial waste of cement kiln dust (CKD) as a source of calcium for the synthesis. Citric acid was first used to chelate the calcium from CKD, then the chelate was converted into a mixture of calcium carbonate and carbon by calcination at 450°C for 1 h. The mixture was used as a precursor for the synthesis of HAP-C by reacting it with ortho-phosphoric acid via a precipitation method. HAP-C was then calcined at different temperatures of 400, 500, and 700°C under inert atmosphere, with a heating rate of 10°C/min for 2 h. The adsorption efficiency of the calcined composites towards rhodamine b (RB) dye and levofloxacin (LV) drug was compared to the uncalcined one, and the best performance was observed for the composite calcined at 700°C (HAP-C 700 A). BET, zeta potential, and TEM measurements indicated that this composite is mesoporous, with a negatively-charged surface at the working pH and an average particle size for the diameter and length are 10± 3.6 nm and 8± 2.9 nm for HAP-C 700A. Equilibrium studies revealed that the adsorption process is best described by Langmuir isotherm model with estimated maximum adsorption capacities of 9.65 and 14.84 mg/g for RB and LV, respectively. The maximum removal efficiency observed was 96 % for RB at 10, 15 and 25 ppm and 86 % for LV at 10 and 15 ppm. Kinetic studies revealed that adsorption of RB and LV followed the pseudo second order model. Thermodynamic analysis suggested exothermic and spontaneous physisorption possibly taking place through electrostatic attraction and hydrogen bonding. The approach proposed herein for the removal of emerging contaminants from water supports the concepts of zero waste management and circular economy.

`

Acknowledgements

I would like to express my utmost and sincere appreciation and gratitude to my supervisor **Dr. Mayyada El-Sayed** for the endless encouragement, patience, and guidance, which has fueled my drive to fulfil this project.

I would like also to express my appreciation to the American University in Cairo for the fellowship and research grant without which this project wouldn't have been possible.

Special thanks to my colleagues in STAR-SEP research group, Ms. Hebatullah Farghal, Ms. Dina Hassenein, Ms. Hanaa Essa, Ms. Hania Guirguis, and Mr. George Morocos.

My gratitude is also to Dr. Abdullah and Eng. Mohammad El-Sissi from the Process and Product Development Unit (PPDU) for their time and help.

I would like also to thank the Chemistry Department lab technicians, Mr. Emad Farag, Mr. Ali Reda, and Mr. Mohamed Nabeel.

`

Contents

`

`

`

List of Figures

`

`

`

List of Tables

`

List of Abbreviations

BET	Brunauer-Emmett-Teller
Ca/P	Calcium to Phosphorus ratio
CBZ	Carbamazepine
CECs	Contaminants of Emerging Concern
Ceph	Cephalexin
CIP	Ciprofloxacin
CKD	Cement Kiln Dust
CR	Congo red
D-R	Dubinin-Radushkevich
EDX	Energy Dispersive X-ray
FQ	Fluoroquinolone
FTIR	Fourier Transform Infrared
GAC	Granular Activated Carbon
HAP	Hydroxyapatite
HAP-C	Hydroxyapatite- Carbon composite
ICP	Inductively Coupled Plasma
ICP/OES	Inductively Coupled Plasma/ Optical Emission Spectroscopy
IUPAC	International Union of Pure and Applied Chemistry
LV	Levofloxacin
NOR	Norfloxacin
OFL	Ofloxacin
OTC	Oxytetracycline
RB	Rhodamine B
SEM	Scanning Electron Microscopy
SMX	Sulfamethoxazole
TC	Tetracycline
TCS	Triclosan
TEM	Transmission Electron Microscopy
TGA	Thermogravimetric Analysis

`

TY	Tylosin
UV-VIS	Ultraviolet-visible
XRD	X-ray Diffraction
XRF	X-ray Fluorescence
Y4D	Yellow 4 Dye

`

List of Symbols

A	Absorbance
l	Path length
ε	Molar absorptivity
C_o	Initial Concentration
C_e	Equilibrium Concentration
pK_a	Acid dissociation constant
K_L	Langmuir constant
K_f	Freundlich Constant
K_s	Sips constant
K_e	Equilibrium constant
k_1	Pseudo-first order rate constant
k_2	Pseudo-second order rate constant
R_L	Separation Factor
q_e	Equilibrium Adsorption Capacity
q_m	Maximum Adsorption Capacity
λ	Incident beam wavelength
θ	Bragg's Angle
d	Interplanar spacing
D	Size of the crystal
K	shape factor
β	Full width at half maximum peak (FWHM)
ΔH	Enthalpy
ΔG	Gibbs free energy
ΔS	Entropy

`

Chapter One

`

1.1 Introduction

One of the most essential needs of human beings is fresh water. The ever-increasing number of people in the world has created a significant stress on the sources of fresh water leading ultimately to scarcity of fresh water. The problem is not only limited to the increasing demand for fresh water due to the increase in population, but also due to the pollution of these limited sources of fresh water. The pollution can be attributed to the increasing activities of mankind, including the industrial and agricultural ones which are key players in the pollution of the sources of freshwater. Millions of tons of pollutants are discharged annually into different water bodies, however the impact of this activity is not assessed appropriately. Hence, this necessitates proper management, monitoring, assessment, and treatment of pollutants discharged into water bodies. Aside from conventional pollutants like heavy metals, nutrients, microbial pollutants and priority pollutants, other emerging pollutants, only newly revealed or recently monitored, are pollutants of increased concern and are known as contaminants of emerging concern (Rodriguez-Narvaez et al., 2017).

Contaminants of emerging concern (CECs) are manmade or even natural chemicals; they are usually not properly monitored or detected despite their accumulation in water bodies. They can, thus, cause environmental and health adverse effects (Geissen et al., 2015). It is extremely difficult to confine these pollutants to a list; the reason behind this difficulty is the daily increasing number of newly introduced chemical products for use by humans (Rodriguez-Narvaez et al., 2017). The registered number of such chemicals, which include pharmaceuticals, personal-care products, pesticides, biocides and industrial chemical compounds, reaches up to 100 million. Unfortunately, the number is still growing by an average rate of 4000 new chemicals per day. Out of this, an estimated number of 30,000 to 50,000 chemicals are present in daily used products. The

`

concluding remark is that these chemicals are now present everywhere, i.e., polluting air, food chains and water bodies (Dulio et al., 2018).

Antibiotics are one type of pharmaceuticals which proved to be useful for humans in combating pathogens. However, the abuse as well as the global increase in their consumption have led to the production of antibiotic resistant pathogens. Eventually, this would lead to unproductive therapeutic functions of this category of medicines (Rutgersson et al., 2014). It was also established that antibiotics have individual as well as combined toxic effects to aquatic organisms (González-Pleiter et al., 2013). Antibiotics were also found to have potential to accumulate in soil sediments (Küster & Adler, 2014), ultimately, inducing toxicity to soil dwelling organisms (Kümmerer, 2008). The effect of pharmaceuticals in drinking water is not yet well understood due to their extremely low concentrations, however, the synergetic effect of the mixtures of these drugs poses an alarming threat (Patel et al., 2019). Levofloxacin (LV) is an antibiotic which belongs to the family of fluoroquinolone (FQ) antibiotics. It is a third generation FQ antibiotic, and it is characterized by high antibacterial activity specifically against streptococci, when compared to former generations, and against broad range of other microorganisms. FQs are excreted from human body unmetabolized, i.e., about 20–80% of their pharmacologically active ingredients are discharged into sewage systems mainly from hospitals and pharmaceutical plants without being metabolized (T. M. Darweesh & Ahmed, 2017). Since pharmaceuticals possess a potential to bind to receptors in living organisms, then, the existence of this un-metabolized LV is a real threat to the living organisms and the environment (Patel et al., 2019). The increased exposure of bacteria to LV could increase the adaptation of these bacteria to LV and result in an increase in number of deaths in humans. The adverse effect of LV goes beyond human beings to include aquatic lives. For instance, the exposure of fish embryo to LV for only 24 h could cause it to perish. It has also

`

been reported that LV can hinder the growth of algae (Altaf et al., 2021). The concentrations of LV reported in literature in different water bodies varied greatly, for instance, a very high concentration of 6.2 mg/L was reported in a wastewater stream in Lahore, Pakistan, whereas very low concentrations of 170−2168 ng/L were reported in a river in Japan (Patel et al., 2019). Other literature reported concentration of LV in Baghdad, Iraq to be 0.414 μg/L (Mahmood et al., 2019).

Dyes are chemical compounds employed in colorizing various types of materials. It is widely used in textile, tanning, pharmaceutical, paper and printing industries. The annual world production of dyes reaches 700,000 tons, of which nearly 15-20 % is lost during the process of dying. This amount of washout usually reaches various waterbodies, and thus, causes serious health and environmental hazards. Dyes are persistent in the environment, which makes their biodegradation difficult (Nyankson & Kumar, 2019). Rhodamine B (RB) is a basic cationic dye, and it is one of the most important and commonly used type of dyes (Mohammadi et al., 2010; Mousavi et al., 2021). It has been extensively used as a colorant, imparting red color, in the textile, food, pharmaceutical, and cosmetic industries (Baldev et al., 2013; Özkantar et al., 2017). It is also used as a biologically staining material in biomedical laboratories (Mohammadi et al., 2010). Owing to the presence of aromatic rings, RB is highly stable. This stability leads to almost no biodegradation of this dye, consequently, this dye stays for a longer period of time in the environment causing health and ecological problems (Baldev et al., 2013). The adverse effects caused by RB vary from mild to extremely life-threatening conditions. Eyes, skin and respiratory tract irritations can be named as mild effects of the RB (Soylak et al., 2011). Serious and life-threatening conditions caused by drinking water polluted with RB include tissue borne sarcoma (extremely carcinogenic) and congenital cancer (Özkantar et al., 2017; Shen & Gondal, 2017). RB is also considered to be teratogenic and mutagenic (Baldev et al., 2013; Mousavi et al., 2021). The

`

effect of RB extends also to aquatic lives since it has a potential to shield sun light from aquatic lives and block up transfer of oxygen (Mousavi et al., 2021).

1.2 An Overview of Methods of Treatment

The issues mentioned in the previous section necessitate the removal of these hazardous pollutants. Towards this end, many techniques have been developed and employed for the removal of pharmaceutical contaminants and dyes from water bodies. Techniques for removal of pharmaceutical contaminants include conventional drinking water and wastewater treatment, chlorination, nano-filtration, reverse osmosis, advanced oxidation and adsorption (Patel et al., 2019). However, these techniques suffer from many drawbacks. Conventional drinking water treatments plants are comprised of many processes which include flocculation, filtration, and disinfection. All these process stages were found to be ineffective in removing the pharmaceutical contaminants (Baldev et al., 2013). For instance, Mahmood et al., 2019 reported that 40 % of LV was still present after treatment of the raw water in a drinking water treatment plant. The conventional wastewater treatment has a limited capacity in removing pharmaceutical contaminants due to failure of many drugs to adsorb on activated sludge. Chlorination technique has the ability to remove only very reactive drugs, however, the products are poisonous making it less favorable. Nano-filtration and reverse osmosis are characterized by very high operational costs (Luo et al., 2014). Photocatalysis is very efficient, however, it is very difficult to scale it up to treat large amount of water. Advanced oxidation is also characterized by high removal rate, but the formation of highly toxic products is the main obstacle for applying this technique. Adsorption offers a promising alternative, as it provides high removal rate, relatively low operating costs, ease of operation, simplicity of design and it does not generate poisonous byproducts. However, developing a cost effective highly efficient adsorbent is a challenge (Patel et al., 2019).

`

1.3 Cement Kiln Dust (CKD)

CKD is a byproduct of cement industries, and it is one of the contributors to air pollution. It is mainly composed of calcium oxide (up to 66 %) and silica (up to 22 %) (Meo, 2004). The huge amount of CKD produced daily, for instance 7500 tons/day in Egypt, makes its proper disposal difficult, while its recycling is mainly hindered by its high alkali content (i.e., Na_2O and K_2O). Thus, it is usually disposed of in deserts, where it is easily blown back to urban areas and ends up inhaled by human beings (HHM. Darweesh, 2020). The particle sizes of CKD lie within the respirable range (0.05-0.5μm) (Meo, 2004), hence, it is easily inhaled and cause many diseases like silicosis, pneumoconiosis, and lung cancer (HHM. Darweesh, 2020; Meo, 2004; Adeyanju & Okeke, 2019).

1.4 Aim of Study

This work aims at developing an adsorption process that removes LV and RB efficiently from water using a composite adsorbent synthesized from an industrial waste, CKD. Hence, the first part of this work is solely dedicated to the use of CKD as a precursor to produce a nanocomposite of hydroxyapatite and carbon (HAP-C). HAP-C is then characterized by using FTIR, BET, XRD, TEM, TGA, and zeta potential measurements. The second part is intended to investigate the performance of the synthesized nanocomposite in the removal of the contaminants in question. In addition, the performance of the adsorbent is also evaluated via conducting adsorption isotherm, kinetics and thermodynamic studies, while the mechanism of adsorption is suggested.

This is the first report, to the best of our knowledge, to utilize CKD waste for the synthesis of HAP or HAP-C as a value-added product. In the due process, a novel approach is used for the synthesis of the nanocomposite, whereby a single precursor incorporating carbon and calcium is used. In previous literature, two precursors were used: one for carbon and one for calcium. Then,

`

a simultaneous process for modification of the carbon and synthesis of the HAP takes place. The advantage of this approach is the reduction in the number of steps undergone for modifying carbon and exploiting it in chelating the calcium from CKD, which consequently leads to reduction in the cost and environmental impact of the synthesis process. This approach is, therefore, in compliance with the UN sustainable development goal, SDG #12 which is concerned with proper management of resources. The work in this thesis is also in line with SDG #6 on clean water, and with the concept of zero waste management and circular economy.

`

Chapter 2

`

2. Literature Review

2.1 Overview

HAP is a compound of the calcium phosphate family with a chemical formula $Ca_{10}(PO_4)_6(OH)_2$ (Ferri et al., 2021). It occurs naturally in the structures of the teeth and bone of vertebrates, plants, seashells, algae, eggshells, and limestone. HAP has a hexagonal crystal structure and it is characterized by biocompatibility, bioactivity, nontoxicity and good mechanical properties (Ferri et al., 2021; Szcześ et al., 2017). Figure 1a and b depicts the 2-dimensional and 3-dimensional structure of HAP, respectively.

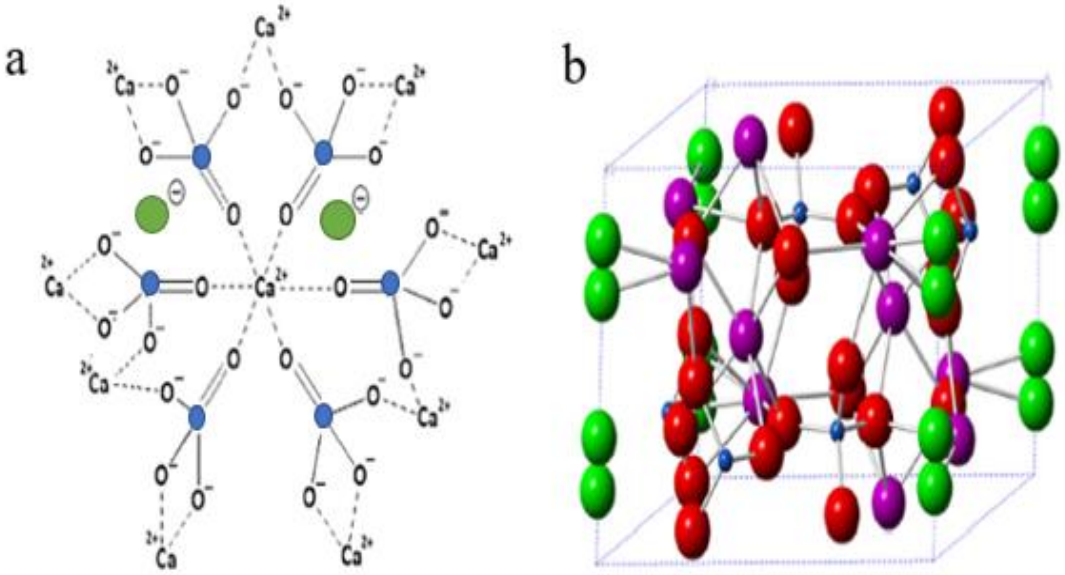

Figure 1 HAP structures a) two-dimensional (Pai et al., 2021), and b) three-dimensional (Qi et al., 2017)

(Green= OH, Red= O, Blue= P and Purple= Ca)

`

Calcium phosphates are distinguished amongst themselves via what is known as the calcium to phosphorous ratio (Ca/P). The stoichiometric Ca/P ratio of HAP is 10:6 or simply expressed as 1.67. Other non-stoichiometric HAPs are within the range of 1.5 and 1.9 (Agbeboh et al., 2020).

Calcium phosphates with Ca/P ratio between 1.5-1.6 are called calcium deficient HAPs. Their chemical formula is given by $Ca_{10-x}(PO_4)_{6-x}(HPO_4)_x(OH)_{2-x}$, where x lies between 0 and 1 (Agbeboh et al., 2020). Table 1 illustrates different types of calcium phosphates with their crystal structures, solubility and Ca/P ratios.

`

Table 1 Calcium phosphate compounds with their Ca/P ratios, crystal structure, and pKs values (Agbeboh et al., 2020; Akram et al., 2014; Szcześ et al., 2017)

Compound Name	Chemical formula	Ca/P Ratio	Crystal Structure	pK_s at 25°C
Monocalcium-phosphate monohydrate	$Ca(H_2PO_4).2H_2O$	0.5	Triclinic	1.14
Monocalcium phosphate anhydrous	$Ca(H_2PO_4)_2$	0.5	Triclinic	1.14
Dicalcium phosphate anhydrous	$CaHPO_4$	1	Orthorhombic	6.9
Dicalcium phosphate dihydrate	$CaHPO_4.2H_2O$	1	Monoclinic	6.59
α-Tricalcium phosphate	$\alpha\text{-}Ca_3(PO_4)_2$	1.5	Monoclinic	25.5
β-Tricalcium phosphate	$\beta\text{-}Ca_3(PO_4)_2$	1.5	Rhombohedral	28.9
Calcium-deficient hydroxyapatite	$Ca_{10-x}(PO_4)_{6-x}(HPO_4)_x\ (OH)_{2-x}$	1.5-1.6	Hexagonal	85
Hydroxyapatite	$Ca_{10}(PO_4)_6\ (OH)_2$	1.67	Hexagonal	116.8
Fluorapatite	$Ca_{10}(PO_4)_6F_2$	1.67	Hexagonal	120
Tetracalcium phosphate	$Ca_4(PO_4)_2O$	2	Monoclinic	38-44

`

HAP is favored over the other calcium phosphates due to its thermodynamic, chemical and thermal stability, biocompatibility and structural flexibilities (Ferri et al., 2021; Sassoni, 2018). Hence, its applications extend from medical implants, drug delivery to water treatment (Agbeboh et al., 2020; Pai et al., 2021).

2. 2 Sources of HAP

HAP is either extracted from natural sources (biological) or synthesized using reagents. Biological sources include plants, mammalian bones, fish bones, egg shells and different types of sea shells (Akram et al., 2014). There are many methods used in the synthesis of HAP, these include sol gel, hydrothermal, mechanochemical, sono-chemical, emulsion method, microwave, spray pyrolysis, solution combustion, precipitation, coprecipitation, hydrolysis and solid state reaction method (Agbeboh et al., 2020; Pai et al., 2021).

2.2.1 Natural sources

2.2.1.1 Bone Sources

One of the major sources of HAP is animal bone. Animal bones are mainly composed of calcium compounds, these include HAP. Up to 67% of animal bones is composed of HAP and the rest is composed of organic matter and trace of other elements (Agbeboh et al., 2020). In the due process of extraction, the following procedure is used in almost all extraction processes of HAP from animal bones. The first step is thorough washing of the bones followed by boiling with distilled water, in order to remove impurities, blood, meat or tissues from the bones. The alkaline treatment follows to further dissolve the remaining proteins, oils, fats, and tissues. In the alkaline treatment, either NaOH or ClO^- could be employed. Afterward, the bones are dried and crushed and ball milled. Calcination is then used to completely remove any remaining organic matter and also to increase the crystallinity of the extracted HAP. In addition, calcination ensures the complete

`

destruction of any pathogens. Meanwhile, calcination usually causes a decrease in the mechanical strength of the HAP extracted and if a suitable calcination regime is not adopted, thermal decomposition can take place. Hence, it is of great importance to choose a suitable calcination regime. In this method, purity and particle size distribution of HAP extracted is affected by the calcination temperature as well as the bone condition (Agbeboh et al., 2020; Akram et al., 2014).

Extraction of HAP from animal bones has been extensively reported in literature. The type of bones used varied from bovine to human bones (Nasser et al., 2009; Sobczak A, Kowalski Z, 2009; Kusrini, Eny & Sontang, 2012; A. Ruksudjarit et al., 2008; Bahrololoom, et al., 2009;Yoganand et al., 2011; Figueiredo et al., 2010). The resulting HAP, thus, varied greatly in its size distribution, particle size and regularity of the structure of its particles. Another drawback was the presence of traces of metals, which resulted in a non-stochiometric HAP (Agbeboh et al., 2020).

2.2.1.2 Biogenic Sources

Biogenic materials include eggshells, snail shells, mussel shells, nacre, coral, oyster shell, sea shells and sea urchin (Agbeboh et al., 2020; Akram et al., 2014; Shavandi, Bekhit, Ali, et al., 2015). Eggshells are composed of 94 % calcium carbonate. Millions of tons of eggshells are discarded into the environment as waste material which makes it cheap and easily available. Generally, methods of synthesis of HAP from shells start with washing the steam or even boiling water in order to remove any organic impurities. This is followed by heating to convert calcium carbonate to calcium oxide and to further remove any remnant organic matter, then it is reacted with a precursor of phosphate to form the HAP. The type of reaction varies from simple precipitation to microwave assisted one. Table 2 summarizes HAP synthesized from biogenic sources reported in literature and the respective type of synthesis used.

`

Table 2 HAP synthesized from biogenic sources and the respective method of synthesis

Source	**Method**	**Particle size (diameter, nm)**	**Ca/P ratio**	**Reference**
Egg shell	Precipitation	-	1.65	(S. J. Lee, 2003)
Coral shell	Hydrothermal and solvothermal	-	-	(Kim, 2005)
Egg shell	Microwave	50	1.67	(Kumar, 2007)
Egg shell	Precipitation	35	-	(Sanosh et al., 2009a)
Egg shell	Precipitation	50	1.67	(Nayar & Guha, 2009)
Sea Urchin	Hydrothermal	-	-	(Alvarez-lloret et al., 2010)
Egg shell	Precipitation	-	-	(Meski et al., 2010)
Nacre	Hydrothermal	5000	-	(Y. Guo et al., 2011)
Egg shell	Hydrothermal	-	-	(Ying Zhang et. al., 2011)

`

Oyster shell	Solid state reaction	-	-	(Wu et al., 2011)
Egg shell	Hydrothermal	20-40	-	(Zhang et al., 2011)
Egg shell	Precipitation	5	1.425	(Taylor et al., 2011)
Egg shell	Solvothermal	15-35	-	(Songnan et al., 2012)
Egg shell	Hydrothermal	60	-	(Elizondo-Villarreal et al., 2012)
Egg shell	Precipitation	30	1.67	(Goloshchapov et al., 2012)
Mussel Shell	Precipitation	-	1.66	(J.H. Shariffuddin, M.I. Jones, 2013)
Egg shell	Solid state reaction	-	2.2	(Ho et al., 2013)
Egg shell	Hydrothermal	-	1.57–1.77	(Wu et al., 2013)
Egg shell	Hydrothermal	41	-	(Chaudhuri et al., 2013)
Egg shell	Precipitation	10	-	(Ibrahim et al., 2013)
Snail shell	Ultrasound-Microwave	460-2500	-	(Putro et al., 2014)
Mussel Shell	Microwave	30-70	1.65	(Shavandi, Bekhit, Ali, et al., 2015)

`

Mussel Shell	Sonochemical	12-18	-	(Edralin et al., 2017)
Egg shell	Precipitation	31.5	1.63	(Khandelwal & Prakash, 2016)
Egg shell	Annealing/Precipitation	4-6	1.63	(Adeogun et al., 2018)

`

One disadvantage of biogenic sources is that they require harsh chemicals to remove organic impurities. In addition, these sources usually produce non-stoichiometric HAP, which also suffers from the presence of trace elements impurities (i.e., the produced HAP is not always pure).

2.2.1.2 Plant Sources

Plants can be used in the production of HAP via two means, it can either be a source of calcium or it can be a source of HAP. Plants like marine algae (*Rodophycophyta* class), *C. officinals*, and *Phymatolithon calcareum* are considered calcium carbonate rich plants, whereas plants such as mint, Khat (*C.edulis*), trifolium, green tea, and basil contain HAP in their structures (Agbeboh et al., 2020; Akram et al., 2014). The parts of the latter plants that contain the highest amount of HAP were found to be the leaves (Agbeboh et al., 2020).

Kusmanto and co-workers used *Phymatolithon calcareum* algae as sources of calcium carbonate (Kusmanto et al., 2008). The first step was to extract the calcium source; hence, the algae was first pyrolyzed into $CaCO_3$/CaO. Then, in the second step the calcium precursors were reacted with a source of phosphorus via a hydrothermal route, and the characterization tests confirmed the partial formation of HAP (Kusmanto et al., 2008).

Synthesis of HAP from *C. officinals* was reported by Walsh and co-workers (Walsh et al., 2008). The carbonate was first extracted from this plant by pyrolysis, then, the extracted calcium precursor was reacted with ammonium dihydrogen phosphate for 12 h at 100°C. As the previous approach, the hydrothermal method was also used here. In order to produce HAP with the required specifications, the following factors must be taken care of: i) decomposition of the carbonate, ii) the original morphology of the algae in use, and iii) the removal of organic impurities prior to the pyrolysis step (Walsh et al., 2008).

`

Shaltout and colleagues used mint, Khat, trifolium, green tea, and basil as sources of HAP (Shaltout et al., 2011). These plants contain in their structure calcium hydroxide, HAP and traces of other elements and compounds. The following procedure was followed to extract the HAP from the leaves and trunks of the plant. The plant was first washed and dried, then it was subjected to grinding and milling. Finally, milled plants were subjected to heating in a muffle furnace. FTIR, TGA, DTG and XRD characterization confirmed the extraction of HAP (Shaltout et al., 2011). Plant derived HAP tend to be thermally unstable, this could be attributed either to partial conversion of precursors to HAP or to the presence of carbonate ions in the raw material (Akram et al., 2014).

2.2.2 Synthetic sources

Synthetic sources include the use of various synthetic precursors of calcium and phosphorus. The use of these precursors is dependent on the method used to synthesize the HAP. The synthesis of HAP for various purposes requires control over the Ca/P ratio, the structure and shape of the particles, the size distribution of the particles, surface properties and the purity of the product. Hence, to accomplish these requirements it is of utmost importance that the synthesis method and the synthetic materials employed in its production are strictly controlled (Akram et al., 2014). The synthesis methods are categorized into dry, wet and high temperature methods (Mohd Pu'ad et al., 2019). The following sections briefly discuss these methods.

`

2.3 Chemical Synthesis of HAP

2.3.1 Solid-State method

In this method, the solid precursors of calcium and phosphorus are milled and calcined in a certain ratio to produce HAP. The mechanism of the synthesis is mainly dependent on the diffusion of reactants in addition to the heat which is responsible for the initiation of the chemical reaction (Mohd Pu'ad et al., 2019). The advantages of this method are the relatively low cost of process, relatively large particle sizes (10^{-6} m order of magnitude) and small number of chemicals used, while the disadvantages are presence of many calcium phosphate phases, high sintering temperature and time (Agbeboh et al., 2020; Mohd Pu'ad et al., 2019; Shavandi et al., 2015).

2.3.2 Mechanochemical method

A mechanochemical method is a method that uses mechanical processes such as shear stress, friction, grinding, milling, and compression to initiate a chemical reaction. (Mohd Pu'ad et al., 2019). In this method, the process is conducted in a closed vessel, and the impact of the mechanical forces on the solid reactants causes an increase in temperature which, in turn, enhances the diffusion and the kinetics of the chemical reaction. Thus, the mechanochemical route is always used as an alternative to the solid-state route. The advantages of this method lies in its ease of operation, low-cost, conduction at room temperature, and production of nano-sized HAP. Meanwhile, this process has serious drawbacks, including the non-stochiometric Ca/P produced, phase impurity and high crystallinity (Agbeboh et al., 2020; Mohd Pu'ad et al., 2019).

2.3.3 Precipitation

The precipitation method is one of the oldest and simplest techniques employed for synthesis of HAP. This technique is usually performed through a series of steps; at the beginning, calcium and phosphorus precursors are mixed, usually in a liquid phase using a solvent. The following step

`

involves adjusting the pH and the temperature of the solution containing the precursors. Afterward, agitation of the solution takes place for a certain period. In the last step, HAP powder is separated from the liquid phase then thoroughly washed to remove any impurities. The source of phosphorus in this method (usually orthophosphoric acid) is added dropwise to avoid abrupt change in pH (Agbeboh et al., 2020; Mohd Pu'ad et al., 2019; Shavandi et al., 2015). The advantages of the precipitation technique are its low-cost process, utilization of less chemicals, production of nano-sized HAP, and suitability for mass production, while the disadvantages are sensitivity to pH, poor crystallization, and diverse morphology (Agbeboh et al., 2020; Shavandi et al., 2015).

2.3.4 Sol-gel method

Sol is the dispersion of colloidal particle in a solvent while gel is a porous three-dimensional continuous solid network with a continuous liquid phase. In this process, a precursor species with a leaving group (an or group of atoms that breaks from a substrate during elementary step of a reaction) is dissolved into a certain solution, then after the molecules are cross-linked (polymerized) the sol is formed. This is followed by a digestion step and an aging step. Finally the excess solvent is dried and the organic material is eliminated, forming a crystal structure (Pai et al., 2020; Shavandi et al., 2015). The advantages of this technique is the purity and the low temperature and pressure requirements, while the main disadvantage is the high cost of starting materials in addition to the diversity of morphology of the HAP produced. (Agbeboh et al., 2020; Shavandi et al., 2015). This method also suffers from lack of reproducibility (Shavandi et al., 2015).

2.3.5 Hydrothermal method

In this method, the chemical reaction is conducted at elevated pressure and temperature (slightly above boiling point of the water) in a closed vessel/ autoclave. The increased pressure and

`

temperature causes an increase in reactivity (Mohd Pu'ad et al., 2019; Shavandi et al., 2015). This technique produces highly crystalline HAP with enhanced mechanical and morphological properties, while its main disadvantage is associated with high cost owing to the high temperature and pressure requirements (Agbeboh et al., 2020; Mohd Pu'ad et al., 2019; Pai et al., 2020; Shavandi et al., 2015).

2.3.6 Sonochemical method

In this technique, the salts of calcium and phosphorus are subjected to sonication during or after mixing. At the end of the reaction, HAP is separated via centrifugation. The sonication enhances the kinetics of the reaction and makes it energy efficient (Pai et al., 2020), however it is still a costly process.

2.3.7 Microwave

Microwave irradiation is used to enhance the reaction between the calcium precursor and phosphorus precursor. This usually takes place at a reduced time when compared to conventional methods. Microwave irradiation is characterized by uniformity in dissipating heat, this will lead to homogenous distribution of temperature and pressure over the reactants. As a result, better control over the crystal size of the HAP can be achieved, which, in turn, affects the morphology of the HAP product. For instance, the HAP nano-rods can be converted to prism like structures by just increasing the temperature (Shavandi, Bekhit, Sun, et al., 2015).

2.3.8 Combustion

In this method, the mixture of reactants is heated at low temperature at the beginning followed by an abrupt increase in temperature, usually this takes place by mixing the fuel with the reactants. At the end of the reaction, the mixture is subjected to rapid cooling. The process of rapid cooling brings about nucleation and causes the crystal growth to stop. This technique produces a

`

stochiometric HAP, however, it suffers from presence of other phases with HAP in addition to the high- cost of operation (Mohd Pu'ad et al., 2019).

2.3.9 Pyrolysis

Pyrolysis or spray pyrolysis is conducted via the spraying of a precursor solution into a hot zone of an electric furnace by an ultrasonic generator. Then, gases and vapors are generated, and a chemical reaction takes place. After the precursors are completely vaporized, nucleation takes place and is followed by gas phase growth of nanoparticles. Ultimately, this results in the formation of an aggregated form of powder. This method suffers from increased process costs and presence of different phases along with HAP (Mohd Pu'ad et al., 2019).

Table 3 summarizes the reported synthesis methods of HAP with their respective calcium and phosphorus precursors.

`

Table 3 Synthesis methods of HAP with their respective calcium and phosphorus precursors

Type of method	**Calcium and Phosphorus precursors**	**Reference**
Solid-State	Ca $(OH)_2$ and β-TCP	(Rao et al., 1997)
	CaO and P_2O_5	(Pramanik et al., 2007)
	Ca $(NO_3)_2.4H_2O$ and $(NH_4)_2HPO_4$	(X. Guo et al., 2013)
	$CaCO_3$ and $CaHPO_4$	(Arkin et al., 2015)
Mechanochemical	CaO and $CaHPO_4$	(Yeong et al., 2001)
	$CaCO_3$ and $Ca_2P_2O_7$	(Rhee, 2002)
	$CaCO_3$ and $CaHPO_4.2H_2O$	(Shu et al., 2005)
	Ca $(OH)_2$ and P_2O_5	(Fathi & Zahrani, 2009)
Precipitation	Ca $(OH)_2$ and H_3PO_4	(Afshar et al., 2003)
	Ca $(NO_3)_2.4H_2O$ and $(NH_4)_2HPO_4$	(Mobasherpour et al., 2007)
	Ca $(OH)_2$ and H_3PO_4	(Yelten-Yilmaz & Yilmaz, 2018)
	Ca $(NO_3)_2.4H_2O$ and Na_3PO_4	(Sundarabharathi et al., 2020)
Sol-gel	Ca $(NO_3)_2.4H_2O$ and H_3PO_4	(Sanosh et al., 2009b)
	Ca $(NO_3)_2.4H_2O$ and P_2O_5+ ethanol	(Agrawal et al., 2011)

`

	$Ca(NO_3)_2.4H_2O$ and $C_6H_{15}O_4P$	(Amiri et al., 2017)
	$Ca(NO_3)_2.4H_2O$ and Na_2HPO_4	(Phatai et al., 2019)
Hydrothermal	$CaCl_2$ and K_2HPO_4	(Wang et al., 2006)
	$CaCl_2$ and H_3PO_4	(Zhang et al., 2011)
	$Ca(NO_3)_2.4H_2O$ and $(NH_4)_2HPO_4$	(Nagata et al., 2013)
	$Ca(NO_3)_2$ and $(NH_4)_2HPO_4$	(Buitrago-Vásquez & Ossa-Orozco, 2018)
	$Ca(NO_3)_2.4H_2O$ and $Na_2HPO_4.12H_2O$	(Y. Xu et al., 2018)
	$Ca(OH)_2$ and $(NH_4)_3PO_4$	(López-Ortiz et al., 2020)
Sonochemical	$Ca(NO_3)_2.4H_2O$ and $(NH_4)_2HPO_4$	(Utara & Klinkaewnarong, 2015)
Microwave	$CaCl_2$ and Na_2HPO_4	(Xiao et al., 2018)
Combustion	$Ca(NO_3)_2$ and $(NH_4)_2HPO_4$	(Sasikumar & Vijayaraghavan, 2008)
	$Ca(OH)_2$, $Ca(NO_3)_2$ and NH_4H_2PO4,	(R. Narayanan et al., 2009)
	$Ca(C_2H_3O_2)_2$ and $(NH_4)_2HPO_4$	(Kavitha et al., 2014)

`

	$Ca(NO_3)_2.4H_2O$ and $(NH_4)_2HPO_4$	(Canillas et al., 2017)
Pyrolysis	$Ca_3(PO_4)_2$, $Ca(NO_3)_2.4H_2O$ and $(NH_4)_2HPO_4$	(Cho & Rhee, 2012)
	$Ca(NO_3)_2$, $(NH_4)_2HPO_4$,	(Nakazato et al., 2012)
	$Ca(OH)_2$, H_3PO_4	
	$Ca(C_2H_3O_2)_2$, $(CH_3)_3PO_4$	
	$Ca(C_2H_3O_2)_2$ and $(NH_4)_2HPO_4$	(Widiyastuti et al., 2014)

`

4. **HAP- Carbon composite and its application in water treatment**

HAP as a major inorganic compound has received increased attention due to its high biocompatibility, bioactivity, non-toxicity and physicochemical properties (Ferri et al., 2021; Long et al., 2019). It has a high capacity to adsorb inorganic materials, especially heavy metals (Ferri et al., 2021). Nevertheless, the efficiency of adsorption of pollutants on the surface of HAP is usually hindered by the following factors. HAP possesses lower capacity to adsorb organic pollutants compared to inorganic pollutants (Ferri et al., 2021). HAP tends to aggregate causing the clogging of active sites and reduction of surface area which, in turn, leads to decline in the adsorption capacity. The aggregation is attributed to the high energy of the surface of HAP caused by van der Waals forces (Liao et al., 2022; Long et al., 2019). Another problem associated with HAP adsorption is the extreme difficulty of separating the adsorbates from the surface of HAP, and hence inability to re-use the adsorbent (Long et al., 2019). Therefore, to address these deficiencies of HAP adsorbent, HAP is usually incorporated into a composite system. For instance, Kede and co-workers coated HAP with polymeric sponges to enhance the removal of lead and cadmium (Kede et al., 2012), while Wang and colleagues loaded HAP on carbon nanotubes to remove methylene blue (Wang et al., 2017). Su and co-workers functionalized HAP with graphene oxide to remove uranium from aqueous media (Su et al., 2021). Even though, these composites have enhanced the adsorption performance of HAP, nevertheless, they suffered from complex synthesis processes as well as increased costs. In order to overcome these problems, carbon as a low cost environmentally friendly material, is incorporated in a composite form with HAP. Carbon is characterized by large surface area and porosity, ability to disperse in aqueous media, and high functionality (Liao et al., 2022).

`

Fernando and co-workers synthesized a HAP-C composite via precipitation (Fernando et al., 2015). Stoichiometric amounts of $(NH_4)_2HPO_4$ and $Ca(NO_3)_2.4H_2O$ were mixed and stirred vigorously at 60°C for 3h to achieve Ca/P ratio of 1.67. The pH was maintained at 10 with the use of ammonium hydroxide, then granular activated carbon (GAC) was immediately added. The precipitate was vacuum filtered and washed then heated at 80°C for 3 h. The final product was whitish gray granules of HAP coated on granular activated carbon. Then, the composite was employed in removal of lead. The composite had a nanorod structure with a diameter of 50-80 nm range and length of 250 nm. The optimum pH was 6 and contact time was 2 h, and the adsorption mechanism was suggested to be via Ca^{+2} ion exchange. The Langmuir adsorption capacity was found to be 83.3 mg/g (Fernando et al., 2015). The same synthesis procedure was adopted in another study by Udayakantha and co-workers to prepare a composite of GAC coated with HAP (Udayakantha et al., 2015). However, the composite was also coated with curcumin to induce an antibacterial property for water purification (Udayakantha et al., 2015). The same composite was prepared by Long and colleagues who used ammonium dihydrogen phosphate and calcium chloride in addition to GAC to produce HAP-C composite (Long et al., 2019) for lead removal from aqueous solutions. The maximum adsorption capacity for lead was 416.67 mg/g at pH 5, 2 h contact time and 25 °C, which is very high compared to other adsorbents and corresponds to a maximum removal of 78.94% (Long et al., 2019). In another study, Rout et al., synthesized HAP-AC composite for the purpose of removal of uranium from water systems (Rout et al., 2020). The removal efficiency reached up to 98% (Rout et al., 2020).

Liao et al. also studied the effect of carbon ratio on the performance of HAP-C composite. The composite was synthesized by utilizing swine manure as a source of carbon and was used for uranium removal (Liao et al., 2022). The best performance was achieved by the composite with

`

10 % mass percent of carbon. The removal efficiency of the composite after five consecutive regeneration cycles was 93% at pH 3 and 25°C, illustrating the composite stability and reusability. The equilibrium was reached after 5 min, and the Langmuir maximum adsorption capacity was 834.8 mg/g (Liao et al., 2022).

In all of the reported studies with the exception of the work of Liao and colleagues, the carbon was first modified or activated before adding it to the reaction medium for the synthesis of HAP. However, in case of Liao et al. work the carbon was pyrolyzed after the synthesis of the HAP. In our study, a similar approach is adopted with some modifications.

2.4 HAP and HAP-C for CECs removal

HAP-based adsorbents have been employed in the removal of CECs. Typical studies from literature that focus on using HAP alone or HAP-carbon composites for the removal of CECs is discussed in this section.

Chen et al. employed HAP for the removal of two different pharmaceuticals which belong to the fluoroquinolone antibiotics family, these were norfloxacin (NOR) and ciprofloxacin (CIP) (Chen et al., 2015). The reported removal percentages were 51.6% and 47.3% for NOR and CIP, respectively. The highest removal for both antibiotics was achieved at pH 6 and the equilibrium was attained after 20 min. The Langmuir maximum adsorption capacity was 1.486 and 1.272 mg/g for NOR and CIP, respectively (Chen et al., 2015). Huang et. al. used HAP for removing ofloxacin (OFL) and triclosan (TCS) (Huang et al., 2016). The optimum pH for removal of OFL and TCS was 4.5 and 2, respectively, and the equilibrium was attained after 0.5 h. The respective Langmuir maximum adsorption capacity was 29.15 and 133.33 mg/g for OFL and TCS at 45°C (Huang et al., 2016). Ciobanu and Harja reported the removal of LV from aqueous media with a removal

`

efficiency that reached up to 95.24 and 87.32 % for uncalcined and calcined HAP, respectively (Ciobanu & Harja, 2018). These efficiencies were attained at pH 7 with high adsorption capacity of 157.09 and 124.52 mg/g for uncalcined and calcined HAP, respectively (Ciobanu & Harja, 2018).

In the study conducted by Yuan et al., the effect of pH and metal ions on the interaction of oxytetracycline (OTC) onto HAP was evaluated (Yuan et al., 2019). The study concluded that that adsorption of OTC on HAP was highly affected by the pH and metallic species present in the aqueous media. The highest amount of OTC adsorbed on HAP was obtained at pH 8, with a Langmuir maximum adsorption capacity of 78.27 mg/g, and the equilibrium was attained after 2 h. This capacity was significantly affected by the presence of metal ions (0.25 mM of Cu^{2+}), i.e., it increased to 169.18 mg/g (Yuan et al., 2019). Another antibiotic, cephalexin (Ceph) was removed from aqueous media using HAP in the study reported by Alhasan et al., (Alhasan et al., 2022). The highest removal percent observed was 70.7% at pH 7 and after 1 h time, and Langmuir maximum adsorption capacity was 16.67 mg/g (Alhasan et al., 2022).

Dyes were also removed by HAP and HAP composites. Hou and colleagues used HAP-chitosan composite to remove congo red (CR) from aqueous solutions (Hou et al., 2012). The Langmuir maximum adsorption capacity reported for CR in this study was 769 mg/g (Hou et al., 2012). Wei and co-workers used poorly crystalline HAP for removal methylene blue from aqueous solution (Wei et al., 2015). The Langmuir maximum adsorption capacity was 14.27 mg/g at 10°C and 12.94 mg/g at 25°C, while the highest percent removal was recorded at pH 10 (Wei et al., 2015). Oladipo and Gazi used a composite of HAP-alginate for removing simultaneously RB and nickel ion (Oladipo & Gazi, 2016). The highest removal for RB was 96%, and the highest adsorption capacity was 480 mg/g at pH 7 and a dose of 20 g/L (Oladipo & Gazi, 2016). Adeogun et al., used HAP for

`

adsorbing yellow 4 dye (Y4D) (Adeogun et al., 2018). The highest removal was observed at pH 6, and the Langmuir adsorption capacity was 127.9 mg/g (Adeogun et al., 2018). Other workers utilized HAP-C composites for the removal of dyes along with heavy metals. Ferri and colleagues synthesized a HAP-C composite via chemical precipitation and studied the simultaneous removal of methylene blue dye, copper and nickel (Ferri et al., 2021). The study also reported the effect of the percent ratio of HAP to carbon on the surface properties of the composite. The adsorption experiments were conducted at pH 5.5, contact time 2 h and 30°C, the results varied depending on the carbon content in the composite. For instance, the highest percent (100 %) removal of methylene blue in the single system belonged to the composites with 8, 12, and 16 % carbon content, at the same time the highest removal of nickel was only 44.7% at relatively close initial concentrations of both adsorbates. All of the composites with different ratios of carbon showed very high removal percentages for copper, ranging for 96.4 to 99.8% (Ferri et al., 2021).

HAP-C composites were employed for removing CECs. Li and colleagues used biochar stabilized HAP for the removal of tylosin (TY), sulfamethoxazole (SMX) and copper (Z. Li et al., 2020). The Langmuir adsorption capacity was 118.84 and 128.77 mg/g for TY and SMX, respectively (Z. Li et al., 2020). Zhao and co-workers also used HAP-biochar for the removal of heavy metals (Cu, Cd, and Pb), carbamazepine (CBZ) and tetracycline (TC) (X. Zhao et al., 2022). The Langmuir maximum adsorption capacity was 168.9, and 105.1 mg/g for CBZ and TC, respectively at pH 6 and 20°C (X. Zhao et al., 2022).

`

Chapter 3

`

3.Theoretical Background

3.1Characterization techniques

3.1.1 X-ray Fluorescence (XRF)

X-ray fluorescence is an analytical non-destructive spectroscopic technique used widely in elemental analysis. In general, the interaction of x-rays when it falls can take place in three different ways, the first one is the x-ray being absorbed, the second is the x-ray being scattered and the third one is the x-ray being transmitted through the material. In XRF analysis the interaction of x-ray occurs as absorption, where the absorbed x-ray causes an inner shell electron to be ejected. This causes the atoms to be intrinsically unstable due to the presence of a vacancy in an inner electron shell leading to an immediate decay to a more stable electronic state. The decay here is the transition of an outer shell electron to fill this inner shell vacancy. When the electrons fall through the potential energy gradient to the inner shell, energy is lost through emitting a fluorescent x-ray photon, and thus, stability of the atom is regained. The emitted fluorescent x-ray is a characteristic property of each element (Perrone et al., 2014; Potts, 1995). Figure 2 illustrates the process of fluorescent x-ray emission.

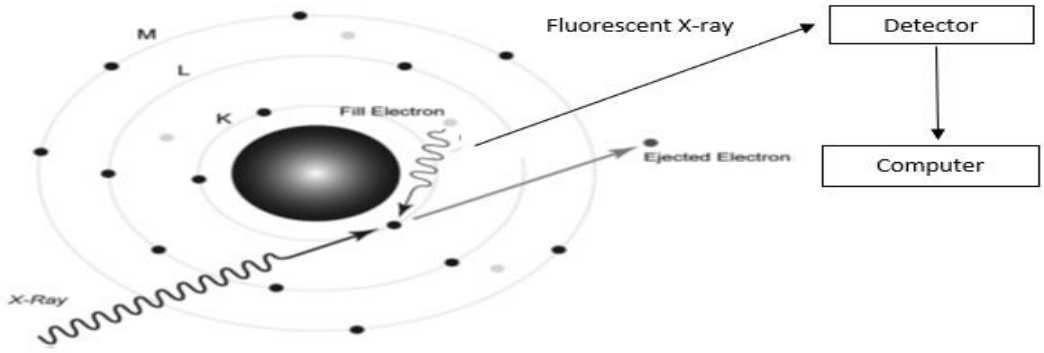

Figure 2 Scheme of fluorescent x-ray emission (Perrone et al., 2014).

`

3.1.2 X-ray powder diffraction (XRD)

XRD is a technique used to study geometrical structure and phases of the crystalline substances. This technique is a non-destructive technique, and it was used in this study as a confirmatory test for the synthesized materials. Crystalline materials are characterized by highly ordered three-dimensional geometrical arrangement of ions, atoms, or molecules in a coherent symmetry in periodically repeating units (Tong, 2019).

Samples are placed in a zero-background holder and then are subjected to a beam of x-ray, with a wavelength comparable to inter atomic distances in the crystalline material. The sample in the holder rotates so that the sample is subjected to the beam from all sides at a specific angle. The coherent scattered radiation is detected by an x-ray detector which converts it into signals. A computer that receives the signals from the detector plots intensity counts versus diffraction angle (Lanzirotti et al., 2010; Raja et al., 2022). The detected scattered radiation peaks at particular values of 2θ obey Bragg's law:

$$n\lambda = 2d\sin\theta \qquad (3.1)$$

where, n is an integer, λ is the wavelength, d is interplanar spacing, and θ is the angle between the lattice plane and the incident beam (Bragg's angle) (Graff et al., 2011; Wilcox & Thron, 2016).

The size of the crystal (D) can be estimated using the diffractogram resulting from the XRD analysis by using the Debye Scherrer equation (Ingham & Toney, 2013):

$$D = \frac{K\lambda}{\beta cos\theta} \qquad (3.2)$$

`

where *K* is the shape factor (typical value of 0.9), λ is the incident beam wavelength, θ is Bragg's angle and β is the full width at half maximum peak (FWHM). The following figure (Figure 3) illustrates the working principle of XRD.

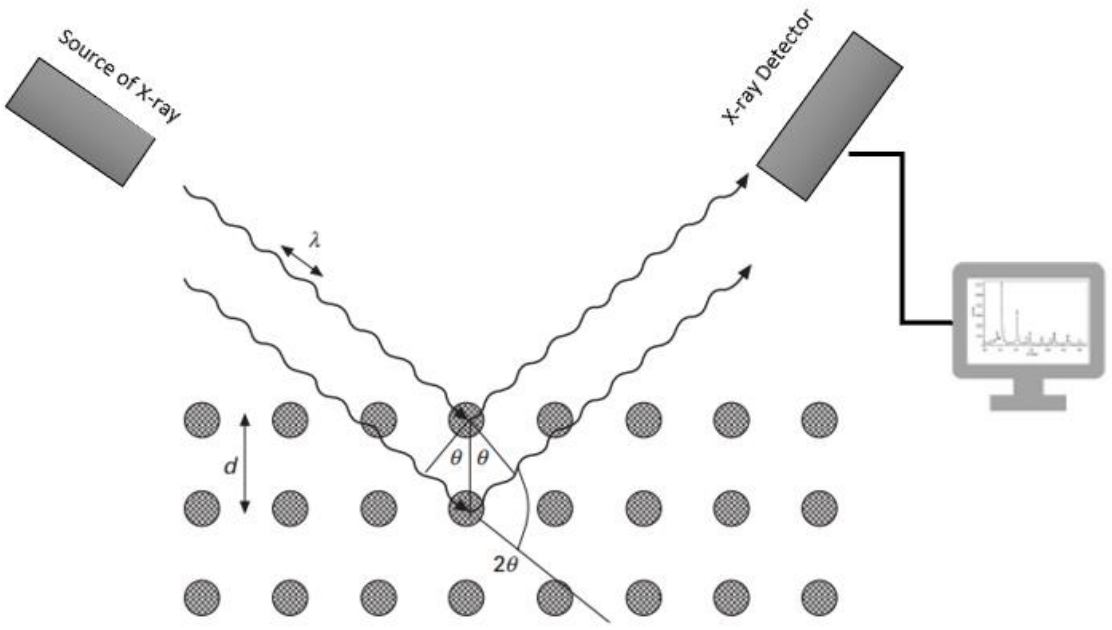

Figure 3 Illustration of XRD working principle (Ingham & Toney, 2013)

3.1.3 Fourier Transform Infrared (FTIR) Spectroscopy

FTIR spectroscopy is an analytical technique that detects the transition of vibrational energy exhibited by covalent bonds. Usually this takes place when covalent bonds absorb radiation in the infrared region (IR), and then excitation within vibrational energy levels occurs. The absorption is only possible when the electromagnetic radiation in the IR region matches the vibrational bond energy in the compound (Khan et al., 2018).

`

When energy in the IR region is absorbed, vibrational transitions (i.e., stretching, bending) take place, in which bond length can change and an atom can be subjected to an angular movement. This is usually accompanied by a change in the dipole moment of the molecule. Thus, compounds with zero net dipole moment are FTIR inactive. Strong ionic compounds (e.g. NaCl, KBr etc..) and homonuclear diatomic (e.g. H_2, N_2 etc..) molecules possess zero net dipole moment, and thus are FTIR inactive (Khan et al., 2018).

The produced IR spectrum is represented by groups of frequencies. These groups are the far-infrared region, near-infrared region, and mid-infrared region. In this study, the group of concern is the mid-infrared spectrum (4000 – 400 cm^{-1}). An infrared spectrum is generated by passing infrared radiation through a sample pelleted with KBr, and then determining the absorbed or transmitted fraction of the incident radiation at a specific energy (Pavia et al., 2000).

The FTIR device, is based on the Michelson interferometer. The interferometer is made up of the following components, movable mirror, fixed mirror, and a beam splitter. The collimator directs the infrared radiation in a single direction towards the beam splitter. Half of the incident beam is transmitted to the fixed mirror and reflected back to the beam splitter. The other half is transmitted to the movable mirror and then reflected back to the beam splitter, where the two beams are recombined and propagate towards the detector. Depending on the path length difference between the two beams, either constructive or destructive interference occurs. If the difference in path length is equal or a multiple of the wavelength, then a constructive interference occurs. If the difference in path length is a fraction of the wavelength, then destructive interference occurs. The product from the interferometer is called the interferogram, it contains all the data as signals but in the form of time domain spectrum. The Fourier transform is a mathematical treatment, which

`

transforms the amplitude signals as a function of time to amplitude power signals as a function of frequency. Figure 4 illustrates the components of the interferometer (Pavia et al., 2000).

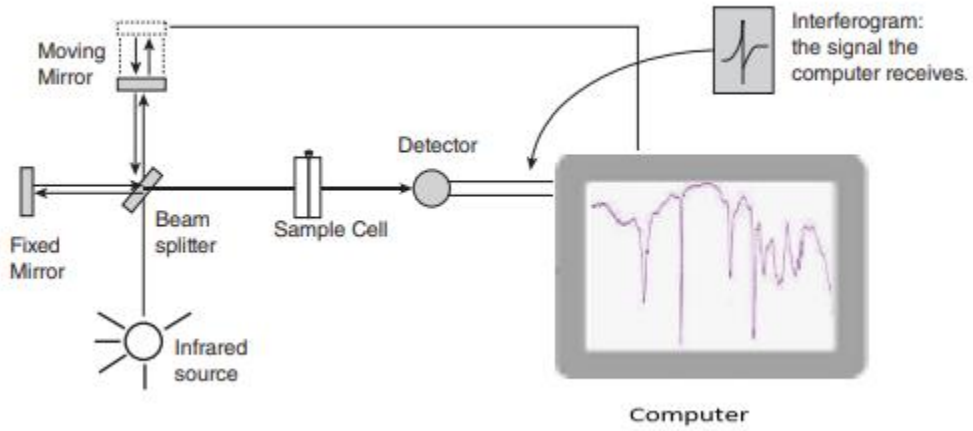

Figure 4 Fourier transform infrared spectrophotometer (Pavia et al., 2000).

3.1.4 Ultraviolet/ Visible (UV/VIS) Spectrophotometry

UV-VIS spectrophotometry is a quantitative analytical instrument. The working principle depends on the absorption of light of wavelength ranging between 200 – 800 nm. Unlike IR spectroscopy which depends on the vibrational energy level excitations, the UV-VIS spectroscopy depends on excitation of electronic energy levels, as they possess shorter wavelength (i.e., higher frequency or higher energy) (Stuart, 2004).

When energy is absorbed by a molecule, electrons are excited from an occupied orbital to an unoccupied orbital of higher potential energy, i.e., from the highest occupied molecular orbital (HOMO) to the lowest unoccupied molecular orbital (LUMO). It is always true that electronic transitions take place from σ to σ*, n to σ*, n to π*, π to π* where σ are of a single bond electron, π are double bonds electrons, and n electrons are of the lone pairs (Pavia et al., 2000). From Beer-

`

Lambert law the amount energy absorbed is proportional to the concentration of the sample in the solution. The law is given by (Pavia et al., 2000),

$$A=\varepsilon cl \tag{3.3}$$

where *A* is the absorbance of the solution, *l* is path length, *c* is the concentration of the sample and ε is molar absorptivity of the sample.

Typical UV-VIS spectrophotometer is composed of the following parts: source of light, a monochromator, beam splitter and a detector. Two types of lamps are used as sources of light, a deuterium lamp which emits electromagnetic radiation in the UV region of the spectrum and a tungsten lamp which emits rays in the visible region of the spectrum. A diffraction grating (monochromator) is used to disperse the beam of light into its constituent wavelengths. The dispersed light is focused by a system of slits and then is split into two beams, the sample beam and the reference beam. Each beam passes through its corresponding cuvette holding. The light from the cuvettes reaches the detector and its intensity is measured (A. De Caro, 2015; Gong et al., 2009; Pavia et al., 2000). Figure 5 depicts the process of measuring concentration using a UV/VIS instrument.

`

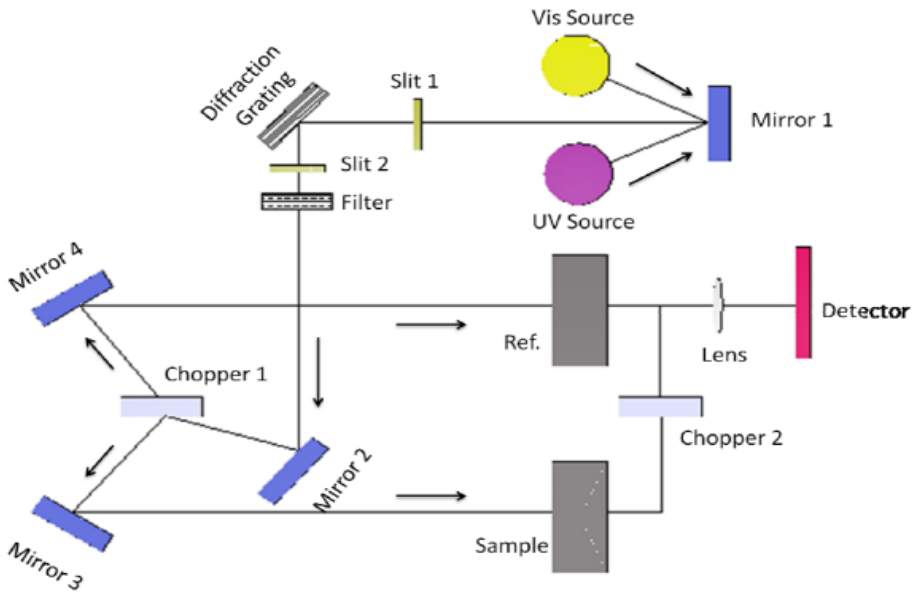

Figure 5 UV-VIS spectrophotometer schematic diagram (Gao, 2012).

3.1.5 Brunauer-Emmett-Teller (BET) Analysis

Adsorption is a surface phenomenon, in which an adsorbate is bound to an adsorbent. The adsorbent is usually a solid which exhibits a porous structure, whereas the adsorbate can be a gas, liquid, or solid. Usually, the interaction between the adsorbate and the adsorbent is spontaneous, due to the presence of unsatisfied bonds on the surfaces of both adsorbent and adsorbate, i.e., the spontaneous process takes place in order to make the energetically unfavorable surface energetically favorable. Hence, it is extremely important to analyze the structure of the adsorbent when studying adsorption processes. The main properties studied include, pore size, pore volume, surface area and pore distribution (Jürgen U. Keller, 2005).

Surface area was first assessed based on the assumption of formation of monolayer by Langmuir. However, the BET model extended the assumption to include multilayer adsorption alongside the monolayer adsorption. The BET analysis uses a gas physisorption analysis to determine the earlier mentioned properties of the adsorbent, usually, the inert gases used are

`

nitrogen or argon. The surface area is then measured by injecting an inert gas into a closed glass tube where the adsorbent is kept. The gas comes then in direct contact with the adsorbent at constant temperature until equilibrium (gas pressure) is established. Since, the cross-section of the gas molecule is known the surface area can be calculated by determining the number of gas molecules adsorbed onto the adsorbent. In addition, the pore volume is determined from condensation of gas molecules in the pores of the adsorbent (Jürgen U. Keller, 2005).

Adsorption isotherm is a relationship between the amount of adsorbate gas and the equilibrium gas pressure at constant temperature. The IUPAC classified such standard isotherms into six different types. Their classification is associated with their pore size and structure, hence, its helps in determining many features of the adsorbent easily (S. Lowel, 2004). Figure 6 depicts the six standard types of isotherms according to IUPAC.

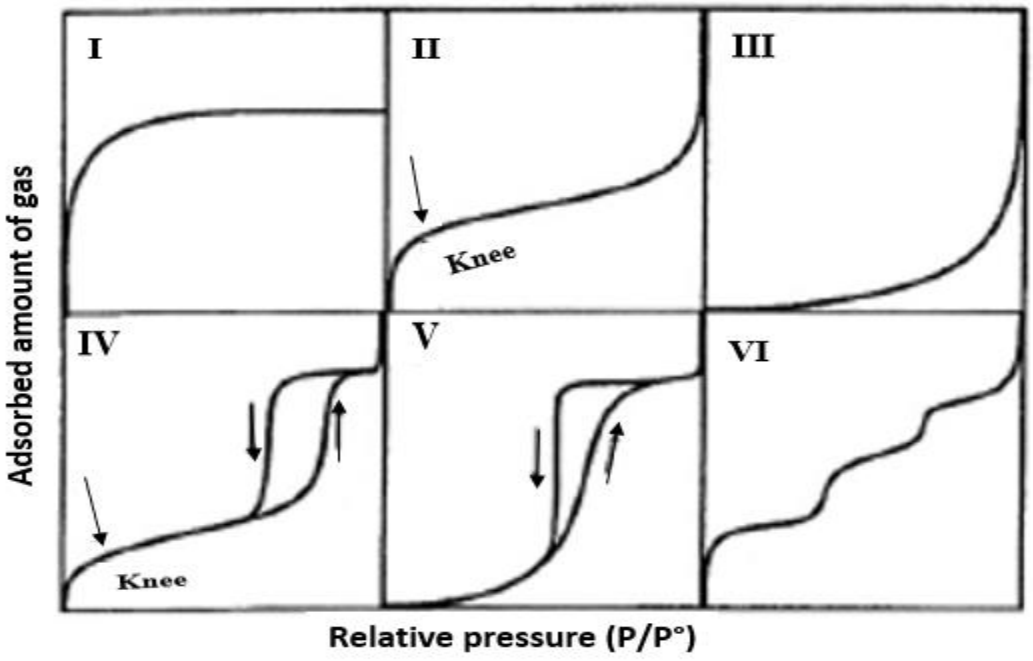

Figure 6 IUPAC Isotherms (Jürgen U. Keller, 2005).

`

These adsorption isotherms can be explained as follows:

Type I is described by Langmuir model, where the plot is concave to the P/P° axis. The pore size is microporous (< 2 nm).

Type II is exhibited by either a nonporous or macroporous (>50 nm) material. Both monolayer and multilayer adsorption takes place, where the knee at point B represents the relative pressure where complete monolayer surface coverage is completed.

Type III is hyperbolic (convex to the P/P° axis), and it is exhibited by nonporous or macroporous materials where the adsorbent-adsorbate interaction is far more less than the adsorbate-adsorbate interaction.

Type IV is exhibited by mesoporous materials (2-50 nm) with strong interaction between adsorbent and adsorbate. The existence of the knee and hysteresis loop is an indication of the presence of pore condensation.

Type V is exhibited by mesoporous materials with weak interaction between adsorbent and adsorbate, and it is highly uncommon.

Type VI is exhibited by nonporous materials, where the surface is almost completely uniform and multilayer adsorption occurs layer by layer (Shields, 1991).

3.1.6 Thermogravimetric Analysis (TGA)

Thermogravimetric analysis is the study of the thermal behavior of a substance under specified heating rate and atmosphere. The thermal stability profile of the sample is obtained by tracking the loss in weight with respect to increase in temperature. The loss in weight of the sample is attributed

`

to the thermal decomposition of the sample. The result of this analysis is displayed as a plot of weight loss % versus temperature (Brown, 1989).

The apparatus consists of an extremely sensitive balance to measure weight changes and a programmable furnace. The balance is thermally isolated and placed above the furnace. A high precision wire is suspended from the balance down into the furnace, where a ceramic cuvette is hanged (sample is placed in the ceramic cuvette during analysis) (Ebnesajjad, 2011). Figure 7 represents the working scheme of TGA.

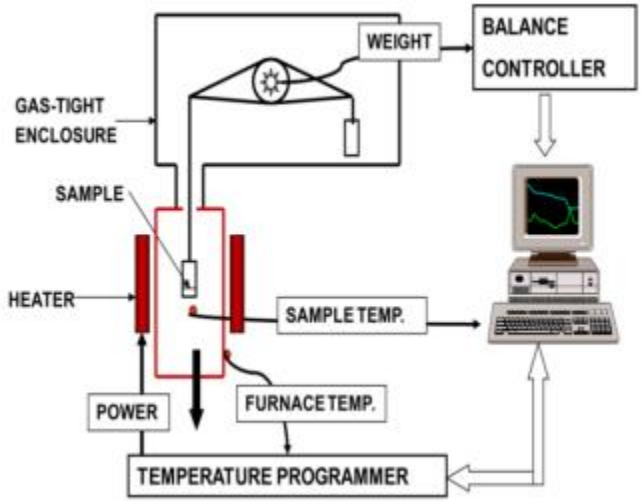

Figure 7 TGA working scheme (Raju, 2012).

3.1.7 Inductively Coupled Plasma/ Optical emission spectroscopy (ICP/OES)

Inductively coupled plasma/ optical emission spectroscopy (ICP/OES) is a spectroscopy analytical technique used to detect metal traces. Its main parts consist of plasma as the excitation source. ICPs are divided into atomic/optical emission spectroscopy (AES/OES) or atomic emission/mass spectrometry (AES/MS). The sample is transferred to the instrument as a liquid,

`

and inside the device the liquid sample is converted to aerosols via a process known as nebulization. Then, the aerosols are transported to the plasma where it is then subjected to the following consecutive processes of de-solvation, vaporization, atomization, excitation and/or ionization by the action of plasma on it. Then the excited ions or atoms emit a wavelength which is a characteristic property of the metal. The wavelength is then detected by a detector and converted to signals to be analyzed by a connected computer. Figure 8 illustrates the working scheme of ICP/OES (Fredeen, 2004).

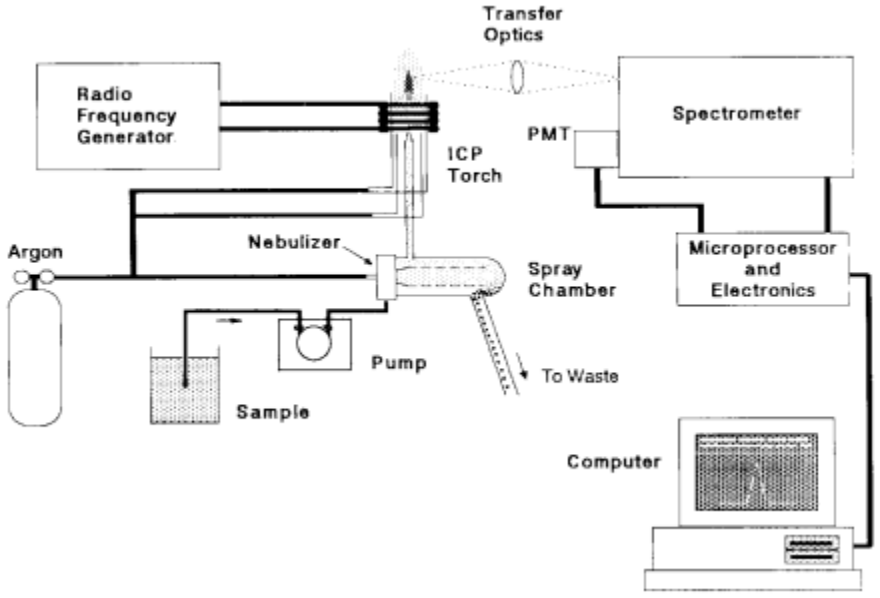

Figure 8 Working scheme of ICP/OES (Fredeen, 2004).

3.1.8 Transmission Electron Microscopy (TEM)

Transmission electron microscopy (TEM) is a quantitative technique of characterization, where it is used to determine the particle size, shape and distribution of nanomaterials. TEM is also used as a spectroscopic imaging technique similar to SEM. The difference between TEM and SEM is mainly in the action of the beam of electrons, i.e., in case of TEM the beam of electrons is transmitted through the sample while in SEM the beam is scattered from the surface. TEM is

`

advantageous over the SEM technique for having a higher resolution. A high voltage, 200 keV, of a highly focused electron beam is transmitted through the sample, thickness of the sample is typically 100-200 nm. The transmitted electrons undergo coherent scattering or diffraction from crystalline lattice planes; hence, phases can be identified. The qualitative elemental analysis can be achieved via the characteristic x-rays that are generated (Ebnesajjad, 2011; Santwana Padhi, 2022).

`

Chapter 4

`

4.Materials and methods

4.1 Materials

All chemicals purchased were of analytical grade and were used as received without any further purification. For the process of synthesis of nano-hydroxyapatite/carbon composite (HAP-C) from CKD, citric acid monohydrate (MW 210.14 g/mol, purity 99.5%) was purchased from Chem-Lab NV (Belgium) and ortho-phosphoric acid 85% was obtained from Merck Millipore (Switzerland). The CKD was collected from a local cement industry and its composition determined by XRF. For the sorption studies, the following chemicals were used; Rhodamine-b dye (pK_a=3.7, MW 479.02 g/mol) from Loba Chemie (India), sodium hydroxide (MW 40 g/mol, purity 99%) from Piochem labs and hydrochloric acid, HCl (purity 37 % by weight). Levofloxacin hemihydrate (pK_{a1}=6.8 & $pK_{a2=}$8.2, MW 740.7 g/mol, purity 98.0-102%) was obtained from Zhejiang East Asia pharmaceutical Co. (China). Commercial hydroxyapatite (MW 1004.6 g/mol) from Nano Tech Egypt for Photo-Electronics.

4.2 Methods

In this study, the adsorbent was synthesized from the industrial waste CKD, however, to do so initially calcium was separated from CKD to be used as a precursor for the synthesis of HAP-C. The separation of calcium and the subsequent HAP-C synthesis will be detailed in the forthcoming sections.

4.2.1 Precipitation of Calcium

Citric acid monohydrate was allowed to react with the raw CKD in order to chelate calcium and separate it from other components of the CKD. The following modified procedure was followed (H. Zhao et al., 2013), initially the CKD was subjected to drying and removal of any volatile matter at 105^oC ± 2^oC for 7h in an oven, i.e., until the mass was stable and no more mass fluctuations

`

were observed. Then, 200 mL of 1M citric acid were added slowly to 10 g of CKD placed in a 250 mL Erlenmeyer flask, to avoid effervescence of the evolving hydrogen gas. The solid to liquid ratio (1:20 w/v) was adopted specifically to avoid formation of sludge at the end of the reaction (Seo et al., 2019). The reaction was conducted at room temperature (25°C±2) for 10 min on a magnetic stirrer with vigorous mixing. The produced calcium rich solution (H. Zhao et al., 2013), was collected using a vacuum filter to get rid of any unreacted CKD, then the solution was heated for 1h at 105°C±2. The resultant precipitate was a white calcium chelate, which was further subjected to vacuum filtration and up to five times washing with distilled water. After filtration and washing, the white precipitate was dried in an oven for 2h at 100^{o}C ± 2. Figure 9 illustrates the whole process of separating calcium from CKD.

Citric acid is a triprotic acid, and its chemical reaction with CKD proceeds as follows.

$$\mathbf{m\ M^{x+} + \mathit{l}\ L^{y-} + h\ H^{+} \longleftrightarrow mM^{x+}\mathit{l}L^{y-}hH^{+}} \quad (4.1)$$

where M is calcium metal, L is the citrate ligand and H^{+} is the hydrogen ion lost from the carboxylic acid functional group (H. Zhao et al., 2013). The type of calcium chelate formed is determined by the number of hydrogen ions lost, i.e., there are 3 different possibilities of chelates that can be formed. Table 4 illustrates the types of chelates formed and their corresponding stability constants. From the stability constants, one can deduce that the most probable type of chelate formed is mono calcium chelate.

`

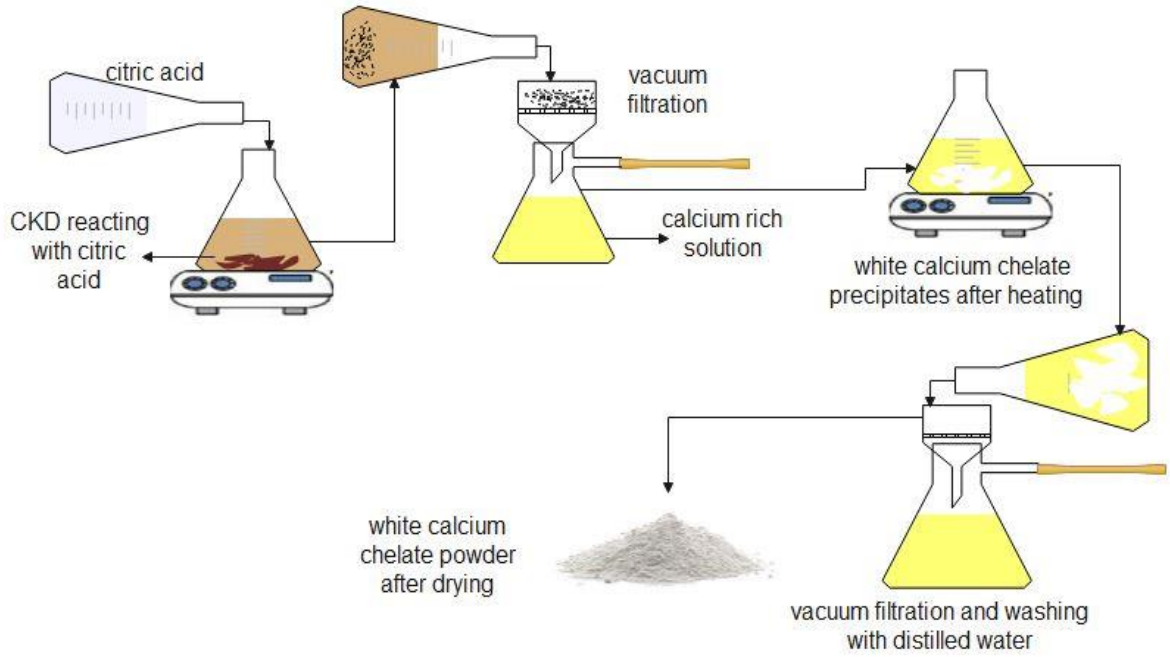

Figure 9 Precipitation of calcium from CKD.

Table 4 Calcium chelates and their respective stability constants (H. Zhao et al., 2013)

Type of calcium chelate	**Number of Hydrogen ions lost**	**Chelate stability constant (log K)**
$CaLH_2$	One	12.3
CaLH	Two	9.5
CaL	Three	4.7

The difference between the procedure adopted in our study and the one in literature, is the method of precipitation of calcium. As mentioned earlier, heating was used here while in the previously reported procedure the calcium rich solution was reacted with potassium carbonate (H. Zhao et al., 2013). In addition, the acid concentration as well as the solid to liquid ratio were

`

modified. The main advantage of the modification of the procedure was the purity of the eluate. The method was primarily used for dissolution of wollastonite which is composed of calcium and silicates, whereas in our case it was used to elute calcium from CKD, and hence the use of K_2CO_3 was not adopted, as in previous literature, since it could result in precipitation of metal carbonates other than calcium.

4.2.2 Synthesis of HAP-C nanocomposite

The synthesis method used for producing HAP-C nanocomposite was adopted from previous literature (Pham Minh et al., 2013). However, the latter method was used to produce pure hydroxyapatite (HAP), whereas in this study it was used to produce the nanocomposite HAP-C. In this method, calcium chelates underwent a thermal decomposition at 450^{o}C for 1h in a muffle furnace (VULCAN 3-550). The calcium carbonate was then used as a precursor for the synthesis of the HAP, in addition, the presence of the carbon was exploited to synthesize the nanocomposite adsorbent, i.e., the HAP-C. Calcium carbonate and ortho-phosphoric acid were reacted in stoichiometric ratios to obtain a 1.67 Ca/P ratio. The reaction took place for 24 h at 80^{o}C ± 5^{o}C on a magnetic stirrer with vigorous stirring. The acid was added to the solution of calcium carbonate dropwise (~ 1.5 mL/min). The resultant product was separated from the supernatant by vacuum filtration and washed with distilled water 5 to 6 times, followed by air drying for 12h. Figure 10 illustrates the process of synthesis of HAP-C nanocomposite.

`

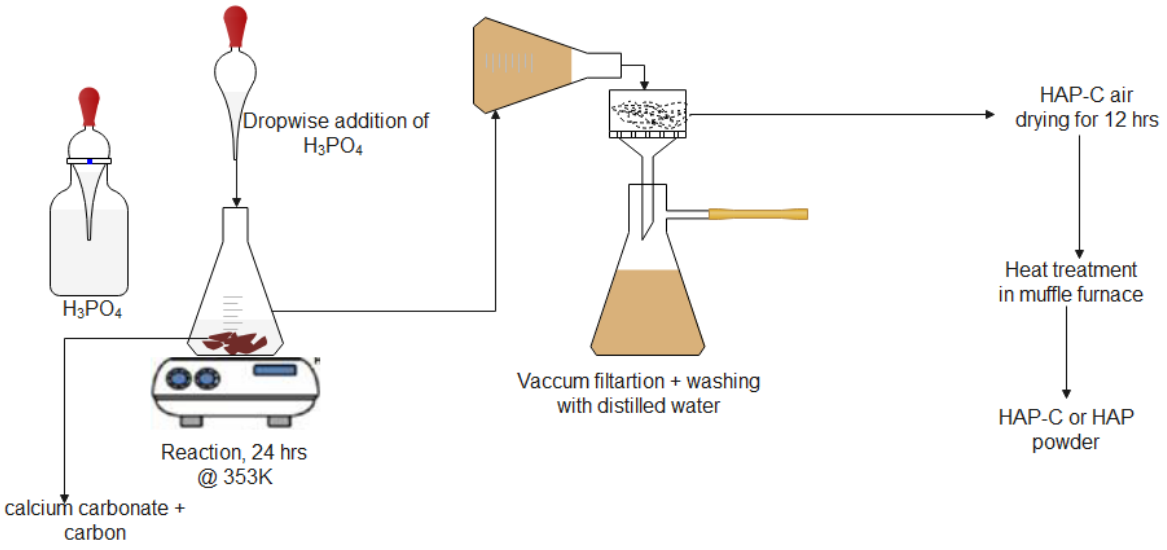

Figure 100 Synthesis of HAP-C and HAP.

The synthesized HAP-C was subjected to various thermal heating scenarios to assess the effect of heat on its properties and performance. The following table summarizes the heating conditions that the HAP-C was subjected to. Under certain treatments, the HAP-C converts to HAP (HAP 700, and HAP 900).

Table 5 Heat treatment conditions for the synthesized adsorbent

Adsorbent Name	Atmosphere	Temperature, °C
HAP-C	-	-
HAP-C 400	Inert	400
HAP-C 500	Inert	500
HAP-C 700A	Inert	700
HAP 700	Air	700
HAP 900	Air	900

`

4.3 Characterization

4.3.1 X-ray Fluorescence (XRF)

The CKD sample powder was mixed with a binder material (cellulose wax) in a ratio of 20% to 80% by wt. Then, the mixture was ground and pressed at a pressure of 4kPa, leading to formation of a pellet. The pellet was heated to 1000°C leading to loss of all volatile matter, then, the sample was subjected to an X-ray beam to detect the oxides of the elements present in the CKD.

4.3.2 Fourier Transform Infrared (FTIR) analysis

Infrared spectroscopic analysis was carried out using a Thermo-Scientific NICOLET 380 FTIR device. The samples were prepared first in the form of pellets, this was done by mixing and grinding the synthesized HAP and HAP-C nanocomposites with analytical grade KBr in a ratio of 1:100 (by wt). Then, the mixture was subjected to a hydraulic press at 1,400 kPa for 2 min. The samples were then scanned from 4000 to 400 cm^{-1} wavenumbers at an average recording of 32 scans. To prevent the interference of the surrounding with the spectra of the samples, the background was first scanned and subtracted from that of the sample.

4.3.3 Powder X-ray Diffraction (XRD)

The crystalline nature of HAP and HAP-C was examined using powder x-ray diffractometer BRUKER D8 system. The two-theta (2θ) range of the scan was from 5^o to 80^o at a scan increment rate of 0.03^o per second.

4.3.4 Surface area and porosity measurements

Surface area, average pore diameter and average pore volume of HAP and HAP-C nanocomposites synthesized with various heat treatment conditions were calculated using Micrometrics ASAP 2020 instrument. To conduct the analysis, about 1g of the powder sample was placed in the designated tube of the instrument, then the tube was connected into the system and

`

degassed under 50 μmHg at 105ºC for 4 h. Nitrogen gas was used to generate adsorption/desorption isotherms at -196º C, then, the specific surface area was calculated by Brunauer-Emmett-Teller (BET) and Langmuir methods, while the pore volume was estimated based on Barret-Joyner-Halenda (BJH) model.

4.3.4 Transmission Electron Microscopy (TEM)

The size and morphology of the synthesized HAP-C nanocomposites were investigated using a high-resolution transmission electron microscope (HR-TEM, JOEL JEM-2100). The samples were first dispersed in distilled water and sonicated for 5 min, then vacuum filtered and dried. Afterward, they were subjected to a beam of electrons with a voltage of 200 kV. Morphologies, average sizes, and lattice places were determined.

4.3.5 Thermogravimetric Analysis (TGA)

The thermal stability of the synthesized HAP and HAP-C nanocomposites was investigated by means of a LABTRON thermal analyzer. A 20 mg sample powder was placed in a ceramic cuvette and subjected to 1000ºC at an incremental rate of heating of 10˚C per min. Hence, the thermal profiles of the adsorbents were generated.

4.3.6 Inductively Coupled Plasma (ICP)

Thermo Scientific ICP-AES 7000 was employed to determine the concentrations of calcium ions leached from CKD. The following formula was used to calculate the percent extraction of Ca^{2+}

$$\% \, Extraction = [(C_{ion} * V) / M_{CKD} * X_{ion\ CKD}] * 100 \qquad (4.2)$$

`

where C_{ion} is the concentration of calcium as quantified by ICP in mg/L, V is the volume of the solution, M_{CKD} is the mass of the CKD sample, and X_{ionCKD} is the fraction of calcium ion present in the CKD.

4.3.7 Zeta Potential

The surface charge was determined by a zeta-sizer (Malvern Zeta-sizer, Nano ZS). To conduct the measurement of zeta potential the following procedure was followed. To 50 mL of distilled water, 10 mg of the adsorbent was added and then sonicated for 10 min. Afterward, the mixture was divided into 5 beakers at a volume of 10 mL each, and their pH was adjusted by addition of either HCl or NaOH dilute solutions. Then, a certain amount of the pH adjusted mixture was transferred to a Malvern cuvette and measured by the zeta-sizer.

4.4 Batch Sorption experiments

To study the effect of the different operating parameters (time, initial concentration, pH and adsorbent dose) on adsorption, stock solutions of LV and RB were prepared separately in volumetric flasks by dissolving 100 mg of each contaminant in 100 mL of distilled water. Serial dilutions of 10,15, 25, 40, 50, 60 and 100 mg/L were then prepared. The pH of the solutions was adjusted by adding either 0.01 M HCl or 0.01 M NaOH accordingly. To conduct batch sorption, a known dose of the adsorbent was added to the prepared solution in a 15-mL falcon tube and subjected to shaking in a mechanical rotary mixer (80 rpm, LABDex) for a specific duration of time. Then, the solutions were centrifuged at 12,000 rpm for 5 min in a centrifuge (SIGMA 3-30KS). Each adsorption run was centrifuged twice because the adsorbents were not separated from the first centrifugation. After centrifugation, the supernatants were collected and the absorbance of either LV or RB was measured by UV/VIS spectrometer (PG instruments T80+ UV/VIS spectrophotometer) at a wavelength of 288 nm and 554 nm, respectively. The concentrations of

`

contaminants remaining in the solution after adsorption (C_e) were calculated based on pre-prepared calibration curve.

The equilibrium adsorption capacity (q_e) was calculated via the following equation,

$$q_e = \frac{(C_o - C_e)}{m} \times V \qquad (4.3)$$

where,

C_o= initial concentration of pollutants (mg/L)

C_e = equilibrium concentration of pollutants in solution (mg/L)

m= mass of adsorbent (g), and

V = volume of the solution (L).

While the percent removal of these pollutants was calculated by the following equation,

$$\%\, removal = \frac{C_o - C_e}{C_o} \times 100 \qquad (4.4)$$

where,

C_o = initial concentration of pollutants (mg/L)

C_e = concentration of pollutants at equilibrium (mg/L)

To study the thermodynamics of the adsorption process, an incubator shaker unit (New Brunswick innova 42) was employed. The adsorption process was conducted at different temperatures and then the concentration was measured using the previously mentioned procedures.

`

4.4.1 Adsorption Isotherms

An adsorption isotherm is a plot that expresses the relationship between q_e and C_e at constant temperature. These plots were fitted to several mathematical models (Langmuir, Freundlich, Sips and D-R) to predict the adsorption behavior and elucidate the nature of interaction between the adsorbent and adsorbate.

Langmuir isotherm model assumes that the surface of the adsorbent is homogenous (i.e., all sites are energetically equivalent), only monolayer adsorption takes place, and no adsorbate-adsorbate interaction exists. It also assumes that the heat of adsorption is independent on coverage of surface and is equivalent for all sites (Robert J. et al., 2022). The Langmuir model can be plotted using the following linearized equation

$$\frac{C_e}{q_e} = \frac{1}{q_m K_L} + \frac{C_e}{q_m} \qquad (4.5)$$

where,

q_m = the maximum adsorption capacity (mg/g)

K_L = Langmuir constant (L/mg)

Furthermore, the separation factor (R_L) can be calculated using equation (4.6) to determine the how favorable is the adsorption process.

$$R_L = \frac{1}{1+K_L C_o} \qquad (4.6)$$

Freundlich isotherm model unlike Langmuir isotherm model accounts for heterogeneity of the surface, and interaction between adsorbed species, i.e., accounts for multilayer adsorption. The empirical linear form of Freundlich isotherm model is given by (Popoola, 2019).

`

$$logq_e = logK_f + \frac{1}{n} logc_e \quad (4.7)$$

where,

K_f = Freundlich constant, and

n = measure of favorability of adsorption

Sips isotherm model represents a combination of Langmuir and Freundlich models. The purpose of this model is to predict the adsorption in heterogeneous system for a wider range of concentrations and so it overcomes the concentration limitation associated with the Freundlich model. The model approaches Freundlich model at low adsorbate concentrations, while at higher adsorbate concentrations it approaches Langmuir model (Popoola, 2019; Tzabar & ter Brake, 2016). The following equation is the linearized form of Sips equation

$$ln\left(\frac{q_e}{q_m - q_e}\right) = \left(\frac{1}{n}\right) lnC_e + lnK_s \quad (4.8)$$

where,

K_s= Sips constant

1/n= heterogeneity factor

The D–R isotherm model associates the adsorption process to micropore filling unlike the previous models, which are based on layer-by-layer adsorption (Hu & Zhang, 2019). It is expressed linearly by the following equation

$$lnq_e = -\beta\epsilon^2 + lnq_m \quad (4.9)$$

where, β is the D-R isotherm constant and ϵ is given by

`

$$\epsilon = RTln(1 + \frac{1}{C_e}) \quad (4.10)$$

where *R* is the universal gas constant and *T* is the absolute temperature. The D-R isotherm model is applied here mainly to estimate the energy of adsorption through the mean free energy, which is given by the following equation,

$$E = \frac{1}{\sqrt{2B_{DR}}} \quad (4.11)$$

where B_{DR} is the D-R isotherm constant.

4.4.2 Kinetic models

Two different kinetic models were investigated with respect to the adsorption of the contaminants on the synthesized HAP-C adsorbent. These are the pseudo-first order and pseudo-second order kinetic models. The first model assumes that the rate of reaction is directly proportional to the number of unoccupied sites, and is given by (Edet & Ifelebuegu, 2020),

$$\frac{dq}{dt} = k(q_e - q) \quad (4.12)$$

which is linearized to,

$$ln(q_e - q) = lnq_e - kt \quad (4.13)$$

where,

q= adsorption capacity (mg/g) at time *t*, and

k= rate constant (min^{-1})

`

The pseudo-second order kinetic model is based on the assumption that the rate of reaction is directly proportional to the square of the number of unbound sites on the adsorbent surface (Lopez et al., 2020).

$$\frac{dq}{dt} = k_2(q_e - q)^2 \quad (4.14)$$

Integrating the above equation results in the following linear form

$$\frac{t}{q} = \frac{1}{{q_e}^2\, k_2} + \frac{t}{q_e} \quad (4.15)$$

4.4.3 Thermodynamic Study

To estimate thermodynamic parameters of the adsorption process, the van't Hoff equation (Eq. 4.16) was used (Ebelegi et al., 2020).

$$lnK_e = -\frac{\Delta H}{RT} + \frac{\Delta S}{R} \quad (4.16)$$

Where K_e (q_e/C_e) is the equilibrium constant, ΔS is the entropy (KJ/mol), and ΔH is the enthalpy (KJ/mol).

The Gibbs free energy (ΔG) can then be calculated using Eq. 4.17,

$$\Delta G = -RTlnK_e \quad (4.17)$$

The Gibbs free energy is an indication of the spontaneity of the adsorption process, while ΔH determines whether the adsorption process is exothermic or endothermic, and ΔS indicates the favorability of the adsorption process (for $\Delta S<0$ indicates decrease in randomness and hence favorability of adsorption process).

`

4.4.3 Statistical Analysis

All the sorption experiments were run in triplicates and the values of the adsorption capacity and removal were expressed as mean ±SD (standard deviation). To test the significance of results a two-tailed student's t-test at a 95% level of confidence was conducted. The adsorption isotherms and kinetic models' fitness (linear regression) were confirmed by using coefficient of determination (R^2) and Chi-square test ($\chi 2$). The linear regression analysis was conducted via the use of Origin-lab software, version 85E.

`

Chapter 5

`

5. Results and Discussion

The purpose of this study is to produce HAP-C from the industrial waste CKD. Hence, it was important first to study the process of chelating calcium from the CKD then using the calcium chelate in HAP-C preparation. The following sections will discuss the synthesis, characterization, and adsorption performance of the synthesized adsorbent.

5.1 Chelating Calcium from CKD and Synthesis of HAP-C composite

An XRF analysis was conducted for the CKD to determine its mass composition as given by Table 6. CKD constitutes mainly CaO, along with minor amounts of other oxides.

Table 6 XRF analysis of CKD

Constituents	**SiO_2**	**TiO_2**	**Al_2O_3**	**Fe_2O_3**	**CaO**	**K_2O**	**Na_2O**	**P_2O_5**	**SO_3**	**Cl**	***L.O. I**
Mass %	**6.55**	**0.23**	**2.12**	**2.06**	**37.81**	**2.78**	**0.96**	**0.08**	**1.1**	**4.23**	**40.54**

*L.O. I: Loss on ignition

The mass % of CaO in CKD varies depending on the raw material used in the process of producing cement. Various studies have reported mass % exceeding 60% for CaO in CKD (Seo et al., 2019; Siddique, 2014). Since the CKD mainly consists of CaO, it was exploited for synthesizing the adsorbent. Therefore, citric acid was used to separate calcium from CKD because of its ability to readily form a complex with calcium via chelation (Kirimura & Yoshioka, 2019). The effect of pH and citric acid concentration on the percent extraction of calcium ions was studied and is summarized in Table 7. After inspecting the results in Table 7, a concentration of 1 M of citric acid (with no pH adjustment) was used to obtain Ca^{2+} ion, to avoid contamination with pH adjusting reagents.

`

Table 7 Effect of Citric acid concentration and solution pH on Ca^{2+} extraction

Concentration (M)	pH	% Extraction of Ca^{2+}
0.5	3.7*	91
0.5	5	73.3
1	3*	73.1
1	5	99.9
2	2.6*	29.5
2	5	99.9

*No pH adjustment was made after reaction.

The calcium chelate complex was then subjected to 1h heating at 450 °C to produce calcium carbonate in addition to carbon. To investigate the chelate, prior to heat treatment, a TGA analysis was conducted, where the temperature was raised up to 700°C. Figure 11 represents the TGA analysis for the thermal decomposition of the calcium chelate.

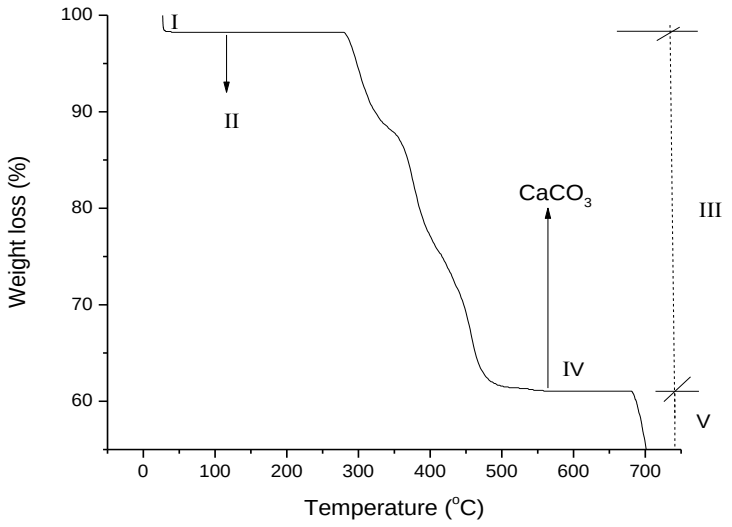

Figure 11 Thermogravimetric analysis of calcium chelate.

`

Process I represent the loss of surface adsorbed water molecules, which accounts for 1.6% of the weight lost. In Process II, no loss in weight takes place owing to possible melting of the chelate (J. Li et al., 2016). Process III represents the decomposition of the chelate into calcium carbonate, and it is associated with the loss of carbon as CO_2 accounting for 39% loss. This process is completed at 560°C, where after no weight loss was observed. This process can be represented by the following chemical equation (unbalanced).

$$Ca_x^{2+}\ L_y^{3-}\ H_{z-x}^{+} \longrightarrow xCaCO_3 + z\text{-}xH_2O + CO_2 \qquad (5.1)$$

Process IV represents the pure calcium carbonate heating where no loss of weight was noticed. Process V begins at 681°C, where the calcium carbonate starts to decompose to calcium oxide and CO_2.

After heat treatment at 450°C for 1h, TGA and XRD tests were conducted for the chelate. Figure 12 illustrates the TGA analysis of the chelate after heat treatment which is composed of calcium carbonate along with some carbon produced as a result of heat treatment. The amount of carbon was estimated by subtracting the weight loss at 450°C from the weight loss at 560°C, at which only calcium carbonate starts to exist (estimated to be 6-7 %).

`

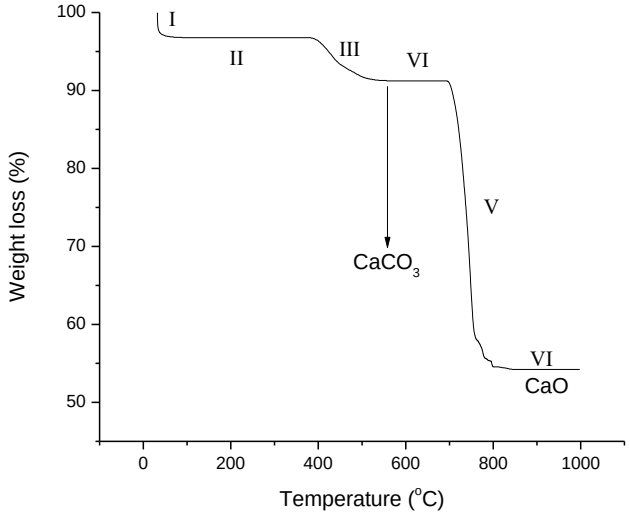

Figure 12 TGA analysis of calcium chelate after heat treatment.

The TGA analysis after heat treatment of the chelate is identical to the one before the heat treatment, except for the amount of weight loss. In process III the decomposition starts at temperature above 400°C, because this sample was already subjected to heat treatment. In process VI, the decomposition of $CaCO_3$ to CaO was almost complete and the weight loss was approximately 40%, which is close to the theoretical loss i.e., 44 %. XRD analysis was also conducted to confirm the product after heat treatment.

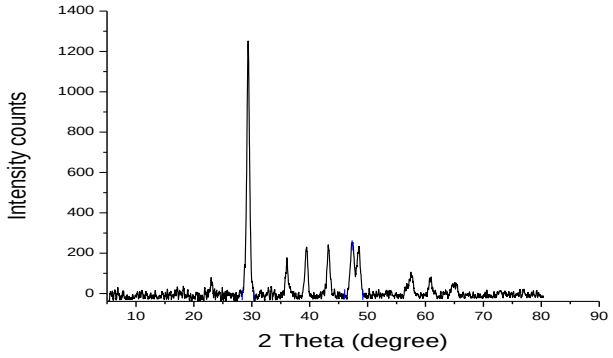

Figure 13 XRD pattern of thermally treated calcium chelate (calcium carbonate and carbon).

`

Intentionally, carbon was not separated from the mixture in order to eventually form the nanocomposite of carbon with HAP. XRD analysis was conducted confirmed the formation of $CaCO_3$ product (Figure 13). Calcium carbonate appeared as brownish black after heat treatment, possibly since it was coated by carbon.

The presence of carbon with calcium carbonate was then exploited to synthesize the adsorbent. A free activation protocol (activation of carbon without use of chemical reagents) was adopted from previous literature to enhance the adsorption capacity of the nanocomposite adsorbent through increasing the porosity and activating the hydroxyl groups (Gursharan et al., 2022; Qing et al., 2012). According to the study reported by Qing et al. the surface area of the composite was expected to exceed the 700 m^2/g (Qing et al., 2012), however, this was not achieved due to the increase of crystallinity of hydroxyapatite as it was heated which led to the decrease in surface area (Ivanets et al., 2019; Rout et al., 2020). Meanwhile, using the activation free protocol at higher temperatures proved to enhance the composite adsorbent performance in removing pollutants. Table 8 summarizes the effect of temperature on the performance of the adsorbent.

Table 8 Effect of heat treatment on the performance of synthesized adsorbent

Adsorbent	**RB removal (%)**	**LV removal (%)**
HAP-C	39.06	45.87
HAP-C 400	43.83	39.24
HAP-C 500	61.21	37.13
HAP-C 700A	96.61	76.48

* The heat treatment conditions were adopted from (Qing et al., 2012).

As can be deduced from Table 8, the adsorbent HAP-C 700A showed the highest removal efficiency, and thus, was used throughout the adsorption study.

`

5.2 Characterization

5.2.1 FTIR spectroscopy

FTIR spectroscopy was used as a confirmatory test for the synthesized adsorbent. The main functional groups present in the adsorbents synthesized under various heat treatment conditions were also determined. Figure 14 illustrates the FTIR spectra of the different synthesized nanocomposites. In addition to the adsorbents synthesized, the FTIR spectra of commercial HAP (com-HAP) is also depicted in Figure 14 for comparison.

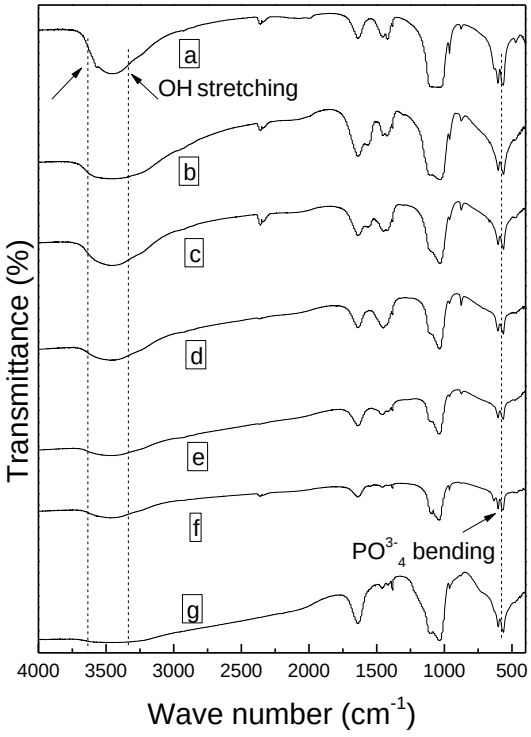

Figure 14 FTIR for a) com-HAP, b) HAP-C, c) HAP-C 400, d) HAP-C 500, e) HAP-C 700 A, f) HAP 700, and g) HAP 900

It is clear that all synthesized HAP-C nanocomposites and the commercial HAP show a broad band at 3700-3200 cm^{-1} which corresponds to the stretching vibration of hydrogen bonded group.

`

In addition, peaks appearing at 563, 960, and 1030 cm^{-1} can be ascribed to the stretching vibration of PO^{3-}_4. The bending vibration of PO_4^{3-} bonds is represented by the peaks 605, 871 and 2360 cm^{-1}, however, the latter can only be observed in com-HAP, HAP 700, HAP-C, and HAP-C 400 (Jayaweera et al., 2018). Peaks at 1458 and 1380 cm^{-1} can be attributed to the bending of the OH group (Shavandi, Bekhit, Ali, et al., 2015).

5.2.2 XRD Analysis

XRD powder analysis was also used as a confirmatory test. The main peaks confirming the crystalline structure of HAP and HAP-C can be seen in Figure 15 at 26°, 29°, 32°, 34°, 40°, 46° and 54°. These peaks are in agreement with previous literature (Mujahid et al., 2015; Rout et al., 2020; Santos et al., 2004; Shavandi, Bekhit, Ali, et al., 2015). It is also worth noting that some peaks of the pure HAP XRD pattern are altered in case of nanocomposites that contain amorphous carbon. The noise in the diffractogram can be attributed to the presence of amorphous carbon, which is eliminated in case of HAP. The crystal size was estimated using Debye–Scherer equation and pure HAP (HAP 700 and HAP 900) showed the largest crystal size among the different nanocomposites, which could explain the low surface area obtained for the nanocomposites using BET analysis (Ivanets et al., 2019). However, the crystal sizes of the rest of the nanocomposites showed little variation, even though, their surface areas differed noticeably. Table 9 illustrates the crystal sizes as estimated by Debye Scherrer equation, along with the corresponding surface areas as measured by BET.

`

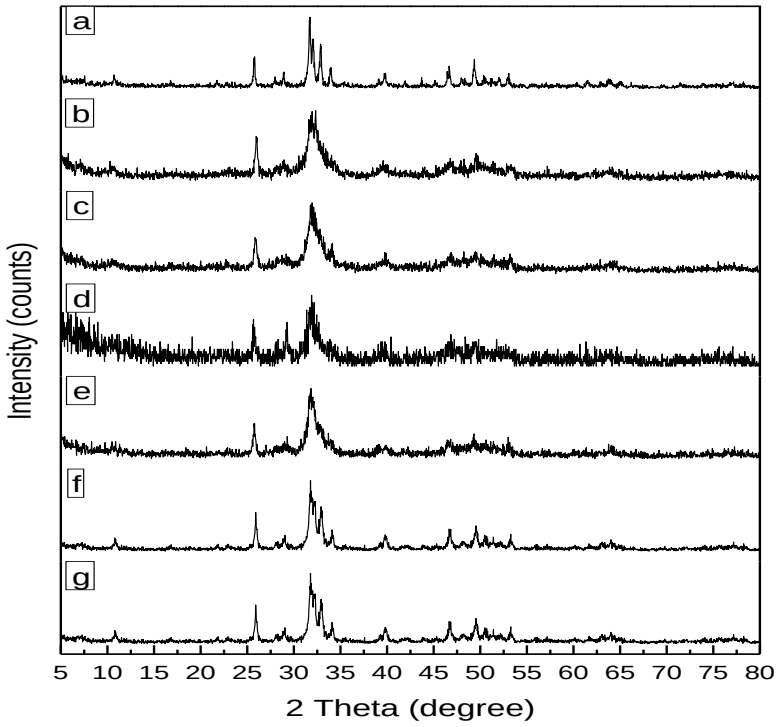

Figure 15 XRD patterns for a) com-HAP, b) HAP-C, c) HAP- 400, d) HAP-C 500, e) HAP-C 700 A, f) HAP 700, and g) HAP 900

Table 9 Crystal sizes and BET surface areas of the synthesized adsorbents

Adsorbent	**Crystal size (nm)**	**BET Surface area (m^2/g)**
HAP-C	4.54	147.00
HAP-C 400	4.57	136.65
HAP-C 500	5.70	119.98
HAP-C 700A	5.93	107.96
HAP 700	6.45	30.69
HAP 900	13.3	18.98

`

5.2.3 Textural and Structural Properties

The surface area and pore size play a crucial role in adsorption, hence, BET analysis was conducted to determine these surface properties. The nitrogen adsorption-desorption isotherms for all HAP and HAP-C adsorbents (Figure 16 and 17, respectively) revealed a type IV isotherm, where the adsorbent-adsorbate interaction is much less than the adsorbate-adsorbate interaction. Type IV isotherm is associated with mesoporous pore sizes that range between 2-50 nm.

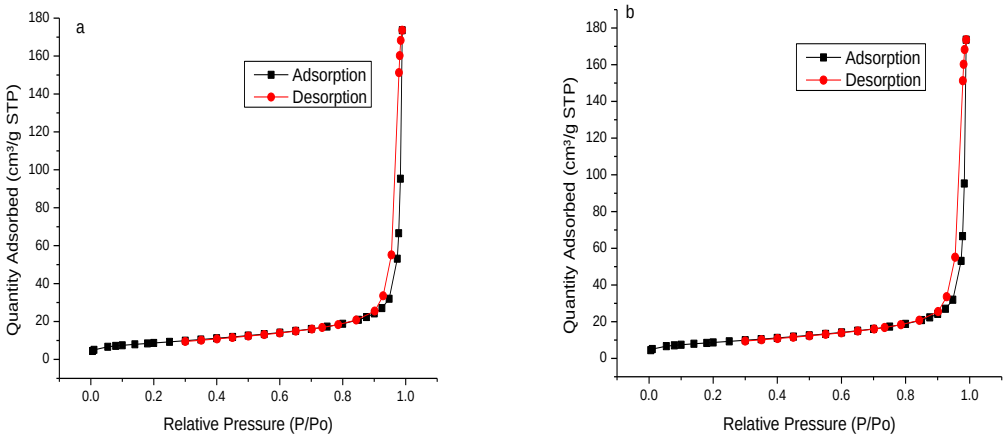

Figure 16 Adsorption-desorption isotherms for a) HAP 900, and b) HAP 700.

`

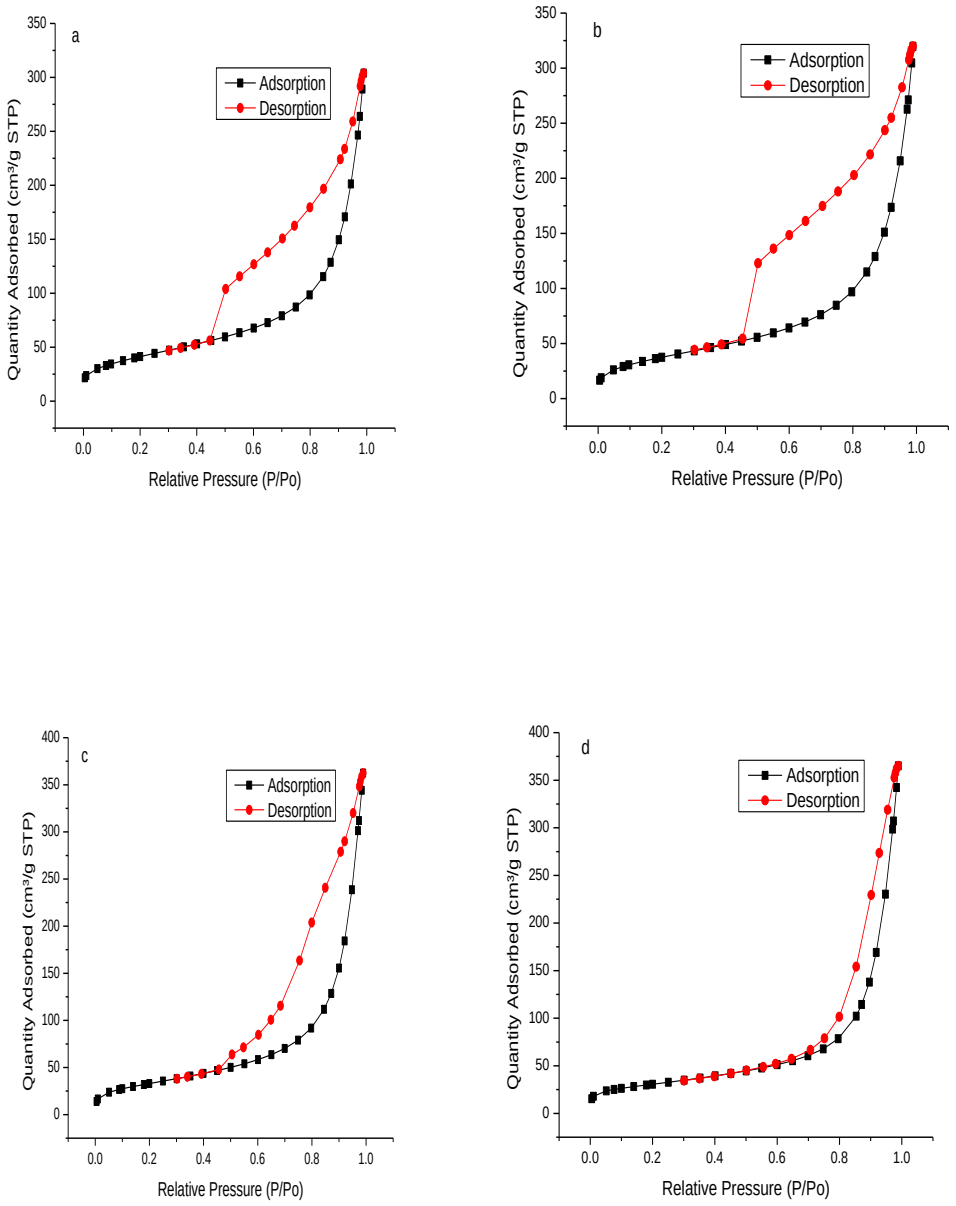

Figure 17 Adsorption-desorption isotherms for a) HAP-C, b) HAP-C 400, c) HAP-C 500, and d) HAP-C 700 A

Table 10 summarizes the textural properties of the synthesized adsorbents and confirms that the average pore sizes of all adsorbents are in the mesoporous range. The shape of the hysteresis loop

`

also indicates the geometry of the pores, which can be estimated to be cylindrical for HAP-C and HAP-C 400, while those of HAP-C 700 A and HAP-C 500 almost agree with the wedge-shaped pore geometry (S. Lowell et al., 2004; Xu et al., 2020).

Table 10 Surface properties of synthesized adsorbents with various heat treatment conditions

Adsorbent	**BET S.A (m^2/g)**	**Langmuir S.A (m^2/g)**	**Pore width (nm)**	**BJH Pore volume (cm^3/g)**
HAP-C	147.5	214.9	12.1	0.48
HAP-C 400	136.6	200.7	13.8	0.49
HAP-C 500	119.9	176.0	17.7	0.56
HAP-C 700A	107.9	154.3	19.6	0.57
HAP 700	30.7	44.1	19.2	0.27
HAP 900	18.9	27.5	17.8	0.13

As clear from Table 10, the BET and Langmuir surface areas show an inversely proportional relationship with the temperature for all adsorbents, and almost a directly proportional relationship with the pore volume and pore width for the nanocomposites only. The case for HAP 700 and HAP 900 is different, i.e., the pore width and pore volume decreased as temperature increased. This behavior can justify the poor adsorption performance of HAP 700 and HAP 900 since they possess the smallest surface areas and pore volumes amongst the synthesized adsorbents. The surface area diminishes with increasing heat treatment temperature due to the increase in the crystal size of the HAP (Table 9), in both pure and composite forms (Ivanets et al., 2019). The pore width also plays a crucial role in the adsorption process. As presented in Table 10, the highest pore width was recorded for HAP-C 700 A, which showed the best removal efficiency for both contaminants.

`

The morphological properties of the adsorbents were further studied using a high-resolution transmission electron microscope. The images produced (Figure 18) revealed rod structured particles typical of nanohydroxyapatite (Mostafa et al., 2015). The images show nano rods coated by carbon. The coating is not shell and core model of coating, but rather HAP nanorods are embedded in the body of the carbon. The mean sizes for the diameter and length are 10± 3.6 nm and 8± 2.9 nm for HAP-C 700A, and 81± 28.9 nm and 72± 18.5 nm for HAP-C 400, respectively. The particle size distribution is shown in Figure 19. The sizes increased with increase of temperature; this could be attributed to mild sintering.

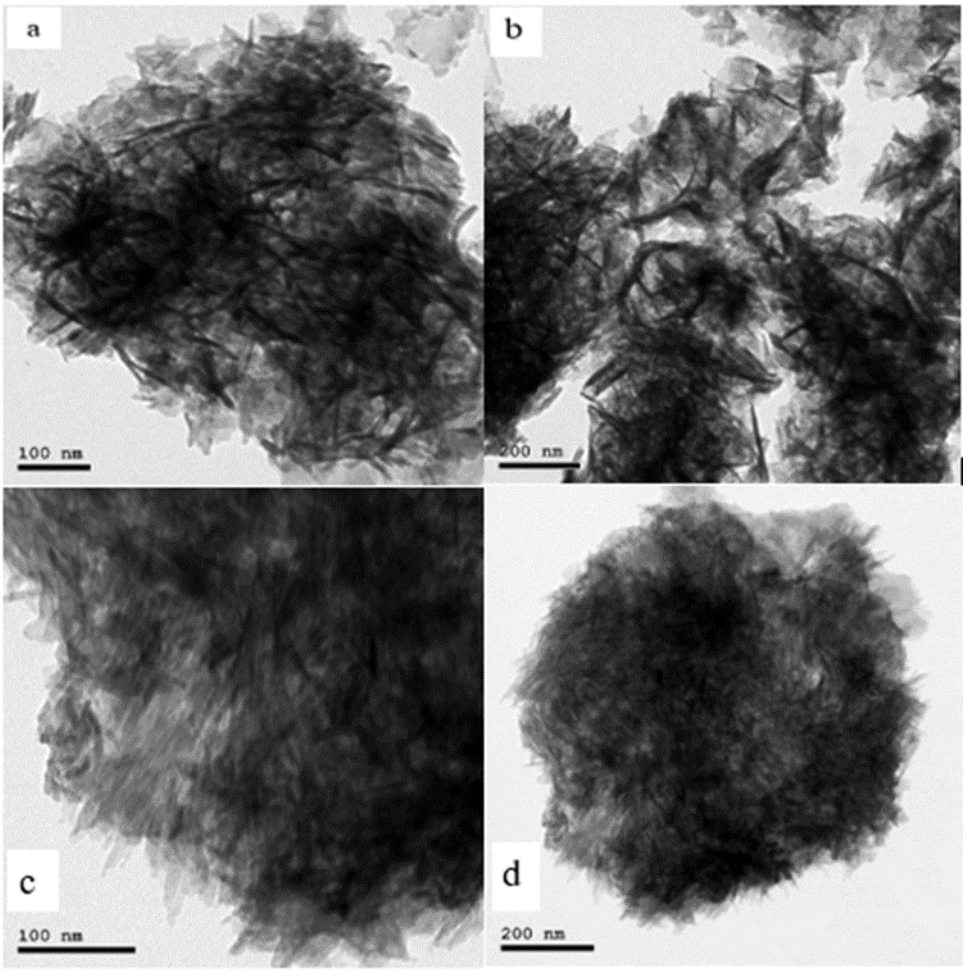

Figure 18 HR-TEM images for HAP-C 700A (a & b), and HAP-C 400 (c & d)

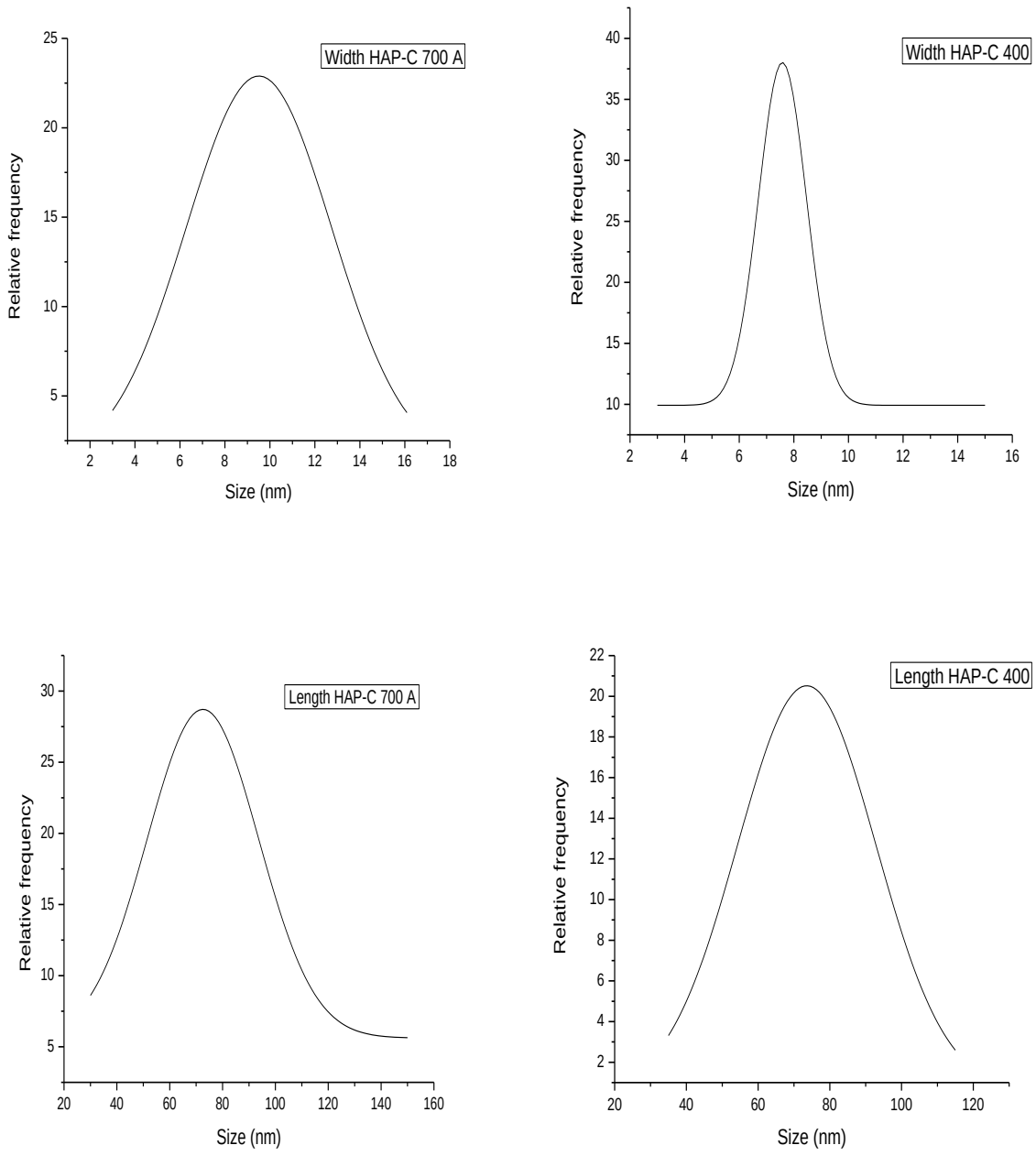

Figure 19 Particle size distribution for HAP-C 400, and HAP-C 700 A

`

5.3 Effect of Operating Parameters

In the following the sections, all the studies were conducted by using the HAP-C 700 A adsorbent. This adsorbent showed enhanced performance over the other adsorbents, which was a result of increased pore width and pore volume.

5.3.1 Effect of pH

pH greatly influences the performance of an adsorbent, by causing protonation and deprotonation of adsorbate. RB exists in either of two forms depending on the pH of the polar solution it exists in. The cationic form exists at pH value less than that of the pK_a (i.e., 3.7), and it exists as a zwitterion at pH values greater than that of the pK_a. (Inyinbor et al., 2015; Mohammadi et al., 2010). The effect of pH on the adsorption of RB (Figure 20 a) onto HAP-C 700A was studied by varying the pH between 3 and 9, at a contact time of 3.5 h, initial adsorbate concentration of 25 mg/L and an adsorbent dose of 3.8 g/L.

`

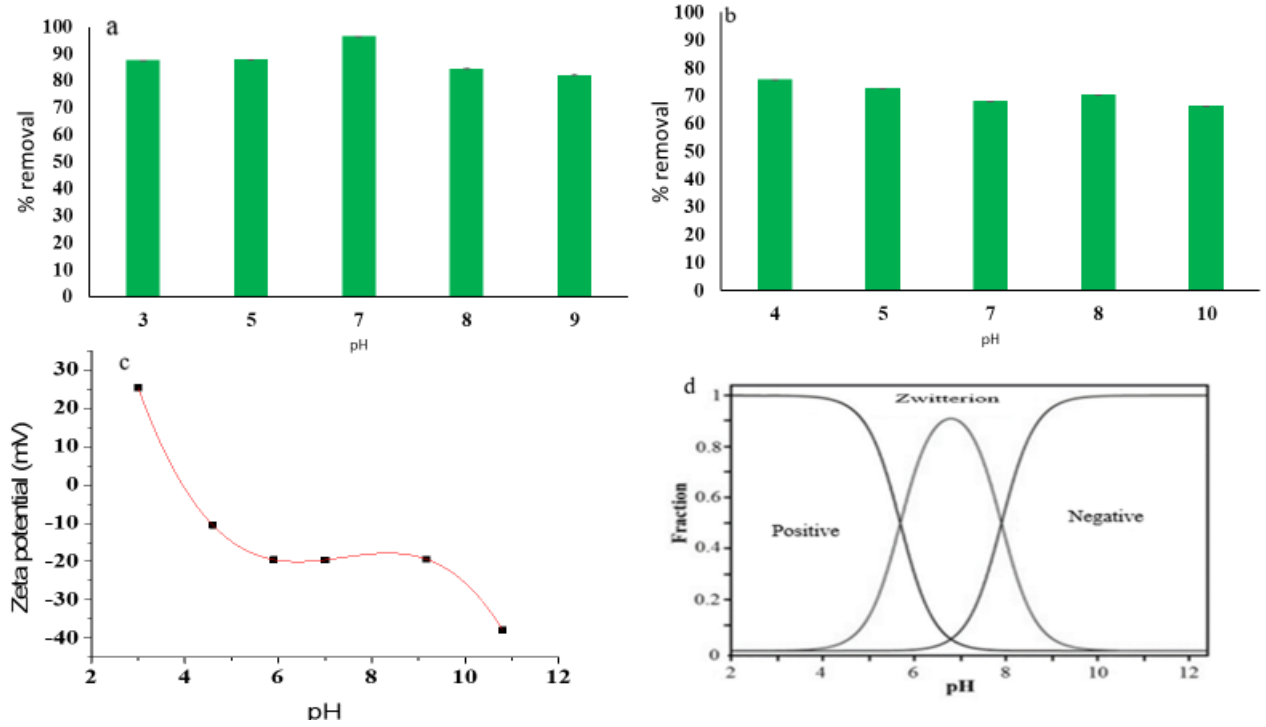

Figure 20 Effect of pH on % removal of a) RB and b) LV onto HAP-C 700 A at 3.8g/L dose, 3.5 h contact time and 25 mg/L initial concentration, c) Zeta potential of HAP-C 700A, and d) LV charge distribution as a function of pH (Ciobanu & Harja, 2018).

It can be clearly seen that the highest removal was achieved at pH value of 7. Below pH 7 the removal percentage increases with increasing the pH; however, the increase is more pronounced in the pH range of 5 to 7. In the acidic region, H^+ ions compete with RB over the sorption sites (Oladipo & Gazi, 2016). This explains the highest removal percentage at pH 7, where the solution is neutral, i.e., there is less competition for sites. As the pH increases above 7, the removal decreases which can be attributed to electrostatic attraction taking place between xanthene groups and carboxyl groups on RB monomers, ending up in forming dimers. The formation of dimers, ultimately leads to an increase in molecular size of the adsorbate and hinders its adsorption and diffusion into the active pores (Inyinbor et al., 2015; Mohammadi et al., 2010). Even though, this

`

interaction can take place at pH values greater than that of the pK_a, however, this behavior was noticed to be more prominent at pH >7.

The surface charge of the adsorbent is also affected by the pH of the solution. Therefore, determining the point of zero charge (PZC) is another important factor that affects the adsorption process. Figure 20 (c) depicts the zeta potential of HAP-C 700 A with varying pH values, where it can be deduced that PZC to is 3.9. The charge on the surface of the adsorbent would be then, positive below the PZC and negative above it. Therefore, in the pH range of 5-7, HAP-C 700 A is negatively-charged while the dye is zwitterion (pK_a=3.7), hence, they were possibly bound via electrostatic interaction in addition to hydrogen bonding, which explains the high removal shown in this pH range. Since the highest removal of RB is achieved at pH 7, this pH is chosen as the working pH for further adsorption studies.

The effect of pH on the removal of LV was also studied as shown in Figure 20 (b), by varying the pH between 4 and 10, at 3.5 h contact time, 25 mg/L initial adsorbate concentration, and 3.8 g/L adsorbent dose. LV exhibits all the three forms namely, anionic, cationic and zwitterionic depending on the solution pH as shown from its speciation diagram in Figure 20 (d).

Clearly from Figure 20 (b), the removal of LV was not notably affected by pH of the solution. The removal percentage ranged between 66.4 % at pH 10 and 75.8 % at pH 4. Hence, all of the following adsorption runs will be conducted at pH 4. The relatively increased removal efficiency of LV at pH of 4 and 5 can be attributed to electrostatic interaction between the negatively-charged adsorbent and positively-charged adsorbate at these specific pHs, but this does not negate the possibility of binding through other mechanisms such as H-bonding and van der Waals forces.

`

5.3.2 Effect of contact time

The effect of contact time was studied by performing adsorption experiments at different time intervals and different initial concentrations of RB and LV. The initial concentrations of RB tested were 10, 15, 25 and 50 ppm, at an adsorbent dose of 3.8 g/L, pH= 7 and 25± 2°C. Same conditions were applied for LV adsorption but its optimal pH of 4 was employed. Figure 21 (a-d) shows the adsorption profiles of the respective percent removal and adsorption capacity (q_e) for RB and LV as a function of time. A steep increase in the removal percentage and q_e can be observed initially then the rate of increase slows down as the profiles approach equilibrium. For the low concentration profiles (10 and 15 ppm), they reached equilibrium in the first 5-10 min and hence they describe instantaneous adsorption. For the higher concentration profiles (25 and 50 ppm), they reached equilibrium after about 2 h. The rate of removal slows down due to the saturation of active binding sites as time elapses, until complete saturation is achieved where no significant increase in the removal percentage or q_e occurs, and hence, equilibrium is attained.

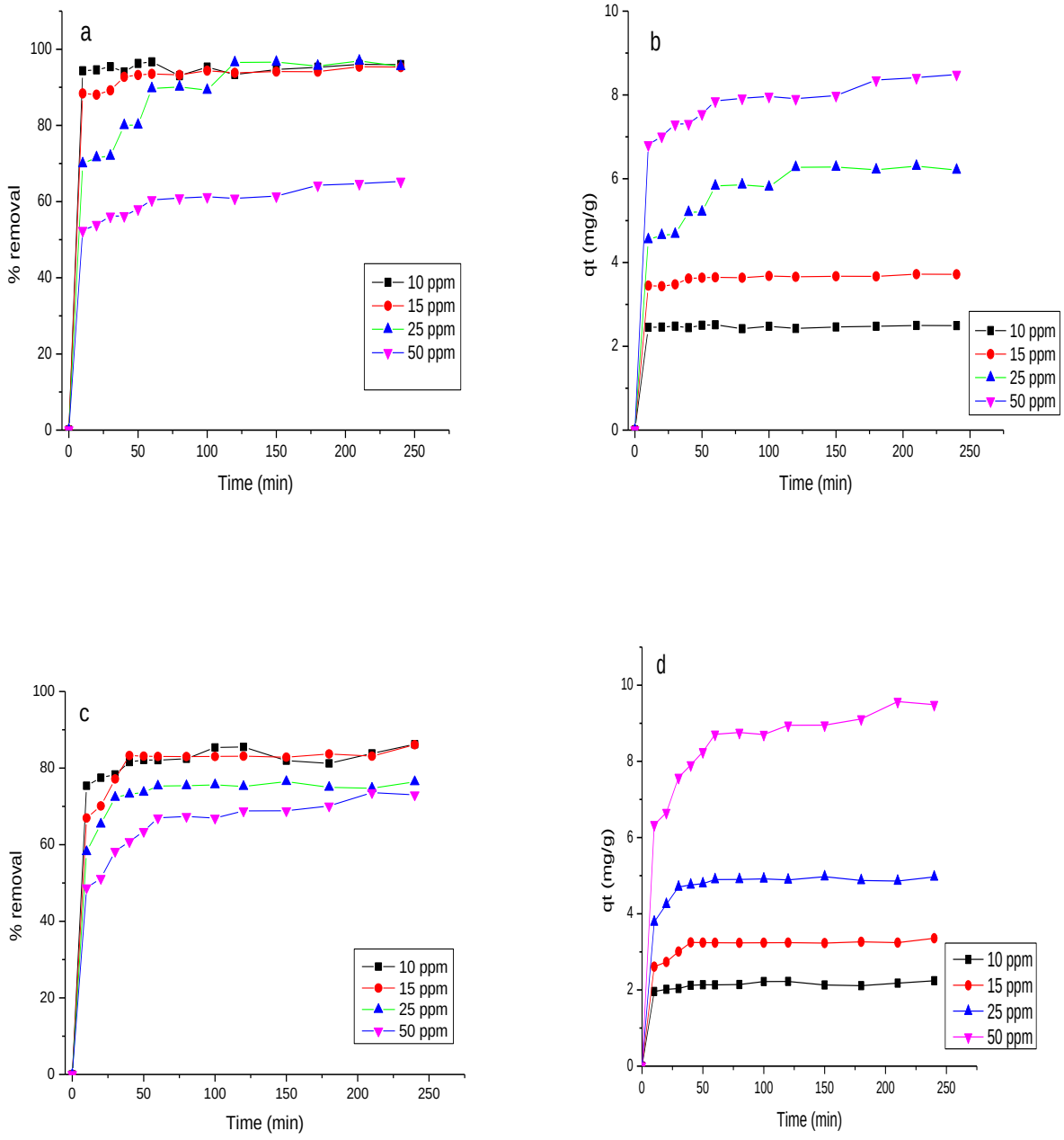

Figure 21 Effect of contact time on percent removal and adsorption capacity of RB (a, b) and LV (c, d), respectively onto 3.8 g/L HAP-C 700 A under different initial concentrations at pH 7 for RB and pH 4 for LV.

`

The highest removal percentage recorded for LV is 86 % at 10 and 15 ppm and it is less than that of RB removal which is 96 % at 10, 15, and 25 ppm initial concentrations. Meanwhile, the q_e is observed to increase with increasing the initial concentration in either RB or LV. At 50 ppm, q_e reached 9.5 and 8.5 mg/g for LV and RB, respectively. The direct proportionality between q_e and the initial concentration can be ascribed to the increased concentration gradient which led to enhanced mass transfer (Bayomie et al., 2020). Nevertheless, the removal efficiencies decreased notably for both adsorbates at this high initial concentration, possibly due to saturation of adsorption sites (Bayomie et al., 2020;Werkneh et al., 2014).

5.3.3 Effect of adsorbent dose

Studying the effect of adsorbent dose is of paramount importance in the economics of the adsorption process (Radnia et al., 2012). Hence, different HAP-C 700A doses were investigated, i.e., 1, 2, 3.8, 6 and 7 g/L at various initial adsorbate concentrations for 210 min contact time, at 25± 2°C and using pH 7 and pH 4 for RB and LV, respectively. The dose profiles for the adsorption of RB and LV under these conditions are shown in Figure 22 (a-d).

`

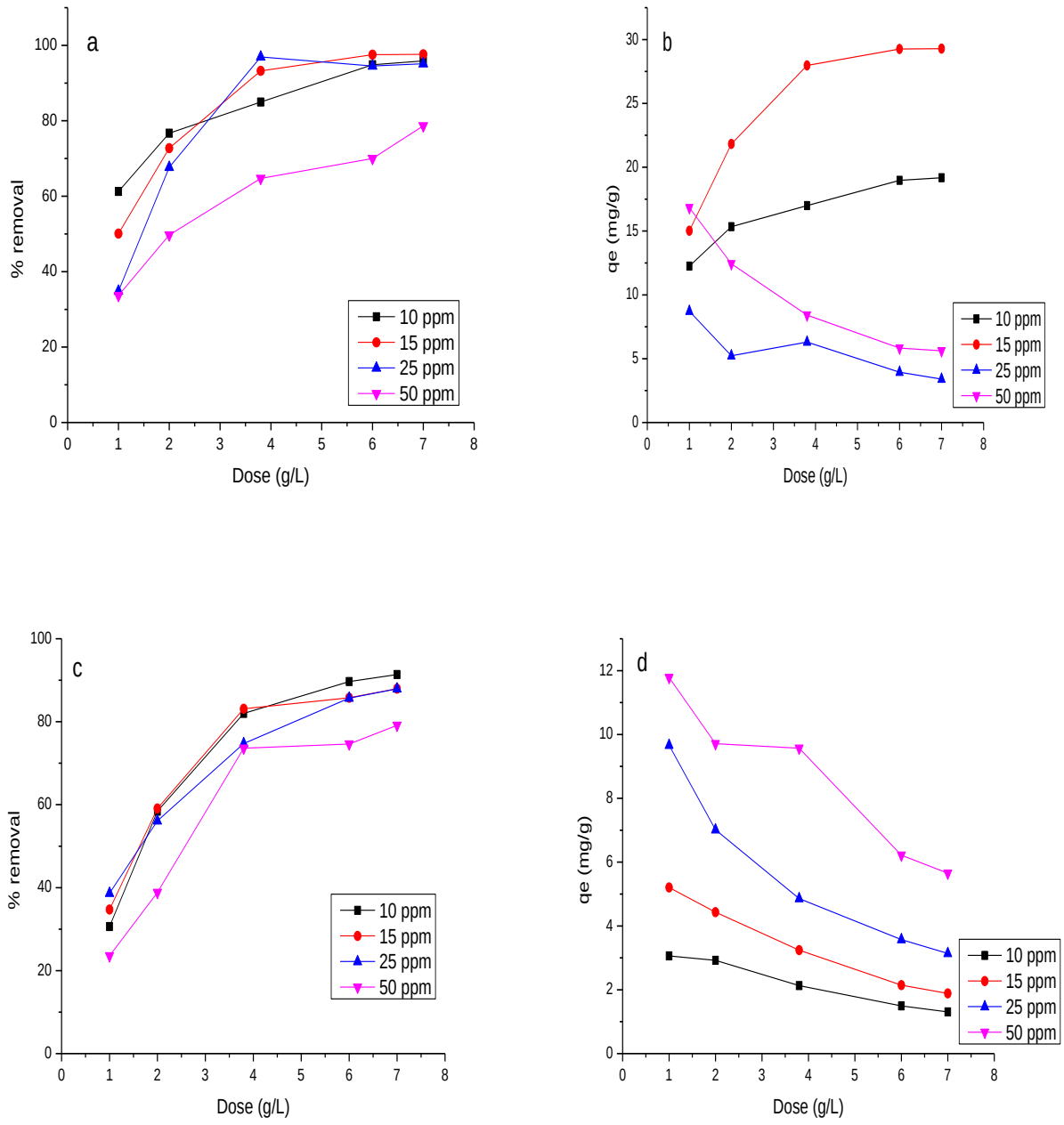

Figure 22 Effect of adsorbent dose on percent removal and adsorption capacity of RB (a, b) and LV (c, d), respectively onto HAP-C 700 A under different initial concentrations for 3.5 h contact time at pH 7 for RB and pH 4 for LV.

`

The equilibrium removal of RB increases as the adsorbent dose increases. On the other hand, q_e is observed to increase as the adsorbent dose increases for the 10 ppm and 15 ppm initial concentrations. In case of higher initial concentrations of 25 and 50 ppm, q_e declines as the adsorbent dose increases. The increase in removal efficiency can be explained by the increase of available active sites on the surface of the adsorbent due to the increase of the amount of adsorbent (Werkneh et al., 2014). The decrease of the adsorption capacity in case of 25 and 50 ppm could, however, be owed to unsaturation or overlapping of the available sorption sites and aggregation of particles, this can be evidenced by the percent removal, that did not similarly decrease (Padmavathy et al., 2016; Bayomie et al., 2020).

By inspecting the same profiles for LV at pH 4 (Figure 22 (c)), it can be deduced that the equilibrium percent removal increases as adsorbent dose increases for all profiles (Figure 22 d), but the q_e decreases. The decrease in adsorption capacity may be, again, explained by the unsaturation of active sites or aggregation of particles during the adsorption process, such behavior has been reported in previous literature (Gorzin & Bahri Rasht Abadi, 2018; Radnia et al., 2012).

5.3.4 Effect of Initial Adsorbate Concentration

The effect of initial adsorbate concentration on q_e and percent removal was studied by employing different initial concentrations while holding other parameters constant. Figure 23(a) depicts the initial concentration profiles for RB adsorption onto HAP-C 700 A at 3.5 h contact time, a dose of 3.8 g/L, and pH 7.

`

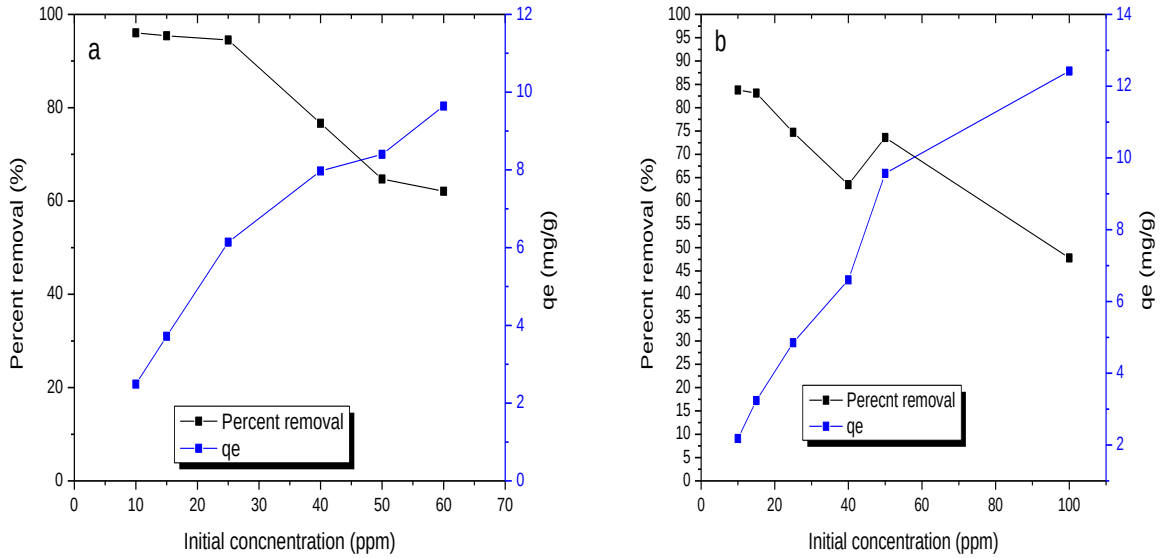

Figure 23 Effect of initial concentration on the percent removal and q_e of RB (a)and LV (b) onto HAP-C 700, respectively for 3.5 h contact time, a dose of 3.8 g/L at pH 7 for RB and pH 4 for LV.

Obviously, q_e increases almost linearly with respect to the initial concentration of RB (Figure 23a). This can be attributed to the increased concentration gradient, which enhances mass transfer of the adsorbate into the adsorbent (Mohammad & El-Sayed, 2020). The effect of initial concentration is associated with decrease in percent removal at higher initial concentrations, but with almost negligible effect at lower initial concentrations. The former might be attributed to the saturation of available adsorption sites (S. L. Narayanan et al., 2014). . The highest removal recorded was 96 % at an initial concentration of 10 ppm, while the highest q_e was 9.64 mg/g at 60 ppm initial concentration.

The corresponding profiles for LV adsorption at pH 4 are shown in Figure 23 (b). The effect of initial concentration on LV is similar to that of RB, where q_e increases linearly while the percent removal decreases with increasing concentration. The highest removal was 83.8 % recorded at an

`

initial concentration of 10 ppm, while the highest q_e was 12.42 mg/g at 100 ppm initial concentration.

5.3.5 Effect of Temperature

The effect of temperature was studied from 30 °C to 80 °C. The adsorption runs were conducted by fixing the contact time at 210 min, the dose at 3.8 g/L and the initial concentration at 25 ppm for both adsorbates. Figure 24 illustrates the impact of temperature on the removal and q_e of both adsorbates. For both adsorbates, it was observed that the percent removal as well as q_e decrease as the temperature increases, implying that the adsorption of RB and LV onto HAP-C 700A is an exothermic process.

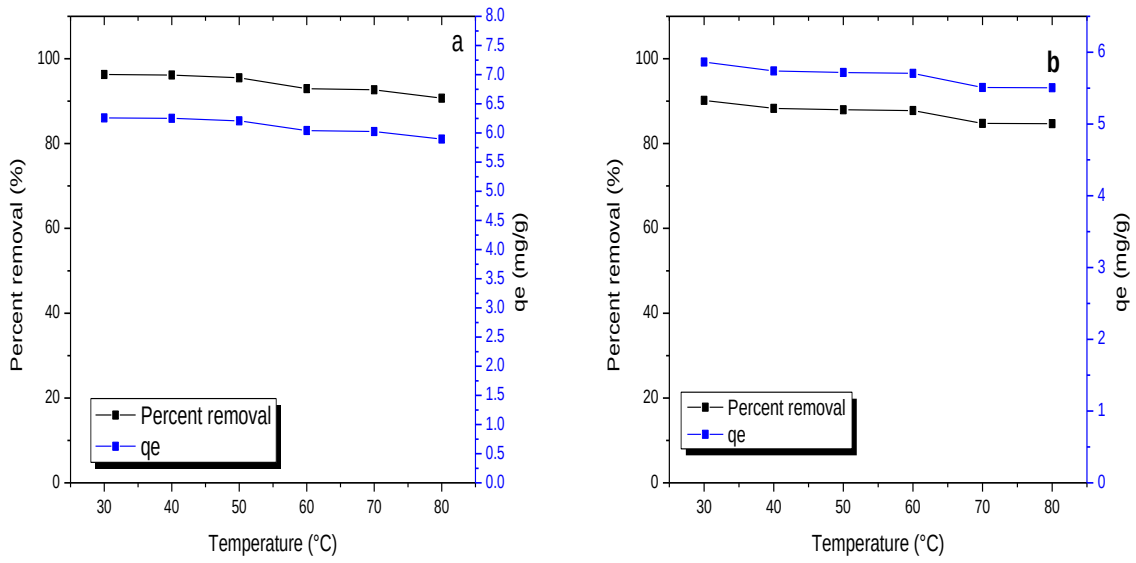

Figure 24 Effect of temperature on a) RB and b) LV removal and adsorption capacity at an adsorbent dose of 3.8 g/L, contact time of 3.5 h at pH 7 for RB and pH 4 for LV.

To determine the heat of adsorption, the linear plots of van't Hoff equation were investigated, and are presented in Figure 25 (a & b) for RB and LV, respectively.

`

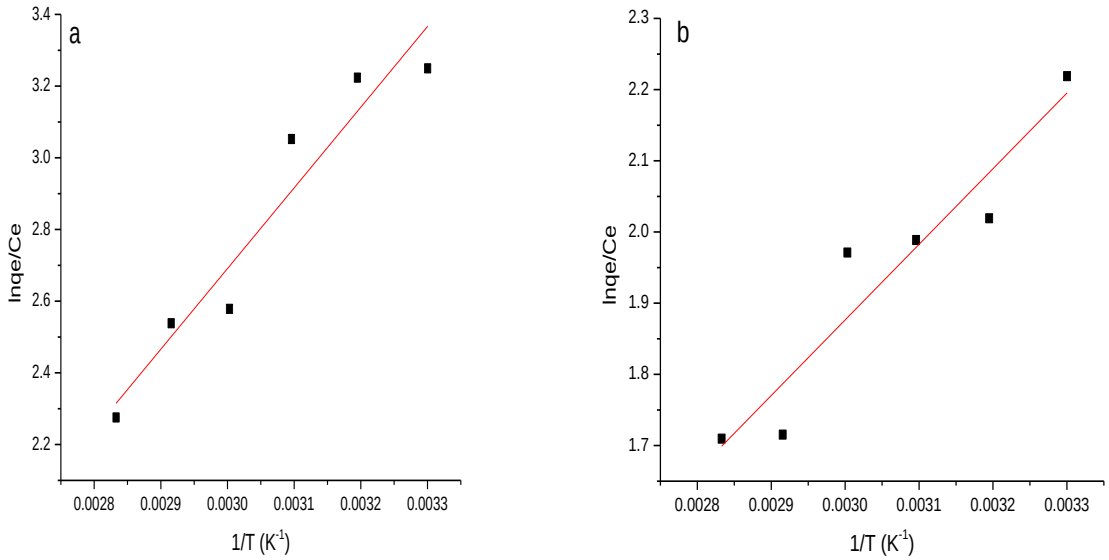

Figure 25 van't Hoff plots for a) RB and b) LV adsorption.

From these plots, the thermodynamic parameters were calculated, which are summarized in Table 11.

Table 11 Thermodynamic parameters for RB and LV adsorption

	RB			***LV***		
Temperature (K)	**Δ*G*** (kJ/mol)	**Δ*H*** (kJ/mol)	**Δ*S*** (J/mol K)	**Δ*G*** (kJ/mol)	**Δ*H*** (kJ/mol)	**Δ*S*** (J/mol K)
303	-8.185			-5.589		
313	-8.388			-5.254		
323	-8.196			-5.234		
333	-7.138	-18.7115	-33.7598	-5.457	-8.828	-10.883
343	-7.238			-4.892		
353	-6.678			-5.018		

`

The negative values of enthalpy change **(**ΔH) confirm that the adsorption process is an exothermic process. The ΔH values also indicate the type of interaction taking place between the adsorbent and the adsorbate, i.e., physisorption or chemisorption. Since ΔH values of both processes lie in the range 10-40 kJ/mol, then the interaction is inferred to be physisorption interaction (Egbosiuba et al., 2019). The negative values of Gibbs free energy (ΔG) indicate a spontaneous adsorption process, this might be related to the instantaneous adsorption observed in both adsorption processes. The values of ΔS are negative for the adsorption of both RB and LV indicating less randomness in the system due to adsorption.

5.4 Adsorption Isotherms

Adsorption isotherms illustrate the adsorbate-adsorbent interaction at equilibrium. Experimental adsorption data was fitted to various adsorption isotherm models. The validity of the adsorption isotherm models for fitting the experimental adsorption data was determined by calculating the coefficient of determination (R^2) and Chi-square ($\chi 2$), where the highest R^2 value indicate the best model and $\chi 2$ values confirm the goodness of the fit. The experimental profile for the isotherm of RB onto HAP-C 700 A at pH 7 and the predicted profile according to Langmuir are shown in Figure 26, while the linear plots predicted by Langmuir, Freundlich, Sips, and D-R models are illustrated in Figure 27 a, b, c, and d, respectively. The estimated isotherm parameters for each model are compiled in Table 12.

`

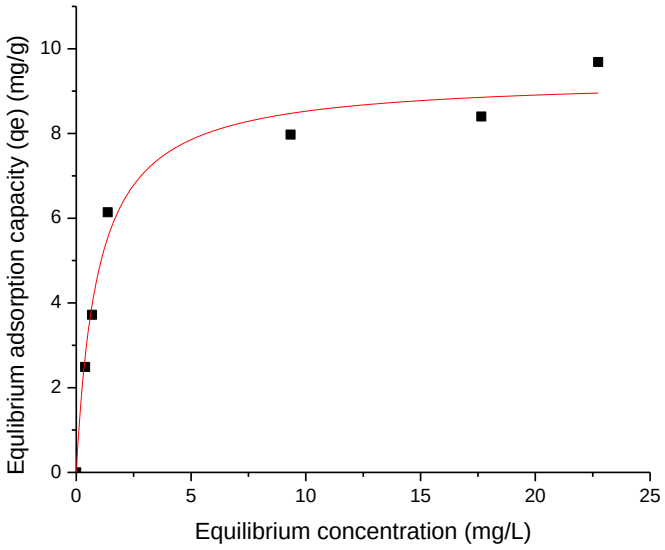

Figure 26 Experimental adsorption isotherm of RB onto HAP-C 700 A at pH 7 and 25 ±2 °C, along with the predicted Langmuir isotherm

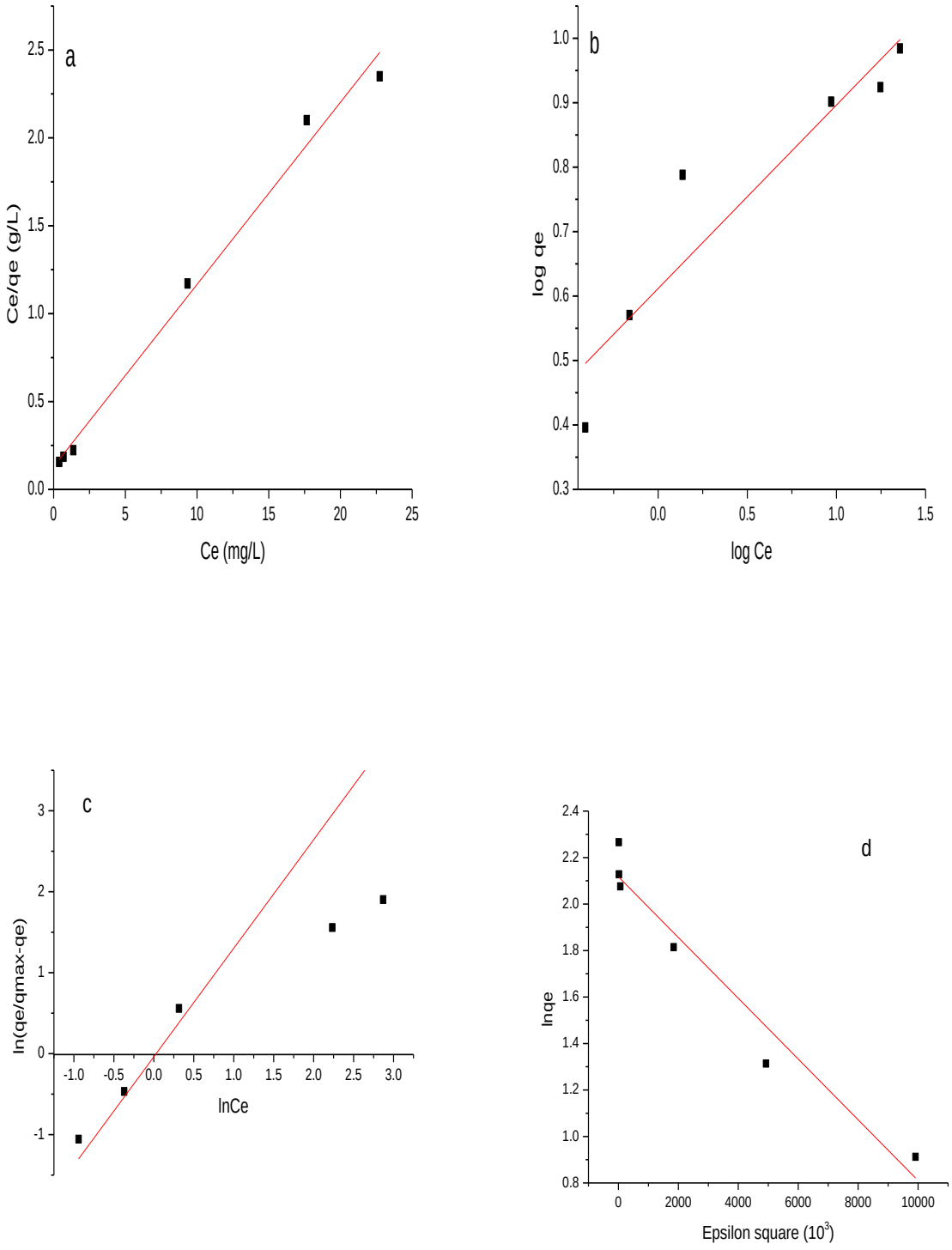

Figure 27 Linear plots for Langmuir (a), Freundlich (b), Sips (c), and D-R (d) models for the adsorption of RB onto HAP-C 700 A at pH 7 and 25±2 °C.

`

Table 12 Langmuir, Freundlich, Sips, and D-R isotherm parameters for RB adsorption onto HAP-C 700 A at pH 7 and 25 ±2 °C

Isotherm model	**Parameter**	
Langmuir	q_m	9.651 (mg/g)
	K_L	0.797(L/mg)
	R^2	0.980
	χ^2	0.035
Freundlich	$1/n$	0.2846
	K_f	4.091 (mg/g)(L/mg)$^{1/n}$
	R^2	0.884
	χ^2	0.051
Sips	N	0.746
	K_s	0.963 (L/mg)$^{1/n}$
	R^2	0.670
	χ^2	4.292
D-R	q_m	8.309 (mg/g)
	B	-1.30712E-07 (mg/g)(J/mol)^2
	R^2	0.957
	χ^2	0.0412

`

From the values of $\chi^2$and R^2 given in Table 12, it can be deduced that the best isotherm model that fits the experimental data is Langmuir model, since it yielded the highest R^2 value while its $\chi 2$ is less than the p-value (0.05). This was furthermore proved by calculating the separation factor (R_L). Table 13 summarizes the values of R_L, which range between 0 and 1 implying favorable adsorption (Mohammad & El-Sayed, 2020). The energy calculated using the D-R model was found to be 1.956 kJ/ mol, since it is less than 8kJ/mol then it represents physisorption, which is in agreement with the conclusion drawn from the thermodynamic study.

Table 13 Summary of values of R_L for RB adsorption

q_e (mg/g)	C_o (mg/L)	K (L/mg)	R_L
2.49	10	0.891	0.100
3.72	15	0.909	0.068
6.14	25	1.28	0.030
7.97	40	0.508	0.047
8.4	50	0.379	0.050
9.64	60	46.549	0.0004

The same procedures were employed for LV experimental data, and the corresponding isotherm plots and linear plots were obtained as depicted in Figure 28 & 29, respectively.

`

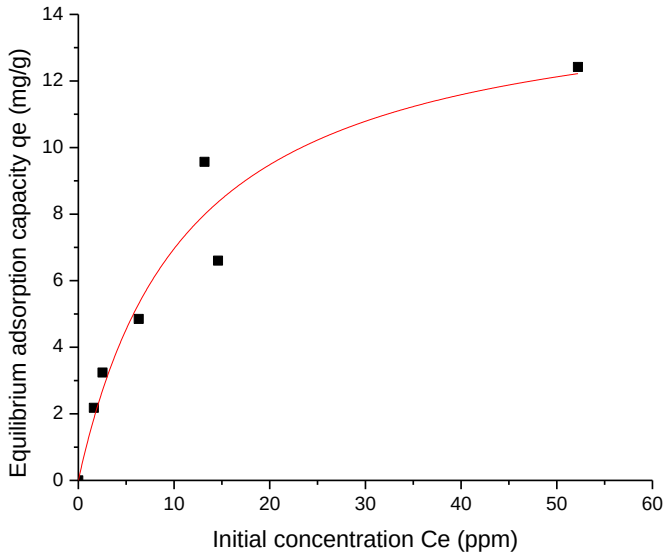

Figure 28 Adsorption isotherm of LV onto HAP-C 700 A at pH 7 and 25 ±2 °C along with predicted Langmuir isotherm

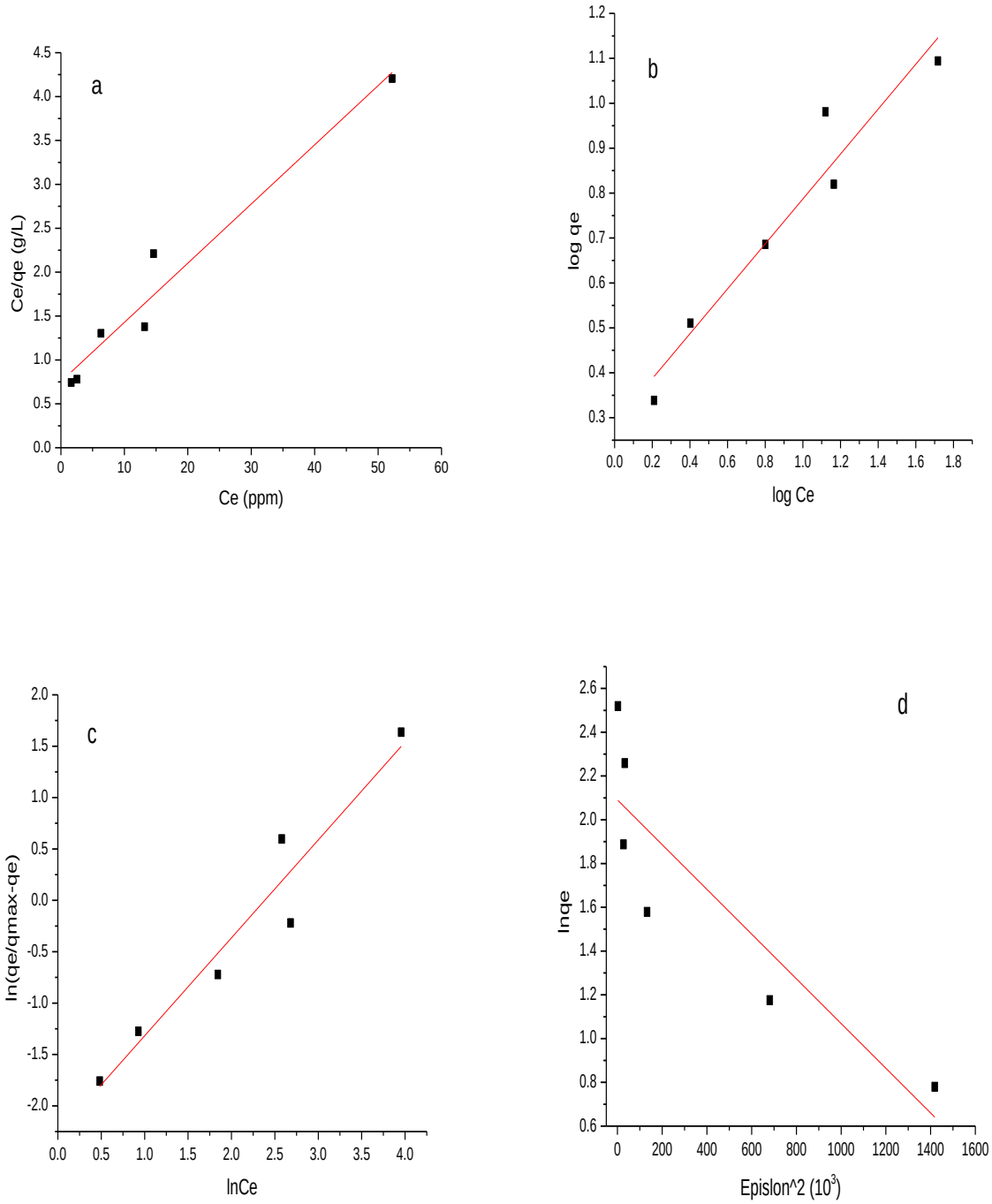

Figure 29 Linear plots for Langmuir (a), Freundlich (b), Sips (c), and D-R (d) models for the adsorption of LV onto HAP-C 700 A at pH 7 and 25±2 °C.

`

Table 14 summarizes the fitting isotherm parameters as predicted by Langmuir, Freundlich, Sips and D-R models. From the table, it can be deduced that the best fit for the adsorption experimental data is Langmuir isotherm, since it yielded the highest R^2 value and its $\chi 2$ is less than the p-value (0.05).

`

Table 14 Langmuir, Freundlich, Sips and D-R isotherm parameters for LV adsorption onto HAP-C 700 A at pH 7 and 25 ±2 °C

Isotherm model	Parameter	
Langmuir	q_m	14.836 (mg/g)
	K_L	0.0895 (L/mg)
	R^2	0.959
	χ^2	0.220
Freundlich	$1/n$	0.50006
	K_f	1.936 (mg/g)(L/mg)$^{1/n}$
	R^2	0.935
	χ^2	0.035
Sips	n	1.049
	K_s	0.103 (L/mg)$^{1/n}$
	R^2	0.936
	χ^2	1.713
D-R	q_m	8.089
	β	-1.02E-06 (mg/g)(mol/J.)^2
	R^2	0.784
	χ^2	0.237

`

The energy calculated using the D-R model for LV adsorption was 0.7kJ/mol, which indicates a physisorption process since it is less than 8 kJ/mol, and this is in agreement with the thermodynamics study.

5.5 Adsorption Kinetic Modelling

The adsorption kinetics was studied for both RB and LV at initial concentrations of 10, 15, 25 and 50 ppm and 3.8 g/L adsorbent dose at pH 7 for RB and pH 4 for LV. The experimental kinetic plots for RB and LV (Figures 30 and 31) were fitted to the pseudo-first order (Figure 30) and the pseudo-second order (Figure 31) kinetic models, and the best fit was determined by the highest R^2 value. Then, using the slopes and the intercepts of the plots the rate constants were determined. For both RB and LV adsorption, the values of R^2 pertaining to the pseudo-first order are lower than their counterparts for the pseudo-second order model, indicating that the process of adsorption of each RB and LV onto HAP-C 700 A can be best described by the pseudo-second order kinetic model. The rate constants obtained from both linear plots at different initial RB or LV concentrations are summarized in Table 15.

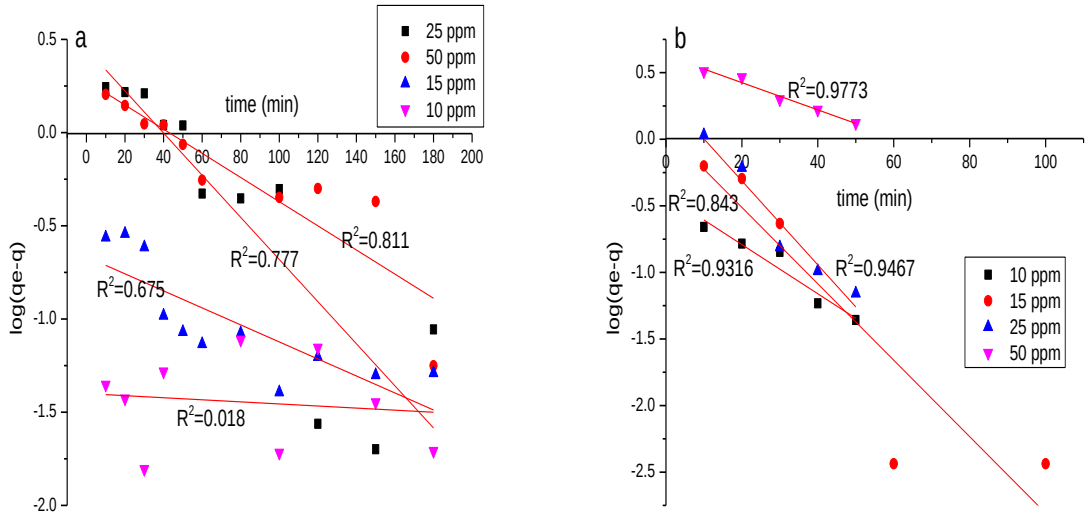

Figure 30 Pseudo-first order kinetic plot for a) RB and b) LV onto HAP-C 700 A at pH 7 for RB and pH 4 for LV and 25 ± 2°C.

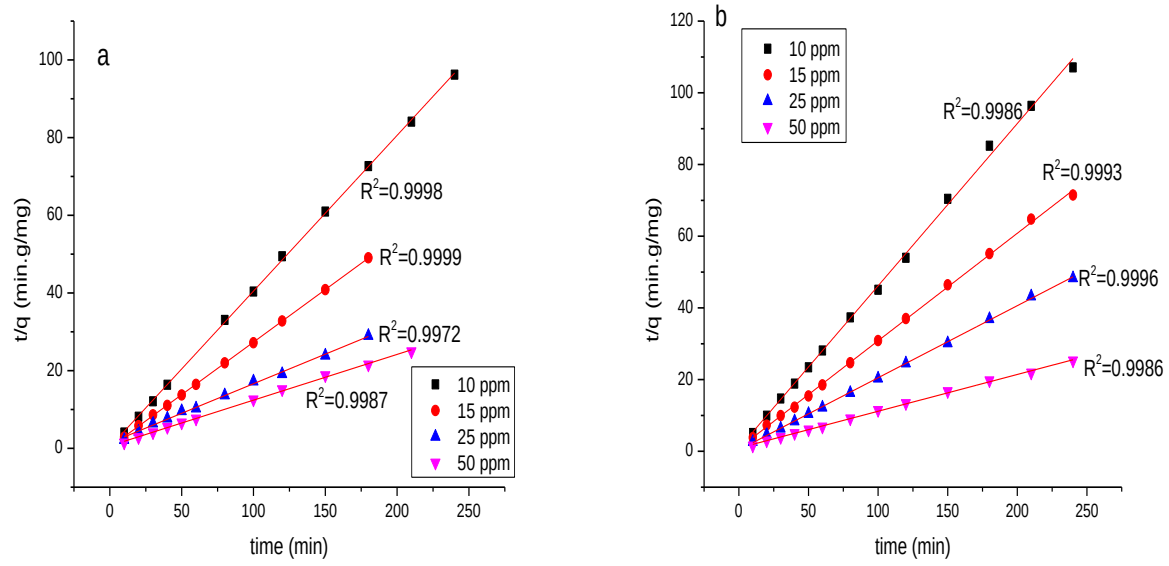

Figure 31 Pseudo-second order kinetic plot for a) RB and b) LV onto HAP-C 700 A at pH 7 for RB and pH 4 for LV and 25 ± 2°C.

`

Table 15 Kinetic rate constants (*k*) at different initial concentrations of RB and LV

	RB				***LV***			
C_o (ppm)	k_1 (min^{-1})	R^2	k_2 (g/mg.min)	R^2	k_1 (min^{-1})	R^2	k_2 (g/mg.min)	R^2
10	0.0005	0.018	0.409	0.999	0.018	0.932	0.427	0.999
15	0.0045	0.675	0.244	0.999	0.029	0.843	0.076	0.999
25	0.011	0.811	0.016	0.997	0.032	0.947	0.016	0.999
50	0.0065	0.777	0.022	0.998	0.010	0.997	0.009	0.999

It can be clearly seen that the rate constant for the pseudo-second order model decreases as the initial concentration of adsorbate increases. Figure 32 depicts the relation between the rate constant and the initial concentration of RB and LV. The decrease in the pseudo-second order rate constant with increasing the initial concentration of RB or LV can be ascribed to the saturation of active sites.

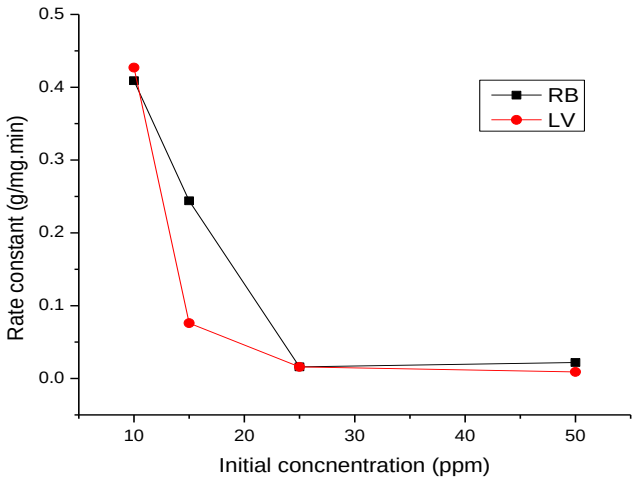

Figure 32 Relation between pseudo-second order rate constant and initial concentration.

`

5.6 Assessment of Binary System

The adsorption capacity and removal efficiency of HAP-C 700A in a binary system was investigated via two runs, in which the initial concentration for both adsorbates was 10 ppm. The solution pH was set at 7, because at this pH the removal efficiency of RB was the highest and even though this was not the case for LV, however, there was no significant variation in removal efficiency as the pH changed from 4 to 7. The temperature was kept at 25± 2°C, the dose at 3.8 g/L and contact time at 240 min.

Table 16 Comparison of adsorption capacities and removal efficiencies of RB and LV in single and binary systems at pH 7

C_o (ppm)	% Removal of RB	q_e of RB (mg/g)	% Removal of LV	q_e of LV (mg/g)
10 (binary system)	96.46	2.31	77.68	2.02
10 (single system)	90.64	2.38	78.69	2.05

It can be observed that at this specific initial concentration the performance of the adsorbent in both systems is comparable, indicating that no considerable competition between the adsorbates existed. It could be that their dominant binding mechanisms are different; RB is likely to bind by electrostatic interactions between its positively-charged groups and the negatively-charged HAP-C 700 A at pH 7, while LV probably binds via hydrogen bonding since it is a zwitterion at this pH.

5.7 Adsorption Mechanism

To elucidate the underlying adsorption mechanism, FTIR spectra before and after adsorption of RB and LV were examined as shown in Figure 33. In case of RB, a significant shift from 3466.9 cm^{-1} to 3446.4 can be observed along with less broadening in the OH peak. The same shift and

`

broadening also occurred with LV, specifically from 3466.9 cm^{-1} to 3448.5 cm^{-1}. This implies that OH plays a role in binding. It is thus, suggested that binding occurs either via electrostatic interaction or hydrogen bonding. For example, the OH groups of HAP-C 700 A could possibly interact with the OH groups, or the N^+ of RB, and it could interact with the OH groups, or lone pairs of the N atoms of LV.

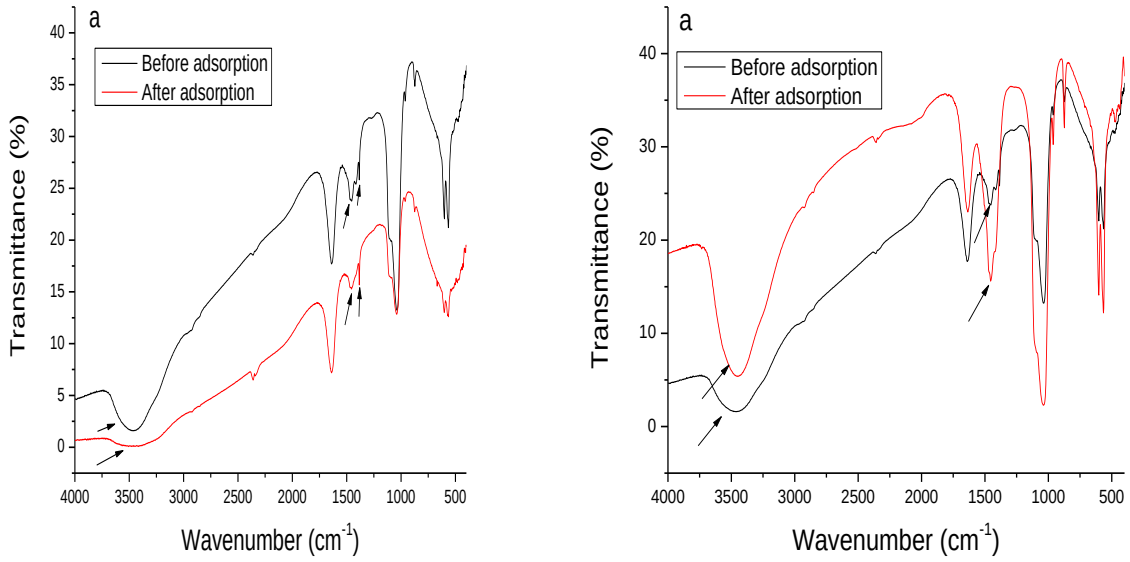

Figure 33 FTIR analysis before and after adsorption of a) RB and b) LV onto HAP-C 700 A.

This mechanism is in agreement with the earlier drawn conclusions about binding mechanisms. That is to say, that the positively-charged groups of RB and LV were bound to the negatively-charged adsorbent by physical forces such as electrostatic attraction or hydrogen bonding, since the enthalpy of adsorption was found to be below 40 kJ/mol.

`

Chapter 6

`

6. Conclusion and Future Work

A novel approach was used to synthesize HAP-C nanocomposite as a value-added product the industrial waste of CKD. In the due process, citric acid was used successfully to separate the calcium from the CKD by chelation. The chelate was then converted to a mixture of calcium carbonate and carbon. The formation of the composite was confirmed by XRD, FTIR and TEM analysis. The textural and surface properties of the composite were also analyzed to study the effect of surface area, pore volume and pore size on the adsorption process. The synthesized composite was then utilized for the removal of RB dye and LV drug in single systems, and its adsorption performance was assessed in binary systems. Excellent removal efficiencies were recorded for both adsorbates in single systems, i.e., 96% for RB with initial concentrations of 10, 15, and 25 ppm, and 86 % for LV with initial concentrations of 10, 15 ppm. The maximum adsorption capacities estimated by Langmuir isotherm model were 9.65 and 14.84 mg/g for RB and LV, respectively. In the binary system, the preliminary assessment revealed that the composite possesses a high potential for simultaneous removal of RB and LV with no considerable competition between the two contaminants on the active sites. Thermodynamic study of the adsorption process revealed that the adsorption of both RB and LV onto HAP-C 700 A was spontaneous, and the interaction was physisorption. This conclusion was further supported by FTIR conducted before and after adsorption, which suggested that OH groups are responsible for the binding that probably occurs by means of electrostatic attraction forces and hydrogen bonding. The kinetic study revealed that adsorption process for both adsorbates followed the pseudo-second order model which suggests that the adsorption takes place via surface reaction, film and pore diffusion.

Future work will include:

`

- Complete study of adsorption in a binary system of RB and LV.
- Assessment of the potential of using the composite in continuous packed bed columns for both single and binary systems.
- Assessment of the adsorption potential of the composite for heavy metals, specifically lead.
- Assessment of the potential of composite to be re-used, i.e., regeneration.

`

References

A. De Caro, C. (2015). UV / VIS Spectrophotometry. *Mettler-Toledo International*, *September 2015*, 4–14. http://lcwu.edu.pk/ocd/cfiles/Chemistry/MSc/Chem-C-410/Fundamentals_UV_VIS.pdf

A. Ruksudjarit, K. Pengpat, G. Rujijanagul, T. T. (2008). Synthesis and characterization of nanocrystalline hydroxyapatite from natural bovine bone. *Current Applied Physics*, *8*(3–4), 270–272. https://doi.org///doi.org/10.1016/j.cap.2007.10.076

Adeogun, A. I., Ofudje, E. A., Idowu, M. A., Kareem, S. O., Vahidhabanu, S., & Babu, B. R. (2018). Biowaste-Derived Hydroxyapatite for E ff ective Removal of Reactive Yellow 4 Dye : Equilibrium , Kinetic , and Thermodynamic Studies. *ACS Publications*, *3*, 1991–2000. https://doi.org/10.1021/acsomega.7b01768

Adeyanju, E., & Okeke, C. A. (2019). Exposure effect to cement dust pollution: a mini review. *SN Applied Sciences*, *1*(12), 1–17. https://doi.org/10.1007/s42452-019-1583-0

Afshar, A., Ghorbani, M., Ehsani, N., Saeri, M. R., & Sorrell, C. C. (2003). Some important factors in the wet precipitation process of hydroxyapatite. *Materials and Design*, *24*(3), 197–202. https://doi.org/10.1016/S0261-3069(03)00003-7

Agbeboh, N. I., Oladele, I. O., Daramola, O. O., Adediran, A. A., Olasukanmi, O. O., & Tanimola, M. O. (2020). Environmentally sustainable processes for the synthesis of hydroxyapatite. *Heliyon*, *6*(4), e03765. https://doi.org/10.1016/j.heliyon.2020.e03765

Agrawal, K., Singh, G., Puri, D., & Prakash, S. (2011). Synthesis and Characterization of Hydroxyapatite Powder by Sol-Gel Method for Biomedical Application. *Journal of Minerals and Materials Characterization and Engineering*, *10*(08), 727–734. https://doi.org/10.4236/jmmce.2011.108057

Akram, M., Ahmed, R., Shakir, I., Ibrahim, W. A. W., & Hussain, R. (2014). Extracting hydroxyapatite and its precursors from natural resources. *Journal of Materials Science*, *49*(4), 1461–1475. https://doi.org/10.1007/s10853-013-7864-x

Alhasan, H. S., Alahmadi, N., Yasin, S. A., Khalaf, M. Y., & Ali, G. A. M. (2022). *Low-Cost and Eco-Friendly Hydroxyapatite Nanoparticles Derived from Eggshell Waste for Cephalexin Removal*.

Altaf, S., Zafar, R., Qamar, W., Ahmad, S., Yaqoob, K., Syed, A., Jahangir, A., Bilal, M., & Arshad, M. (2021). Ecotoxicology and Environmental Safety Removal of levofloxacin from aqueous solution by green synthesized magnetite (Fe 3 O 4) nanoparticles using Moringa olifera : Kinetics and reaction mechanism analysis. *Ecotoxicology and Environmental Safety*, *226*, 112826. https://doi.org/10.1016/j.ecoenv.2021.112826

Alvarez-lloret, P., Rodrı, A. B., & Falini, G. (2010). *Crystallographic Control of the Hydrothermal Conversion of Calcitic Sea Urchin Spine (Paracentrotus lividus) into Apatite*. https://doi.org/10.1021/cg101012a

Amiri, A., Chahkandi, M., & Targhoo, A. (2017). Synthesis of nano-hydroxyapatite sorbent for microextraction in packed syringe of phthalate esters in water samples. *Analytica Chimica*

`

Acta, *950*, 64–70. https://doi.org/10.1016/j.aca.2016.11.027

Arkin, V. H., Lakhera, M., Manjubala, I., & Narendra Kumar, U. (2015). Solid state synthesis and characterization of calcium phosphate for biomedical application. *International Journal of ChemTech Research*, *8*(6), 264–267.

Bahrololoom, Mohammad & Javidi, Mohsen & Javadpour, Sirus & Ma, J. . (2009). Characterisation of natural hydroxyapatite extracted from bovine cortical bone ash. *Journal of Ceramic Processing Research*, *10*, 129–138.

Baldev, E., MubarakAli, D., Ilavarasi, A., Pandiaraj, D., Ishack, K. A. S. S., & Thajuddin, N. (2013). Degradation of synthetic dye, Rhodamine B to environmentally non-toxic products using microalgae. *Colloids and Surfaces B: Biointerfaces*, *105*, 207–214. https://doi.org/10.1016/j.colsurfb.2013.01.008

Bin Huang , Dan Xiong , Tingting Zhao, H. H. and X. P. (2016). Adsorptive removal of PPCPs by biomorphic HAP templated from cotton. *Water Science & Technology*, *1*, 276–286. https://doi.org/10.2166/wst.2016.209

Brown, M. E. (1989). Introduction to thermal analysis, techniques and applications. In *Thermochimica Acta* (Vol. 155, pp. 383–385). https://doi.org/10.1016/0040-6031(89)87162-x

Buitrago-Vásquez, M., & Ossa-Orozco, C. P. (2018). Hydrothermal synthesis of hydroxyapatite nanorods using a fruit extract template. *Dyna*, *85*(204), 283–288. http://www.scielo.org.co/scielo.php?script=sci_arttext&pid=S0012-73532018000100283&lang=pt%0Ahttp://www.scielo.org.co/pdf/dyna/v85n204/0012-7353-dyna-85-204-00283.pdf

Canillas, M., Rivero, R., García-Carrodeguas, R., Barba, F., & Rodríguez, M. A. (2017). Processing of hydroxyapatite obtained by combustion synthesis. *Boletin de La Sociedad Espanola de Ceramica y Vidrio*, *56*(5), 237–242. https://doi.org/10.1016/j.bsecv.2017.05.002

Chaudhuri, B., Mondal, B., Modak, D. K., Pramanik, K., & Chaudhuri, B. K. (2013). Preparation and characterization of nanocrystalline hydroxyapatite from egg shell and K 2 HPO 4 solution. *Materials Letters*, *97*, 148–150. https://doi.org/10.1016/j.matlet.2013.01.082

Chen, Y., Lan, T., Duan, L., Wang, F., & Zhao, B. (2015). *Adsorptive Removal and Adsorption Kinetics of Fluoroquinolone by Nano-Hydroxyapatite*. https://doi.org/10.1371/journal.pone.0145025

Cho, J. S., & Rhee, S. H. (2012). Preparation of submicron-sized hydroxyapatite powders by spray pyrolysis. *Key Engineering Materials*, *493–494*(3), 215–218. https://doi.org/10.4028/www.scientific.net/KEM.493-494.215

Ciobanu, G., & Harja, M. (2018). Studies on the sorption of levofloxacin from aqueous solutions onto nanohydroxyapatite. *Revue Roumaine de Chimie*, *63*(7–8), 593–601.

Darweesh, H. H. M. (2020). Hazardous Effects of Electrostatic Precipitator Cement Kiln Bypass Dust Waste on both Environment and Public Human Health. *Prime Archives in Biosciences*, 1–35.

`

Darweesh, T. M., & Ahmed, M. J. (2017). Batch and fixed bed adsorption of levofloxacin on granular activated carbon from date (Phoenix dactylifera L .) stones by KOH chemical activation. *Environmental Toxicology and Pharmacology*, *50*, 159–166. https://doi.org/10.1016/j.etap.2017.02.005

Dulio, V., van Bavel, B., Brorström-Lundén, E., Harmsen, J., Hollender, J., Schlabach, M., Slobodnik, J., Thomas, K., & Koschorreck, J. (2018). Emerging pollutants in the EU: 10 years of NORMAN in support of environmental policies and regulations. *Environmental Sciences Europe*, *30*(1). https://doi.org/10.1186/s12302-018-0135-3

Ebelegi, A. N., Ayawei, N., & Wankasi, D. (2020). Interpretation of Adsorption Thermodynamics and Kinetics. *Open Journal of Physical Chemistry*, *10*(03), 166–182. https://doi.org/10.4236/ojpc.2020.103010

Ebnesajjad, S. (2011). Surface and Material Characterization Techniques. In *Handbook of Adhesives and Surface Preparation*. Elsevier Inc. https://doi.org/10.1016/B978-1-4377-4461-3.10004-5

Edet, U. A., & Ifelebuegu, A. O. (2020). Kinetics, isotherms, and thermodynamic modeling of the adsorption of phosphates from model wastewater using recycled brick waste. *Processes*, *8*(6). https://doi.org/10.3390/PR8060665

Edralin, E. J. M., Garcia, J. L., dela Rosa, F. M., & Punzalan, E. R. (2017). Sonochemical synthesis, characterization and photocatalytic properties of hydroxyapatite nano-rods derived from mussel shells. *Materials Letters*, *196*, 33–36. https://doi.org/10.1016/j.matlet.2017.03.016

Egbosiuba, T. C., Abdulkareem, A. S., Kovo, A. S., Afolabi, E. A., Tijani, J. O., Auta, M., & Roos, W. D. (2019). Ultrasonic Enhanced Adsorption of Methylene Blue onto the Optimized Surface Area of Activated Carbon: Adsorption Isotherm, Kinetics and Thermodynamics. *Chemical Engineering Research and Design*. https://doi.org/10.1016/j.cherd.2019.10.016

Fathi, M. H., & Zahrani, E. M. (2009). Fabrication and characterization of fluoridated hydroxyapatite nanopowders via mechanical alloying. *Journal of Alloys and Compounds*, *475*(1–2), 408–414. https://doi.org/10.1016/j.jallcom.2008.07.058

Fernando, M. S., De Silva, R. M., & De Silva, K. M. N. (2015). Synthesis, characterization, and application of nano hydroxyapatite and nanocomposite of hydroxyapatite with granular activated carbon for the removal of Pb 2+ from aqueous solutions. *Applied Surface Science*, *351*, 95–103. https://doi.org/10.1016/j.apsusc.2015.05.092

Ferri, M., Campisi, S., Polito, L., Shen, J., & Gervasini, A. (2021). Tuning the sorption ability of hydroxyapatite/carbon composites for the simultaneous remediation of wastewaters containing organic-inorganic pollutants. *Journal of Hazardous Materials*, *420*(May), 126656. https://doi.org/10.1016/j.jhazmat.2021.126656

Figueiredo, M., Fernando, A., Martins, G., Freitas, J., Judas, F., & Figueiredo, H. (2010). Effect of the calcination temperature on the composition and microstructure of hydroxyapatite derived from human and animal bone. *Ceramics International*, *36*(8), 2383–2393. https://doi.org/10.1016/j.ceramint.2010.07.016

`

Fredeen, C. B. B. and K. J. (2004). *Concepts , Instrumentation and Techniques in Inductively Coupled Plasma Optical Emission Spectrometry* (3rd editio). https://resources.perkinelmer.com/lab-solutions/resources/docs/GDE_Concepts-of-ICP-OES-Booklet.pdf

Gao, X. (2012). *Vanadium Redox Flow Batteries For Large-Scale Energy Storage Electrochemistry, Efficiency and Spectroscopic Monitoring* (Issue February).

Geissen, V., Mol, H., Klumpp, E., Umlauf, G., Nadal, M., van der Ploeg, M., van de Zee, S. E. A. T. M., & Ritsema, C. J. (2015). Emerging pollutants in the environment: A challenge for water resource management. *International Soil and Water Conservation Research*, *3*(1), 57–65. https://doi.org/10.1016/j.iswcr.2015.03.002

Goloshchapov, D. L., Kashkarov, V. M., Rumyantseva, N. A., Seredin, P. V, Lenshin, A. S., Agapov, B. L., & Domashevskaya, E. P. (2012). Synthesis of nanocrystalline hydroxyapatite by precipitation using hen's eggshell. *Ceramics International*. https://doi.org/10.1016/j.ceramint.2012.11.050

Gong, W., Kraft, M., Morgan, H., & Mowlem, M. (2009). A Simple, Low-Cost Double Beam Spectrophotometer for Colorimetric Detection of Nitrite in Seawater. *IEEE Sensors Journal*, *9*(7), 862–869. https://doi.org/10.1109/JSEN.2009.2020659

González-Pleiter, M., Gonzalo, S., Rodea-Palomares, I., Leganés, F., Rosal, R., Boltes, K., Marco, E., & Fernández-Piñas, F. (2013). Toxicity of five antibiotics and their mixtures towards photosynthetic aquatic organisms: Implications for environmental risk assessment. *Water Research*, *47*(6), 2050–2064. https://doi.org/10.1016/j.watres.2013.01.020

Gorzin, F., & Bahri Rasht Abadi, M. M. (2018). Adsorption of Cr(VI) from aqueous solution by adsorbent prepared from paper mill sludge: Kinetics and thermodynamics studies. *Adsorption Science and Technology*, *36*(1–2), 149–169. https://doi.org/10.1177/0263617416686976

Graff, A., Thorpe, M., Chair, G., Ghirlanda, D., Matyushov, S., Ozkan, M., & Treacy. (2011). *Network Models for Materials and Biological Systems*. *June*, 10–12.

Guo, X., Yan, H., Zhao, S., Li, Z., Li, Y., & Liang, X. (2013). Effect of calcining temperature on particle size of hydroxyapatite synthesized by solid-state reaction at room temperature. *Advanced Powder Technology*, *24*(6), 1034–1038. https://doi.org/10.1016/j.apt.2013.03.002

Guo, Y., Yao, Y., Ning, C., Guo, Y., & Chu, L. (2011). Fabrication of mesoporous carbonated hydroxyapatite microspheres by hydrothermal method. *Materials Letters*, *65*(14), 2205–2208. https://doi.org/10.1016/j.matlet.2011.04.057

Gursharan Singh, Shubham Sharm, Manoj Mittal, Gurminder Singh, Jujhar Singh, Li Changhe, Aqib Mashood Khan, Shashi Prakash Dwivedi, RayTahir Mushtaqh, S. (2022). Impact of post-heat-treatment on the surface-roughness, residual stresses, and micromorphology characteristics of plasma-sprayed pure hydroxyapatite and 7%-Aloxite reinforced hydroxyapatite coatings deposited on titanium alloy-based biomedical implants. *Journal of Materials Research and Technology*, *18*, 1358–1380. https://doi.org/https://doi.org/10.1016/j.jmrt.2022.03.065

Ho, W., Hsu, H., Hsu, S., & Hung, C. (2013). Calcium phosphate bioceramics synthesized from

`

eggshell powders through a solid state reaction. *Ceramics International*, *39*(6), 6467–6473. https://doi.org/10.1016/j.ceramint.2013.01.076

Hou, H., Zhou, R., Wu, P., & Wu, L. (2012). Removal of Congo red dye from aqueous solution with hydroxyapatite / chitosan composite. *Chemical Engineering Journal*, *211–212*, 336–342. https://doi.org/10.1016/j.cej.2012.09.100

Hu, Q., & Zhang, Z. (2019). Application of Dubinin–Radushkevich isotherm model at the solid/solution interface: A theoretical analysis. *Journal of Molecular Liquids*, *277*, 646–648. https://doi.org/10.1016/j.molliq.2019.01.005

Ibrahim, A., Wei, W., Zhang, D., Wang, H., & Li, J. (2013). Conversion of waste eggshells to mesoporous hydroxyapatite nanoparticles with high surface area. *Materials Letters*, *110*, 195–197. https://doi.org/10.1016/j.matlet.2013.08.014

Ingham, B., & Toney, M. F. (2013). X-ray diffraction for characterizing metallic films. In *Metallic Films for Electronic, Optical and Magnetic Applications: Structure, Processing and Properties*. https://doi.org/10.1533/9780857096296.1.3

Inyinbor, A. A., Adekola, F. A., & Olatunji, G. A. (2015). Adsorption of rhodamine b dye from aqueous solution on Irvingia gabonensis biomass: Kinetics and thermodynamics studies. *South African Journal of Chemistry*, *68*(1), 115–125. https://doi.org/10.17159/0379-4350/2015/v68a17

Ivanets, A. I., Kitikova, N. V., Shashkova, I. L., Roshchina, M. Y., Srivastava, V., & Sillanpää, M. (2019). Adsorption performance of hydroxyapatite with different crystalline and porous structure towards metal ions in multicomponent solution. *Journal of Water Process Engineering*, *32*(May), 100963. https://doi.org/10.1016/j.jwpe.2019.100963

J.H. Shariffuddin, M.I. Jones, D. A. P. (2013). Greener photocatalysts: hydroxyapatite derived from waste mussel shells for the photocatalytic degradation of a model azo dye wastewater. *Chemical Engineering Research and Design*, *91*, 1693–1704. https://doi.org/10.1016/j.cherd.2013.04.018

Jayaweera, H. D. A. C., Siriwardane, I., de Silva, K. M. N., & de Silva, R. M. (2018). Synthesis of multifunctional activated carbon nanocomposite comprising biocompatible flake nano hydroxyapatite and natural turmeric extract for the removal of bacteria and lead ions from aqueous solution. *Chemistry Central Journal*, *12*(1), 1–14. https://doi.org/10.1186/s13065-018-0384-7

Jürgen U. Keller, R. S. (2005). Gas Adsorption Equilibria. In *Gas Adsorption Equilibria*. https://doi.org/10.1007/b102056

Kavitha, M., Subramanian, R., Narayanan, R., & Udhayabanu, V. (2014). Solution combustion synthesis and characterization of strontium substituted hydroxyapatite nanocrystals. *Powder Technology*, *253*, 129–137. https://doi.org/10.1016/j.powtec.2013.10.045

Kede, M. L. F. M., Mavropoulos, E., da Rocha, N. C. C., Costa, A. M., da Silva, M. H. P., Moreira, J. C., & Rossi, A. M. (2012). Polymeric sponges coated with hydroxyapatite for metal immobilization. *Surface and Coatings Technology*, *206*(11–12), 2810–2816. https://doi.org/10.1016/j.surfcoat.2011.11.044

`

Khan, S. A., Khan, S. B., Khan, L. U., Farooq, A., Akhtar, K., & Asiri, A. M. (2018). Fourier transform infrared spectroscopy: Fundamentals and application in functional groups and nanomaterials characterization. *Handbook of Materials Characterization*, 317–344. https://doi.org/10.1007/978-3-319-92955-2_9

Khandelwal, H., & Prakash, S. (2016). Synthesis and Characterization of Hydroxyapatite Powder by Eggshell. *Journal of Minerals and Materials Characterization and Engineering*, *4*(March), 119–126.

Kim, Y. H. (2005). *Preparation of porous Si-incorporated hydroxyapatite*. *5*, 538–541. https://doi.org/10.1016/j.cap.2005.01.031

Kirimura, K., & Yoshioka, I. (2019). Citric acid. In *Comprehensive Biotechnology* (Third Edit, Vol. 3, Issue 25 C). Elsevier. https://doi.org/10.1016/B978-0-444-64046-8.00157-9

Kumar, S. K. S. Æ. T. S. S. (2007). A novel route for synthesis of nanocrystalline hydroxyapatite from eggshell waste. *J Mater Sci: Mater Med*, *18*, 1735–1743. https://doi.org/10.1007/s10856-007-3069-7

Kümmerer, K. (2008). Part II: Sources, Occurrence and Fate. In *Pharmaceuticals in the Environment: Sources, Fate, Effects and Risks*.

Kusmanto, F., Walker, G., Gan, Q., Walsh, P., Buchanan, F., Dickson, G., McCaigue, M., Maggs, C., & Dring, M. (2008). Development of composite tissue scaffolds containing naturally sourced mircoporous hydroxyapatite. *Chemical Engineering Journal*, *139*(2), 398–407. https://doi.org/10.1016/j.cej.2007.11.041

Kusrini, Eny & Sontang, M. (2012). Characterization of x-ray diffraction and electron spin resonance: Effects of sintering time and temperature on bovine hydroxyapatite. *Radiation Physics and Chemistry - RADIAT PHYS CHEM.*, *81*. https://doi.org/81. 10.1016/j.radphyschem.2011.10.006

Küster, A., & Adler, N. (2014). Pharmaceuticals in the environment: Scientific evidence of risks and its regulation. *Philosophical Transactions of the Royal Society B: Biological Sciences*, *369*(1656). https://doi.org/10.1098/rstb.2013.0587

Lanzirotti, A., Tappero, R., & Schulze, D. G. (2010). Practical application of synchrotron-based hard X-ray microprobes in soil sciences. In *Developments in Soil Science* (Vol. 34). Elsevier Masson SAS. https://doi.org/10.1016/s0166-2481(10)34002-5

Li, J., Liu, Y., Gao, Y., Zhong, L., Zou, Q., & Lai, X. (2016). Preparation and properties of calcium citrate nanosheets for bone graft substitute. *Bioengineered*, *7*(5), 376–381. https://doi.org/10.1080/21655979.2016.1226656

Li, Z., Li, M., Wang, Z., & Liu, X. (2020). Coadsorption of Cu(II) and tylosin/sulfamethoxazole on biochar stabilized by nano-hydroxyapatite in aqueous environment. *Chemical Engineering Journal*, *381*(June 2019), 122785. https://doi.org/10.1016/j.cej.2019.122785

Liao, J., Xiong, T., Ding, L., Xie, Y., Zhang, Y., & Zhu, W. (2022). Design of a renewable hydroxyapatite-biocarbon composite for the removal of uranium(VI) with high-efficiency adsorption performance. *Biochar*, *4*(1), 1–18. https://doi.org/10.1007/s42773-022-00154-1

`

Long, Y., Jiang, J., Hu, J., Hu, X., Yang, Q., & Zhou, S. (2019). Removal of Pb(II) from aqueous solution by hydroxyapatite/carbon composite: Preparation and adsorption behavior. *Colloids and Surfaces A: Physicochemical and Engineering Aspects*, *577*(Ii), 471–479. https://doi.org/10.1016/j.colsurfa.2019.06.011

López-Ortiz, S., Mendoza-Anaya, D., Sánchez-Campos, D., Fernandez-García, M. E., Salinas-Rodríguez, E., Reyes-Valderrama, M. I., & Rodríguez-Lugo, V. (2020). The pH Effect on the Growth of Hexagonal and Monoclinic Hydroxyapatite Synthesized by the Hydrothermal Method. *Journal of Nanomaterials*, *2020*. https://doi.org/10.1155/2020/5912592

Lopez, G. E. P., Madrid, J. F., & Abad, L. V. (2020). Chromium and cadmium adsorption on radiation-grafted polypropylene copolymers: regeneration, kinetics, and continuous fixed bed column studies. *SN Applied Sciences*, *2*(3), 1–10. https://doi.org/10.1007/s42452-020-2168-7

Luo, Y., Guo, W., Ngo, H. H., Nghiem, L. D., Hai, F. I., Zhang, J., Liang, S., & Wang, X. C. (2014). A review on the occurrence of micropollutants in the aquatic environment and their fate and removal during wastewater treatment. *Science of the Total Environment*, *473–474*, 619–641. https://doi.org/10.1016/j.scitotenv.2013.12.065

Mahmood, A. R., Al-haideri, H. H., & Hassan, F. M. (2019). *Detection of Antibiotics in Drinking Water Treatment Plants in Baghdad City , Iraq*. *2019*.

Meo, S. A. (n.d.). *Health hazards of cement dust*. *966*(29), 1153–1159.

Meski, S., Ziani, S., & Khireddine, H. (2010). *Removal of Lead Ions by Hydroxyapatite Prepared from the Egg Shell*. *2*(3), 3923–3928.

Mobasherpour, I., Heshajin, M. S., Kazemzadeh, A., & Zakeri, M. (2007). Synthesis of nanocrystalline hydroxyapatite by using precipitation method. *Journal of Alloys and Compounds*, *430*(1–2), 330–333. https://doi.org/10.1016/j.jallcom.2006.05.018

Mohammad, S. G., & El-sayed, M. M. H. (2020). Removal of imidacloprid pesticide using nanoporous activated carbons produced via pyrolysis of peach stone agricultural wastes. *Chemical Engineering Communications*, *0*(0), 1–12. https://doi.org/10.1080/00986445.2020.1743695

Mohammadi, M., Hassani, A. J., Mohamed, A. R., & Najafpour, G. D. (2010). *Removal of Rhodamine B from Aqueous Solution Using Palm Shell-Based Activated Carbon : Adsorption and Kinetic Studies*. 5777–5785.

Mohd Pu'ad, N. A. S., Abdul Haq, R. H., Mohd Noh, H., Abdullah, H. Z., Idris, M. I., & Lee, T. C. (2019). Synthesis method of hydroxyapatite: A review. *Materials Today: Proceedings*, *29*(November 2018), 233–239. https://doi.org/10.1016/j.matpr.2020.05.536

Mostafa, A. A., Oudadesse, H., & El-Sayed, M. M. H. (2015). A quantitative approach for studying the bioactivity of nanohydroxyapatite/gold composites. *Journal of Biomedical Materials Research - Part A*, *103*(11), 3483–3492. https://doi.org/10.1002/jbm.a.35494

Mousavi, S. A., Kamarehie, B., Almasi, A., Darvishmotevalli, M., Salari, M., Moradnia, M., Azimi, F., Ghaderpoori, M., Neyazi, Z., & Karami, M. A. (2021). Removal of Rhodamine B from aqueous solution by stalk corn activated carbon: adsorption and kinetic study. *Biomass*

`

Conversion and Biorefinery. https://doi.org/10.1007/s13399-021-01628-1

Mujahid, M., Sarfraz, S., & Amin, S. (2015). On the formation of hydroxyapatite nano crystals prepared using cationic surfactant. *Materials Research*, *18*(3), 468–472. https://doi.org/10.1590/1516-1439.298014

N. Elizondo-Villarreal, A., & Martínez-de-la-Cruz, R. Obregón Guerra, J.L. Gómez-Ortega, L. M. T.-M. & V. M. C. (2012). Biomaterials from Agricultural Waste : Eggshell-based Hydroxyapatite. *Water Air Soil Pollution*, *223*, 3643–3646. https://doi.org/10.1007/s11270-012-1137-1

Nagata, F., Yamauchi, Y., Tomita, M., & Kato, K. (2013). Hydrothermal synthesis of hydroxyapatite nanoparticles and their protein adsorption behavior. *Nippon Seramikkusu Kyokai Gakujutsu Ronbunshi/Journal of the Ceramic Society of Japan*, *121*(1417), 797–801. https://doi.org/10.2109/jcersj2.121.797

Nakazato, T., Tsukui, S., Nakagawa, N., & Kai, T. (2012). Continuous production of hydroxyapatite powder by drip pyrolysis in a fluidized bed. *Advanced Powder Technology*, *23*(5), 632–639. https://doi.org/10.1016/j.apt.2011.07.005

Narayanan, R., Singh, V., Kwon, T. Y., & Kim, K. H. (2009). Combustion synthesis of hydroxyapatite and hydroxyapatite (silver) powders. *Key Engineering Materials*, *396–398*, 411–419. https://doi.org/10.4028/www.scientific.net/kem.396-398.411

Narayanan, S. L., Arunkumar, C., Perumal, R., Saravanan, P. K., & Prasad, A. S. A. (2014). *A BATCH STUDY ON THE REMOVAL OF NICKEL (II) USING LOW COST ADSORBENT FLYASH*. *4*(1), 31–36.

Nasser A.M. Barakat, Myung Seob Khil, A.M. Omran, Faheem A. Sheikh, H. Y. K. (2009). Extraction of pure natural hydroxyapatite from the bovine bones bio waste by three different methods. *Journal of Materials Processing Technology*, *209*(7), 3408–3415. https://doi.org///doi.org/10.1016/j.jmatprotec.2008.07.040

Nayar, S., & Guha, A. (2009). Waste utilization for the controlled synthesis of nanosized hydroxyapatite. *Materials Science & Engineering C*, *29*(4), 1326–1329. https://doi.org/10.1016/j.msec.2008.10.002

Nyankson, E., & Kumar, R. V. (2019). Removal of water-soluble dyes and pharmaceutical wastes by combining the photocatalytic properties of Ag3PO4 with the adsorption properties of halloysite nanotubes. *Materials Today Advances*, *4*, 100025. https://doi.org/10.1016/j.mtadv.2019.100025

Oladipo, A. A., & Gazi, M. (2016). Uptake of Ni2+ and rhodamine B by nano-hydroxyapatite/alginate composite beads: batch and continuous-flow systems. *Toxicological and Environmental Chemistry*, *98*(2), 189–203. https://doi.org/10.1080/02772248.2015.1115506

Omar S. Bayomie, Haitham Kandeel, Tamer Shoeib , Hu Yang, N. Y., & El-Sayed, M. M. H. (2020). Novel approach for effective removal of methylene blue dye from water using fava bean peel waste. *Scientific RepoRtS*, *10*, 1–10. https://doi.org/10.1038/s41598-020-64727-5

Özkantar, N., Soylak, M., & Tüzen, M. (2017). Spectrophotometric detection of rhodamine B in

`

tap water, lipstick, rouge, and nail polish samples after supramolecular solvent microextraction. *Turkish Journal of Chemistry*, *41*(6), 987–994. https://doi.org/10.3906/kim-1702-72

Padmavathy, K. S., Madhu, G., & Haseena, P. V. (2016). A study on Effects of pH, Adsorbent Dosage, Time, Initial Concentration and Adsorption Isotherm Study for the Removal of Hexavalent Chromium (Cr (VI)) from Wastewater by Magnetite Nanoparticles. *Procedia Technology*, *24*, 585–594. https://doi.org/10.1016/j.protcy.2016.05.127

Pai, S., Kini, M. S., & Selvaraj, R. (2021). A review on adsorptive removal of dyes from wastewater by hydroxyapatite nanocomposites. *Environmental Science and Pollution Research*, *28*(10), 11835–11849. https://doi.org/10.1007/s11356-019-07319-9

Pai, S., M Kini, S., Selvaraj, R., & Pugazhendhi, A. (2020). A review on the synthesis of hydroxyapatite, its composites and adsorptive removal of pollutants from wastewater. *Journal of Water Process Engineering*, *38*(August), 101574. https://doi.org/10.1016/j.jwpe.2020.101574

Pandian BothiRaja, Kabilashen ReaddyiMunusamy, VeeradasanPerumal, M. N. M. (2022). Characterization of nanomaterial used in nanobioremediation. In *Nano-Bioremediation : Fundamentals and Applications* (pp. 57–83). https://doi.org/https://doi.org/10.1016/B978-0-12-823962-9.00037-4

Patel, M., Kumar, R., Kishor, K., Mlsna, T., Pittman, C. U., & Mohan, D. (2019). Pharmaceuticals of emerging concern in aquatic systems: Chemistry, occurrence, effects, and removal methods. *Chemical Reviews*, *119*(6), 3510–3673. https://doi.org/10.1021/acs.chemrev.8b00299

Pavia, D. L., Lampman, G. M., Kriz, G. S., & Vyvyan, J. R. (2000). Introduction to Spetroscopy. In *Tetrahedron Organic Chemistry Series* (Vol. 20, Issue C). https://doi.org/10.1016/S1460-1567(00)80010-0

Perrone, A., Finlayson, J. E., Bartelink, E. J., & Dalton, K. D. (2014). Chapter 7 - Application of Portable X-ray Fluorescence (XRF) for Sorting Commingled Human Remains. In *Commingled Human Remains: Methods in Recovery, Analysis, and Identification* (pp. 145–165). Elsevier. https://doi.org/10.1016/B978-0-12-405889-7.00007-1

Pham Minh, D., Tran, N. D., Nzihou, A., & Sharrock, P. (2013). Carbonate-containing apatite (CAP) synthesis under moderate conditions starting from calcium carbonate and orthophosphoric acid. *Materials Science and Engineering C*, *33*(5), 2971–2980. https://doi.org/10.1016/j.msec.2013.03.023

Phatai, P., Futalan, C. M., Kamonwannasit, S., & Khemthong, P. (2019). Structural characterization and antibacterial activity of hydroxyapatite synthesized via sol-gel method using glutinous rice as a template. *Journal of Sol-Gel Science and Technology*, *89*(3), 764–775. https://doi.org/10.1007/s10971-018-4910-9

Popoola, L. T. (2019). Characterization and adsorptive behaviour of snail shell-rice husk (SS-RH) calcined particles (CPs) towards cationic dye. *Heliyon*, *5*(1), e01153. https://doi.org/10.1016/j.heliyon.2019.e01153

`

Potts, P. J. (1995). X-Ray Absorption Fine Structure X-Ray Fluorescence and Emission. *Transform*, 408–418.

Pramanik, S., Agarwal, A. K., Rai, K. N., & Garg, A. (2007). Development of high strength hydroxyapatite by solid-state-sintering process. *Ceramics International*, *33*(3), 419–426. https://doi.org/10.1016/j.ceramint.2005.10.025

Putro, J. N., Handoyo, N., Kristiani, V., Soenjaya, S. A., Ki, O. L., Soetaredjo, F. E., Ju, Y. H., & Ismadji, S. (2014). Pomacea sp shell to hydroxyapatite using the ultrasound-microwave method (U-M). *Ceramics International*, *40*(7 PART B), 11453–11456. https://doi.org/10.1016/j.ceramint.2014.03.162

Qi, M. L., He, K., Huang, Z. N., Shahbazian-Yassar, R., Xiao, G. Y., Lu, Y. P., & Shokuhfar, T. (2017). Hydroxyapatite Fibers: A Review of Synthesis Methods. *Jom*, *69*(8), 1354–1360. https://doi.org/10.1007/s11837-017-2427-2

Qing, Q., Ying, X., & Wang, B. (2012). Microporous and Mesoporous Materials An activation-free protocol for preparing porous carbon from calcium citrate and the capacitive performance. *Microporous and Mesoporous Materials*, *158*, 155–161. https://doi.org/10.1016/j.micromeso.2012.03.031

Qing QingZhou, Xiang Ying Chen, B. W. (2012). An activation-free protocol for preparing porous carbon from calcium citrate and the capacitive performance. *Microporous and Mesoporous Materials*, *158*, 155–156. https://doi.org/https://doi.org/10.1016/j.micromeso.2012.03.031

Radnia, H., Ghoreyshi, A. A., Younesi, H., & Najafpour, G. D. (2012). Adsorption of Fe(II) ions from aqueous phase by chitosan adsorbent: Equilibrium, kinetic, and thermodynamic studies. *Desalination and Water Treatment*, *50*(1–3), 348–359. https://doi.org/10.1080/19443994.2012.720112

Raju, P. M. S. (2012). *Infiltration Growth Processing of YBCO nano-composites: Shape Forming, Microstructural and Magnetic Studies* (Issue 123).

Rao, R. R., Roopa, H. N., & Kannan, T. S. (1997). Solid state synthesis and thermal stability of HAP and HAP - β-TCP composite ceramic powders. *Journal of Materials Science: Materials in Medicine*, *8*(8), 511–518. https://doi.org/10.1023/A:1018586412270

Render, D., Samuel, T., King, H., Vig, M., Jeelani, S., Babu, R. J., & Rangari, V. (2016). Biomaterial-Derived Calcium Carbonate Nanoparticles for Enteric Drug Delivery. *Journal of Nanomaterials*, *2016*. https://doi.org/10.1155/2016/3170248

Rhee, S. H. (2002). Synthesis of hydroxyapatite via mechanochemical treatment. *Biomaterials*, *23*(4), 1147–1152. https://doi.org/10.1016/S0142-9612(01)00229-0

Robert J. Silbey, Robert A. Alberty, Moungi G. B. (2022). *Physical Chemistry* (5th ed.).

Rodriguez-Narvaez, O. M., Peralta-Hernandez, J. M., Goonetilleke, A., & Bandala, E. R. (2017). Treatment technologies for emerging contaminants in water: A review. *Chemical Engineering Journal*, *323*, 361–380. https://doi.org/10.1016/j.cej.2017.04.106

Rout, S., Muduli, B., Kumar, A., & Pulhani, V. (2020). Removal of uranium(VI) from water using hydroxyapatite coated activated carbon powder nanocomposite. *Journal of Environmental*

`

Science and Health - Part A Toxic/Hazardous Substances and Environmental Engineering, *55*(5), 596–605. https://doi.org/10.1080/10934529.2020.1721228

Rutgersson, C., Fick, J., Marathe, N., Kristiansson, E., Janzon, A., Angelin, M., Johansson, A., Shouche, Y., Flach, C. F., & Larsson, D. G. J. (2014). Fluoroquinolones and qnr genes in sediment, water, soil, and human fecal flora in an environment polluted by manufacturing discharges. *Environmental Science and Technology*, *48*(14), 7825–7832. https://doi.org/10.1021/es501452a

S. J. Lee, S. H. O. (2003). Fabrication of calcium phosphate bioceramics by using eggshell and phosphoric acid. *Materials Letters*, *57*, 4570–4574. https://doi.org/10.1016/S0167-577X(03)00363-X

S. LOWELL, JOAN E. SHIELDS, MARTIN A. THOMAS, M. T. (2004). Characterization of Porous Solids and Powders: Surface Area, Pore Size and Density. In *y Kluwer Academic Publishers*.

Sanosh, K. P., Chu, M., Balakrishnan, A., Kim, T. N., & Cho, S. (2009a). Utilization of biowaste eggshells to synthesize nanocrystalline hydroxyapatite powders. *Materials Letters*, *63*(24–25), 2100–2102. https://doi.org/10.1016/j.matlet.2009.06.062

Sanosh, K. P., Chu, M. C., Balakrishnan, A., Kim, T. N., & Cho, S. J. (2009b). Preparation and characterization of nano-hydroxyapatite powder using sol-gel technique. *Bulletin of Materials Science*, *32*(5), 465–470. https://doi.org/10.1007/s12034-009-0069-x

Santos, M. H., Oliveira, M. de, Souza, L. P. de F., Mansur, H. S., & Vasconcelos, W. L. (2004). Synthesis control and characterization of hydroxyapatite prepared by wet precipitation process. *Materials Research*, *7*(4), 625–630. https://doi.org/10.1590/s1516-14392004000400017

Santwana Padhi, A. B. (2022). Chapter 17 - Biosynthesis of Silver Nanoparticles: Synthesis, mechanism, and characterization. In *Agri-Waste and Microbes for Production of Sustainable Nanomaterials* (pp. 397–440). https://doi.org/https://doi.org/10.1016/B978-0-12-823575-1.00008-1

Sasikumar, S., & Vijayaraghavan, R. (2008). Solution combustion synthesis of bioceramic calcium phosphates by single and mixed fuels-A comparative study. *Ceramics International*, *34*(6), 1373–1379. https://doi.org/10.1016/j.ceramint.2007.03.009

Sassoni, E. (2018). Hydroxyapatite And Other calcium phosphates for the conservation of cultural heritage: A review. *Materials*, *11*(4). https://doi.org/10.3390/ma11040557

Seo, M., Lee, S., Lee, C., & Cho, S. (2019). *Recycling of Cement Kiln Dust as a Raw Material for Cement*.

Shaltout, A. A., Allam, M. A., & Moharram, M. A. (2011). FTIR spectroscopic, thermal and XRD characterization of hydroxyapatite from new natural sources. *Spectrochimica Acta - Part A: Molecular and Biomolecular Spectroscopy*, *83*(1), 56–60. https://doi.org/10.1016/j.saa.2011.07.036

Shavandi, A., Bekhit, A. E. D. A., Ali, A., & Sun, Z. (2015). Synthesis of nano-hydroxyapatite (nHA) from waste mussel shells using a rapid microwave method. *Materials Chemistry and*

Physics, *149*, 607–616. https://doi.org/10.1016/j.matchemphys.2014.11.016

Shavandi, A., Bekhit, A. E. D. A., Sun, Z., & Ali, A. (2015). A review of synthesis methods, properties and use of hydroxyapatite as a substitute of bone. *Journal of Biomimetics, Biomaterials and Biomedical Engineering*, *25*, 98–117. https://doi.org/10.4028/www.scientific.net/JBBBE.25.98

Shen, K., & Gondal, M. A. (2017). Removal of hazardous Rhodamine dye from water by adsorption onto exhausted coffee ground. *Journal of Saudi Chemical Society*, *21*(November), S120–S127. https://doi.org/10.1016/j.jscs.2013.11.005

Shields, S. L. and J. E. (1991). Powder Surface Area and Porosity. In B. SCARLETI (Ed.), *News.Ge* (3rd editio). Springer-Science+Business Media, B.V. https://link.springer.com/content/pdf/10.1007/978-94-015-7955-1.pdf

Shu, C., Yanwei, W., Hong, L., Zhengzheng, P., & Kangde, Y. (2005). Synthesis of carbonated hydroxyapatite nanofibers by mechanochemical methods. *Ceramics International*, *31*(1), 135–138. https://doi.org/10.1016/j.ceramint.2004.04.012

Siddique, R. (2014). Utilization of industrial by-products in concrete. *Procedia Engineering*, *95*(December 2014), 335–347. https://doi.org/10.1016/j.proeng.2014.12.192

Simpson, J. H. (2012). Data Collection, Processing, and Plotting. In *Organic Structure Determination Using 2-D NMR Spectroscopy*. https://doi.org/10.1016/b978-0-12-384970-0.00003-x

Sobczak A, Kowalski Z, W. Z. (2009). Preparation of hydroxyapatite from animal bones. *Acta Bioeng Biomech*, *11*(4), 8–23.

Songnan Li, Jun Wang, Xiaoyan Jing, Qi Liu, Jamil Saba, Tom Mann, M. Z., & Hao Wei, Rongrong Chen, and L. L. (2012). Conversion of Calcined Eggshells into Flower-Like Hydroxyapatite Agglomerates by Solvothermal Method Using Hydrogen Peroxide/ N,N-Dimethylformamide Mixed Solvents. *The American Ceramic Society*, *3379*, 3377–3379. https://doi.org/10.1111/j.1551-2916.2012.05458.x

Soylak, M., Unsal, Y. E., Yilmaz, E., & Tuzen, M. (2011). Determination of rhodamine B in soft drink, waste water and lipstick samples after solid phase extraction. *Food and Chemical Toxicology*, *49*(8), 1796–1799. https://doi.org/10.1016/j.fct.2011.04.030

Stuart, B. H. (2004). *Infrared Spectroscopy: Fundamentals and Applications* (1st editio). John Wiley & Sons, Incorporated: Hoboken. https://doi.org/DOI:10.1002/0470011149

Su, M., Liu, Z., Wu, Y., Peng, H., Ou, T., Huang, S., Song, G., Kong, L., Chen, N., & Chen, D. (2021). Graphene oxide functionalized with nano hydroxyapatite for the efficient removal of U(VI) from aqueous solution. *Environmental Pollution*, *268*(Vi), 115786. https://doi.org/10.1016/j.envpol.2020.115786

Sundarabharathi, L., Ponnamma, D., Parangusan, H., Chinnaswamy, M., & Al-Maadeed, M. A. A. (2020). Effect of anions on the structural, morphological and dielectric properties of hydrothermally synthesized hydroxyapatite nanoparticles. *SN Applied Sciences*, *2*(1), 1–13. https://doi.org/10.1007/s42452-019-1807-3

`

Szcześ, A., Hołysz, L., & Chibowski, E. (2017). Synthesis of hydroxyapatite for biomedical applications. *Advances in Colloid and Interface Science*, *249*, 321–330. https://doi.org/10.1016/j.cis.2017.04.007

Taylor, P., Neelakandeswari, N., Sangami, G., Dharmaraj, N., Neelakandeswari, N., Sangami, G., & Dharmaraj, N. (2011). Preparation and Characterization of Nanostructured Hydroxyapatite Using a Biomaterial. *Synthesis and Reactivity in Inorganic , Metal-Organic , and Nano-Metal Chemistry*, *December 2014*, 37–41. https://doi.org/10.1080/15533174.2011.568434

Tong, C. (2019). *Introduction to Materials for Advanced Energy Systems*.

Tzabar, N., & ter Brake, H. J. M. (2016). Adsorption isotherms and Sips models of nitrogen, methane, ethane, and propane on commercial activated carbons and polyvinylidene chloride. *Adsorption*, *22*(7), 901–914. https://doi.org/10.1007/s10450-016-9794-9

Udayakantha, K. S. M., De Silva, R. M., De Silva, K. M. N., & Hettiarachchi, C. (2015). Biocompatible nano hydroxyapatite - Curcumin bi-coated antibacterial activated carbon for water purification. *RSC Advances*, *5*(79), 64696–64703. https://doi.org/10.1039/c5ra11518c

Utara, S., & Klinkaewnarong, J. (2015). Sonochemical synthesis of nano-hydroxyapatite using natural rubber latex as a templating agent. *Ceramics International*, *41*(10), 14860–14867. https://doi.org/10.1016/j.ceramint.2015.08.018

Walsh, P. J., Buchanan, F. J., Dring, M., Maggs, C., Bell, S., & Walker, G. M. (2008). Low-pressure synthesis and characterisation of hydroxyapatite derived from mineralise red algae. *Chemical Engineering Journal*, *137*(1), 173–179. https://doi.org/10.1016/j.cej.2007.10.016

Wang, Y., Hu, L., Zhang, G., Yan, T., Yan, L., Wei, Q., & Du, B. (2017). Removal of Pb(II) and methylene blue from aqueous solution by magnetic hydroxyapatite-immobilized oxidized multi-walled carbon nanotubes. *Journal of Colloid and Interface Science*, *494*(Ii), 380–388. https://doi.org/10.1016/j.jcis.2017.01.105

Wang, Y., Zhang, S., Wei, K., Zhao, N., Chen, J., & Wang, X. (2006). Hydrothermal synthesis of hydroxyapatite nanopowders using cationic surfactant as a template. *Materials Letters*, *60*(12), 1484–1487. https://doi.org/10.1016/j.matlet.2005.11.053

Wei, W., Yang, L., Zhong, W. H., Li, S. Y., Cui, J., & Wei, Z. G. (2015). Fast removal of methylene blue from aqueous solution by adsorption onto poorly crystalline hydroxyapatite nanoparticles. *Digest Journal of Nanomaterials and Biostructures*, *10*(4), 1343–1363.

Werkneh, A. A., Haftu, N. G., & Beyene, H. D. (2014). *Removal of hexavalent chromium from tannery wastewater using activated carbon primed from sugarcane bagasse : Adsorption / desorption studies*. *2*(6), 128–135. https://doi.org/10.11648/j.ajac.20140206.16

Widiyastuti, W., Setiawan, A., Winardi, S., Nurtono, T., & Setyawan, H. (2014). Particle formation of hydroxyapatite precursor containing two components in a spray pyrolysis process. *Frontiers of Chemical Science and Engineering*, *8*(1), 104–113. https://doi.org/10.1007/s11705-014-1406-1

Wilcox, W., & Thron, C. (2016). Scattering and Diffraction. *Macroscopic Electrodynamics*, *0*, 641–686. https://doi.org/10.1142/9789814616638_0012

`

Wu, S., Hsu, H., Wu, Y., & Ho, W. (2011). Hydroxyapatite synthesized from oyster shell powders by ball milling and heat treatment. *Materials Characterization*, *62*(12), 1180–1187. https://doi.org/10.1016/j.matchar.2011.09.009

Wu, S., Tsou, H., Hsu, H., & Hsu, S. (2013). A hydrothermal synthesis of eggshell and fruit waste extract to produce nanosized hydroxyapatite. *Ceramics International*, *39*(7), 8183–8188. https://doi.org/10.1016/j.ceramint.2013.03.094

Xiao, W., Gao, H., Qu, M., Liu, X., Zhang, J., Li, H., Yang, X., Li, B., & Liao, X. (2018). Rapid microwave synthesis of hydroxyapatite phosphate microspheres with hierarchical porous structure. *Ceramics International*, *44*(6), 6144–6151. https://doi.org/10.1016/j.ceramint.2017.12.247

Xu, L., Zhang, J., Ding, J., Liu, T., Shi, G., Li, X., Dang, W., Cheng, Y., & Guo, R. (2020). Pore structure and fractal characteristics of different shale lithofacies in the dalong formation in the western area of the lower yangtze platform. *Minerals*, *10*(1). https://doi.org/10.3390/min10010072

Xu, Y., An, L., Chen, L., Xu, H., Zeng, D., & Wang, G. (2018). Controlled hydrothermal synthesis of strontium-substituted hydroxyapatite nanorods and their application as a drug carrier for proteins. *Advanced Powder Technology*, *29*(4), 1042–1048. https://doi.org/10.1016/j.apt.2018.01.008

Yelten-Yilmaz, A., & Yilmaz, S. (2018). Wet chemical precipitation synthesis of hydroxyapatite (HA) powders. *Ceramics International*, *44*(8), 9703–9710. https://doi.org/10.1016/j.ceramint.2018.02.201

Yeong, K. C. B., Wang, J., & Ng, S. C. (2001). Mechanochemical synthesis of nanocrystalline hydroxyapatite from CaO and CaHPO4. *Biomaterials*, *22*(20), 2705–2712. https://doi.org/10.1016/S0142-9612(00)00257-X

Ying Zhang, Yong Liu, Xiaobo Ji, C. E. B. and W. Z. (2011). Conversion of egg-shell to hydroxyapatite for highly sensitive detection of endocrine disruptor bisphenol A †. *Journal of Materials Chemistry*, *21*, 14428–14431. https://doi.org/10.1039/c1jm12544c

Yoganand, C. P., Selvarajan, V., Goudouri, O. M., Paraskevopoulos, K. M., Wu, J., & Xue, D. (2011). Preparation of bovine hydroxyapatite by transferred arc plasma. *Current Applied Physics*, *11*(3), 702–709. https://doi.org/10.1016/j.cap.2010.11.035

Yuan, L., Yan, M., Huang, Z., He, K., Zeng, G., Chen, A., Hu, L., Li, H., Peng, M., Huang, T., & Chen, G. (2019). Influences of pH and metal ions on the interactions of oxytetracycline onto nano-hydroxyapatite and their co-adsorption behavior in aqueous solution. *Journal of Colloid And Interface Science*, *541*, 101–113. https://doi.org/10.1016/j.jcis.2019.01.078

Zhang, G., Chen, J., Yang, S., Yu, Q., Wang, Z., & Zhang, Q. (2011). Preparation of amino-acid-regulated hydroxyapatite particles by hydrothermal method. *Materials Letters*, *65*(3), 572–574. https://doi.org/10.1016/j.matlet.2010.10.078

Zhao, H., Park, Y., Lee, D. H., & Park, A. H. A. (2013). Tuning the dissolution kinetics of wollastonite via chelating agents for CO2 sequestration with integrated synthesis of precipitated calcium carbonates. *Physical Chemistry Chemical Physics*, *15*(36), 15185–

15192. https://doi.org/10.1039/c3cp52459k

Zhao, X., Yuan, P., Yang, Z., Peng, W., Meng, X., & Cheng, J. (2022). *Integration of Micro-Nano-Engineered Hydroxyapatite / Biochars with Optimized Sorption for Heavy Metals and Pharmaceuticals*. 1–17.

`

Appendix

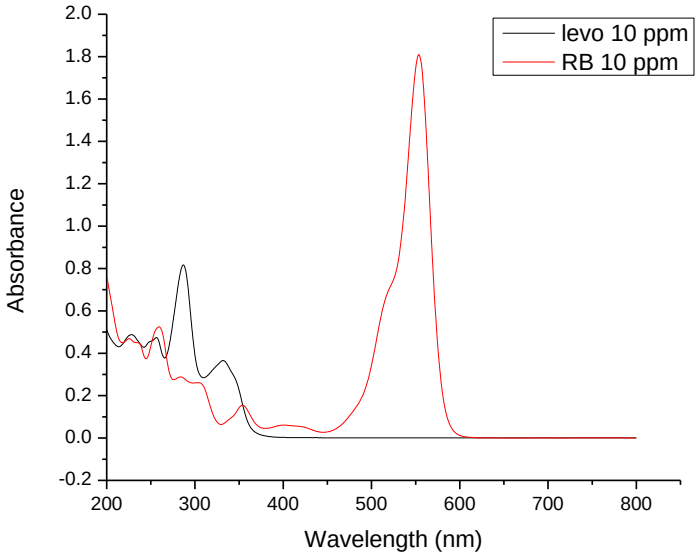
levo 10 ppm
RB 10 ppm
Absorbance
Wavelength (nm)
2.0
1.8
1.6
1.4
1.2
1.0
0.8
0.6
0.4
0.2
0.0
-0.2
200
300
400
500
600
700
800

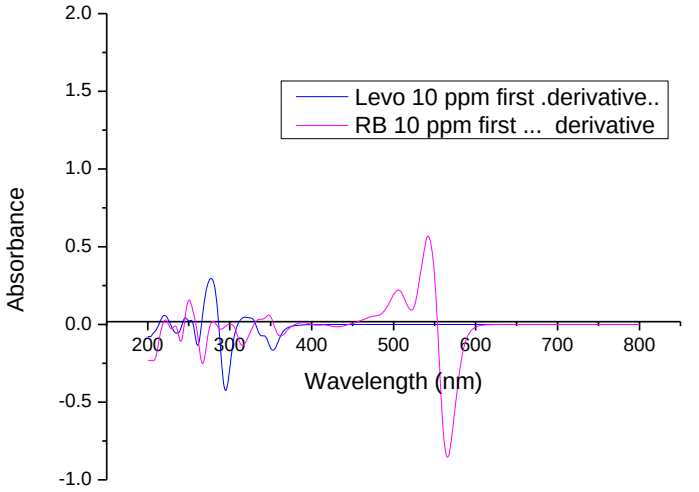
Levo 10 ppm first .derivative..
RB 10 ppm first ... derivative
Absorbance
Wavelength (nm)
2.0
1.5
1.0
0.5
0.0
-0.5
-1.0
200
300
400
500
600
700
800

`

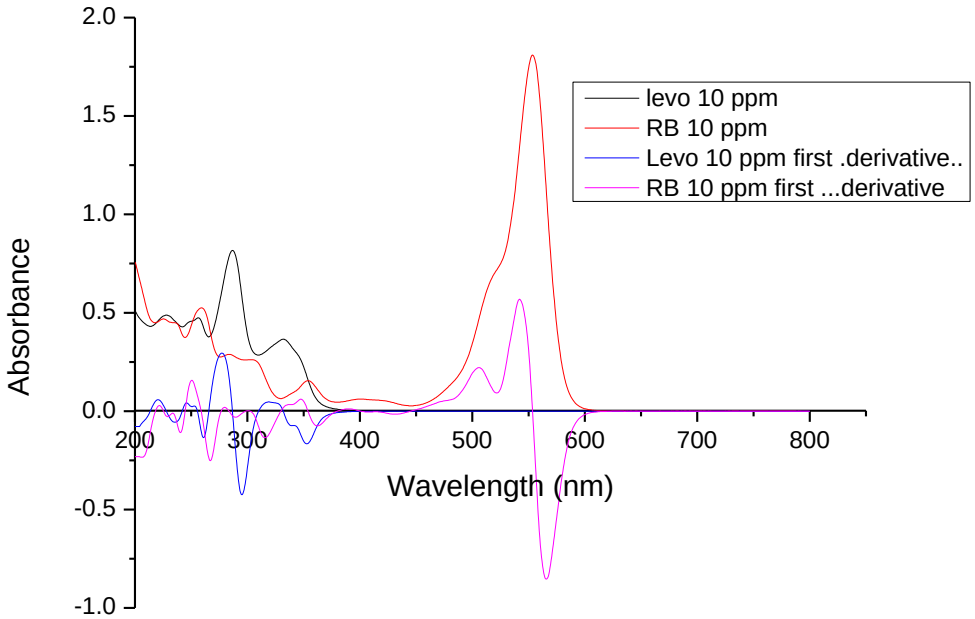

Standard JCPDS XRD of Calcium Carbonate (Render et al., 2016)